CHARACTERISTICS OF AIR FLOW OVER A SESSILE DROPLET AT THE VERGE OF SHEDDING

REZA YAGHOUBI EMAMI

A THESIS SUBMITTED TO
THE FACULTY OF GRADUATE STUDIES
IN PARTIAL FULFILLMENT OF THE REQUIREMENTS
FOR THE DEGREE OF
MASTER OF SCIENCE

GRADUATE PROGRAM IN MECHANICAL ENGINEERING

YORK UNIVERSITY

TORONTO, ONTARIO

APRIL 2020

Abstract

A Particle Image Velocimetry (PIV) study on the air flow over a sessile water droplet exposed to a boundary layer flow was done in a wind tunnel. The free stream velocity, U_∞ was set just below the air velocity that causes the droplet to move. Reynolds number based on U_∞ and the height of the droplet (h) was $600 < Re_h \leq 1000$. We studied the effects of the substrate wettability (PMMA, PEMA, PS, and Teflon) and droplet size ($10 - 30\,\mu l$) on flow characteristics (flow structure, turbulence, etc.) in the plane that bisects the droplet streamwise. For that purpose, a PIV experimental setup -including the closed wind tunnel- was designed, fabricated and set up. To study the effect of drop oscillations in the flow, solid mockups of the droplets were 3D-printed. The flow structure showed a bifurcation that was not seen when 2D objects were examined (this is due to intrusion of flow from sides into the wake area). Considering only the midplane of the droplets:

The flow structure (pattern) was seen to be the same for all cases regardless of the surface wettability and drop size (the differences seen for shedding of droplets of different sizes and on different surfaces, are not due to the structure of the flow). For hydrophilic surfaces, the normalized recirculation length decreases with size, while, for hydrophobic surfaces, the normalized recirculation length increases with size. The order of separation angle is the same for all cases and for all cases fall in $92° - 98°$. The order of c_f is the same for all the cases due to velocity profile and separation angle similarity. The order of magnitude of c_p is the same for all drop sizes on different surface wettabilities. The drag force by which the droplets are depinned changes only with AU_∞^2 (A is the frontal area of the droplet). For all droplet sizes and surface wettabilities, the instantaneous drag coefficient is similar to their average value as turbulence around the droplet

profile is insignificant. For a tandem arrangement of droplets, the droplet placed downstream would be exposed to a shearing flow:

- With higher turbulence intensity, if for small droplets, the droplets are placed on PS and PMMA
- Of the same turbulence intensity for all surface wettabilities, if the droplets are large
- With higher turbulence intensity, if the droplets are larger

The effect of oscillation in flow structure and turbulence statistics is equivalent to the effect of surface roughness for the 3D-printed solid mockups (if the ramp-up of the air velocity is as slow as ~2.8 (m⁄s)/min).

Dedication

Dedicated to My Mom and Dad!

I question many things. I look at the swaying shade of a willow tree and wonder if it is real. I wonder if the solid ground beneath my feet is actually physically present. I wonder if all the scientific models I studied all these years came any close to the sheer truth!

I wonder if the abundance around me – or myself- are any different from nothingness!

Your love, I have never questioned. The love you have given me, is the most present and the most precious reality in my life!

Thank you and love you forever and ever and more!

Acknowledgements

I’d like to thank my supervisor who’s been always supportive to me during this project. His supervision was not limited to scientific and technical matters on the project. He generously offered advice and thoughts on professionalism and philosophy of life –those which he himself learned by experience- which is quite valuable to me and I very much thank him for his words of wisdom and his kind support.

I’d like to thank all the faculty members and staff in Mechanical Engineering Department who have helped me throughout the program. Especially, Professor Hanson, Professor Melenka, and Professor Tabatabaei from which I have sought help for my project and was kindly and supportively guided.

I am blessed with a sweet and supportive family (Uncles, aunts, cousins…). Each have helped and supported me in my life! I can never thank them enough! Especially, I’d like to thank my kind, kind, and one of a kind brothers from whom I’ve never seen anything but support and love. Although I haven’t been of any help to them; who and where I am, is a result of their efforts, support and love throughout my life. Love them!

I’d like to thank me! I’d like to thank me for I have chosen beautiful good-hearted people around me as my friends! And I’d like to thank those people for they have chosen to be my friend! Friends, who despite my introversion, -or maybe they mind but- have always been there for me, helped me and brought cheer every now and then. I have learned from them and felt happy to have them in my life! They are treasures whom I’d be a fool to take for granted! Love them!

Table of Contents

List of Tables

List of Figures

List of Symbols, Nomenclature, Abbreviations

A – area of the droplet in the plane that bisects the droplet streamwise

AOF – area of interest

Bo – Bond number

c_d – drag coefficient

c_f – coefficient of friction (form drag)

c_p – pressure coefficient

CZ – contraction zone

CAH– contact angle hysteresis

CCD – charged coupled devices

CDS – correlated double sampling

CFD – computational fluid dynamics

CID – charged injection devices

CQS – correlated quadruple sampling

CMOS – complementary metal oxide semi-conductor

d – drop initial contact diameter

d_p – particle diameter

DOF – depth of field

f – focal length

$F_{adhesion}$ – adhesion orce

FFT – Fast Fourier Transform

g – gravitational acceleration

GDL – Gas Diffusion Layer

h – drop height

h_d – drop height

K – pressure drop coefficient

L – contact length (contact line diameter)

L_e – entrance length

M – Mach number

N – contraction ratio

P – pressure

PS - Polystyrene

PIV- particle image velocimetry

PEMA – poly(ethyl methacrylate)

PMMA – poly(methyl methacrylate)

PEMFC – Proton Exchange Membrane Fuel Cell

Q – peak ratio

TS – test section

U_{crit} – critical air velocity for incipient motion (i.e. for the onset of drop motion)

u – streamwise velocity

$\bar{u}$ – time-averaged streamwise velocity

U_g – gravitationally induced velocity

U_∞ – free stream air velocity

u'_{rms} – root mean square of velocity fluctuations

$\overline{u'v'}$ – Reynolds stress

V – volume of the droplet

v – Wall-normal velocity

$\bar{v}$ – time-averaged y-velocity

VOF – Volume of Fluid (a CFD Technique)

w – Spanwise velocity

β – open area ratio (for screens)

γ – surface tension

δ – local boundary layer thickness

θ_d – diffuser angle

θ – contact angle

θ_a – advancing contact angle

θ_r – receding contact angle

λ – laser wavelength

μ – viscosity of air

ρ – air density

ρ_d – particle density

ψ – azimuthal angle

1D – one dimension(al) (spatial dimension)

2D – two dimension(al) (spatial dimensions)

3D – three dimension(al) (spatial dimensions)

1 Introduction

1.1 Conceptual Example

This thesis concerns the air flow characteristics over a sessile droplet (a droplet sitting on a surface) at the verge of shedding. In that, the air flow structure and the turbulence intensity are investigated to understand various characteristics associated with the flow, specifically, the drag force imposed by the shearing air flow on the droplet. As a conceptual example, consider the raindrops sitting on the blades of a wind turbine. In a cold weather, these drops turn to ice and stick to the surface of the blades. Literature shows that these frozen droplets could dramatically change the efficiency of wind turbines [1]. The same issue is for aircrafts as well [2]. Now, before these droplets are turned to ice, it would be advantageous, if they are removed from the surface using an external force. In the absence of external stimuli e.g. gravitational force, and drag force, a droplet sits on a surface, with its shape being defined by surface wettability. The symmetric shape of a sessile droplet can be approximated with a spherical cap based on its contact angle and size. A shearing air flow makes the droplet to deform from its symmetric shape and it may cause the droplet to oscillate. The deformity of the droplet changes the uniform distribution of interfacial forces acting on the contact line. The change of contact angle is such that:

- on the upstream half of the droplet, the contact angle becomes less than its stable value (receding contact angle)
- on the downstream half of the droplet, the contact angle becomes more than its stable value (advancing contact angle)

Figure 1-1 shows a sessile droplet at rest and at the verge of shedding (deformed).

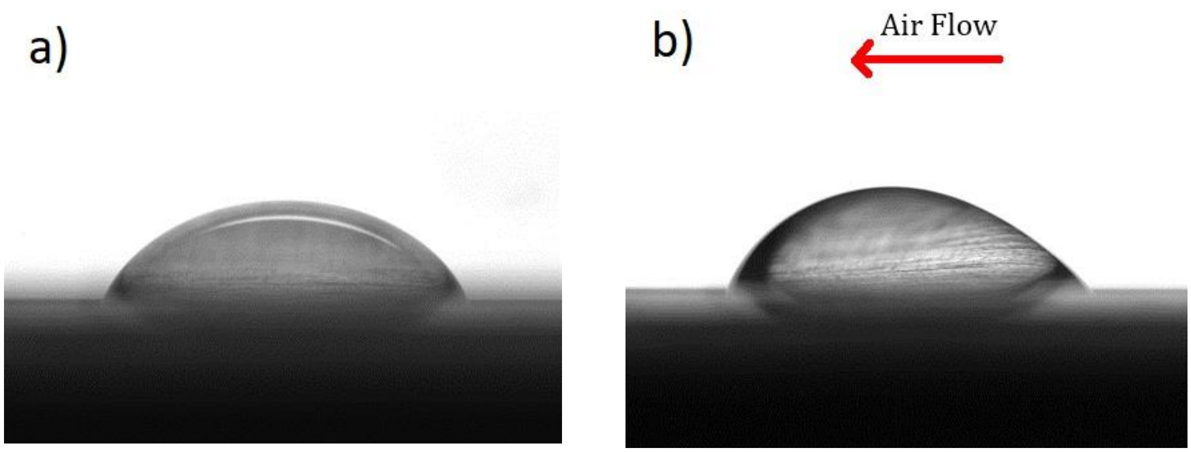

Figure 1-1. a) a sessile droplet at rest. b) a sessile droplet at the verge of shedding

The shearing air flow imposes a drag force on the droplet, due to the shear stress acting on the surface of the droplet and the streamwise pressure difference across the droplet. The non-uniform distribution of contact angle, on the other hand, imposes a resistance force on the contact line known as adhesion force. As the velocity of the air flow increases, the drag force increases, causing the droplet to deform such that the induced adhesion force equals the drag force. Further increasing the air velocity, there comes a point in which the droplet cannot deform further its contact angle hysteresis to resist the drag force. Consequently, the droplet starts to depin (incipient motion). This is followed by the droplet being removed (shed) from the surface (runback).

Aside from the icing issue, water management in fuel cells (as to avoid the clogging/flooding due to droplets pinned in fuel cell plates) is another concern in science and industry [3]. Droplet shedding has also various applications in heat exchangers [4], improving visibility in rainy conditions (for flights and cars) and cleaning [5]. Enhanced oil recovery is also another notable application in which the shearing fluid is not necessarily air and a flowing liquid is present instead.

In this study, water is used to form sessile droplets. The volumes of $10\ \mu l$, $20\ \mu l$, and $30\ \mu l$ was considered. The flow of interest in this study was the flow over a flat plate. Because, this is the closest condition to the shedding of water droplets for most of the applications e.g. aircrafts, and wind turbines. The local Reynolds number of the air flow varies between 3×10^4 and 7.2×10^4 based on the location of the sessile droplet and free stream velocity of the air.

In the following section, the literature for the shedding of sessile droplets is given. The review mainly concerns the studies for air flow over sessile droplets at the verge of shedding

1.2 Literature Review

1.2.1 Shedding: Principles and fundamentals

Droplet shedding is a process in which a droplet gets detached from a surface. The conditions which contribute to the incipient motion of sessile droplets are of high interest to researchers. This is due to the various applications in which the understanding of the droplet shedding could affect the associated industries significantly. These applications are aircraft-icing [2,6], wind turbine icing [1], heat exchangers [4], water management in fuel cells [5,7], enhanced oil recovery [8] and cleaning [6].

This process is always associated with an external force which is mostly either the gravitational force or the drag force imposed by an air flow. Now, if there is no air flow and the droplet is sitting on a horizontal surface, the droplet is at rest (sessile). The geometry of a sessile droplet is controlled by the wetting characteristics of the substrate namely, surface tension/energy, contact angle (which is dependent on both the liquid and the substrate), and contact line shape/size. It is also the gravity which affects the geometry of the droplet. However, for small droplets showing a Bond number (describing the ratio of capillary forces to gravitational forces) less than unity ($Bo < 1$) the gravitational effect is negligible which is also the case for this study. For an ideal surface (chemically homogeneous and uniformly rough) the shape of the contact line is circular, and the contact angle is uniformly distributed along the contact line. When a sessile droplet is exposed to the air flow, it starts to deform, changing the distribution of the contact angle along the contact line [9]. This non-uniform distribution of contact angle imposes a resistance force on the contact line known as adhesion force. Figure 1-2 shows the effect of the contact angle distribution along the contact line on the interfacial forces between the droplet and the surface. The adhesion force is the integral of surface tension components being projected in the external force direction:

$$F_{adhesion} = F_x = \int_0^L \gamma_x dl = -\gamma \int_0^L cos\theta(l) cos\psi(l) dl \tag{1-1}$$

As the drag force is increased, the droplet is deformed in such a way that the adhesion force counterbalances the drag force. This simply impedes the droplet from movement. However, there comes a point in which the adhesion force cannot be further increased. In that moment which is known as the “incipient motion” of the droplet, the contact line is no further pinned to its previous location and the droplet starts to move. [10]

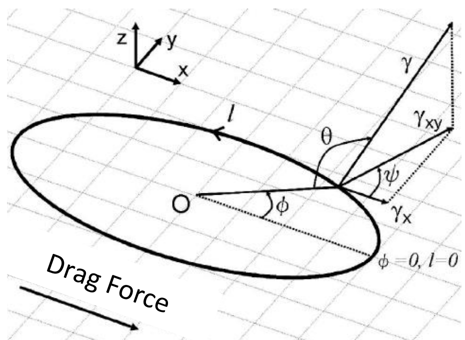

Figure 1-2: View of the contact line of a droplet exposed to the air flow [11] (with permission from the author)

Droplet shedding with air flow is a complex problem. The complexities are mainly due to: interfacial interactions, deformability of the droplet, and external flow characteristics. On the interfacial interactions, the complexities lead to a not-quite-accurate calculated adhesion force. Because, to calculate the adhesion force, the distribution of the contact angle over the contact line in each deformed state of the droplet should be known, in addition to the geometry (shape/size) of the contact line. However, that is not a trivial effort. Researchers have put forward various models for the shape of the contact line and the distribution of contact angle over it [12-16]. These simplifications which are proposed for droplets on inclined surfaces lead to the calculation of the adhesion force. Consequently, the accuracy of the calculated adhesion force is contingent on the validity of these models. For instance, Antonini et al. [11] reported that these simplifications could lead to errors up to 76% in the estimated adhesion force, with their high precision measurement technique called IBAFA. Milne et al. [17] found a diffuse literature for the oscillation of constrained droplets. They proposed a unifying conceptual framework on the oscillation of droplets, based on the review of literature. In this framework, bulk and surface modes of oscillation and their coupling is clarified for constrained droplets.

Finally, droplet shedding is a considerably complex aerodynamics problem. This is due to the presence of small-scale turbulence, possible distinct state of vortex shedding, the presence of boundary layer (locally variable non-uniform velocity profile upstream the droplet), and near-wall effects. Due to the three-dimensional separation points on the droplet surface (opposed to cylindrical shapes), various small wakes will form behind the droplet. Furthermore, the non-uniformity of the incoming velocity profile (boundary layer effect) brings about distinct wakes compared to uniform flows.

The occurrence of such phenomena for flow over a droplet can be predicted based on literature for air flow over rigid bodies. For instance, Jang and Lee [18] study the water flow past a sphere at a Re number of 11000 (based on the free stream velocity and sphere diameter) using PIV. They state that for spheres, in a Re range of 420-800 an asymmetric flow is observed, and unsteadiness continues. Their results show small vortices that are distributed circumferentially in a circular shape behind the sphere (which is due to the 3D flow separation points). On the effect of boundary layer on forming small scale turbulence, Ozgoren et al.'s [19] study on the wake patterns past a sphere in a boundary layer of a water channel is of note. The Re number for their study is $2500 \leq$

$Re \leq 10000$ (based on free stream velocity and sphere diameter). They reported various small eddies being formed around and in the larger vortices downstream due to Kelvin-Helmholtz instability in the boundary layer region. In another study, Ozgoren et al. [20] observed small scale vortices downstream a sphere and a cylinder located in free stream flow of a water tunnel. For this study, Reynolds numbers were set to 5000 and 10000 (based on free stream velocity and sphere diameter). They indicated that the concentration of small-scale vortices are more dominant in the wake of a sphere than that of a cylinder. Consequently, it can be expected that such small-scale turbulence exists in the process of shedding for a sessile droplet. The extent of which, and its effect on the shedding process, however, is to be clarified through a fundamental study on the aerodynamics of the process.

Regarding the state of vortex shedding, primarily, the frequency of the oscillation of the droplet is expected to change the vortex shedding pattern of the problem compared to that of the rigid bodies. The effect of deformability on the state of vortex shedding for deformable objects (not including droplets) has been vastly studied in literature [21-24]. Also, because a sessile droplet is attached to the surface, the vortex shedding pattern is expected to be different than that of the suspended bluff bodies [19]. The effect of boundary layer presence is obviously the non-uniform velocity profile that makes the problem complicated. Plus, this non-uniform velocity profile changes with the location of the droplet with respect to where the boundary layer starts to develop (See Figure 1-3). This contributes to a change of drag force as the location inside the boundary layer is changed [25]. Thus, it is quite necessary to consider where the droplet sits considering the boundary layer, as the mere report on the state of the outer boundary layer flow would be insufficient in that case. Finally, the near-wall effects are another determinant on the complex state of flow pattern behind a droplet.

Even though the complexities associated with the adhesion force and oscillations of a droplet has been addressed in literature for sessile droplets, the complexities regarding the aerodynamics aspect of the problem have been surprisingly overlooked thus far. In that regards studies divide into experimental and numerical investigations both failing to address the aerodynamics of the droplet shedding comprehensively.

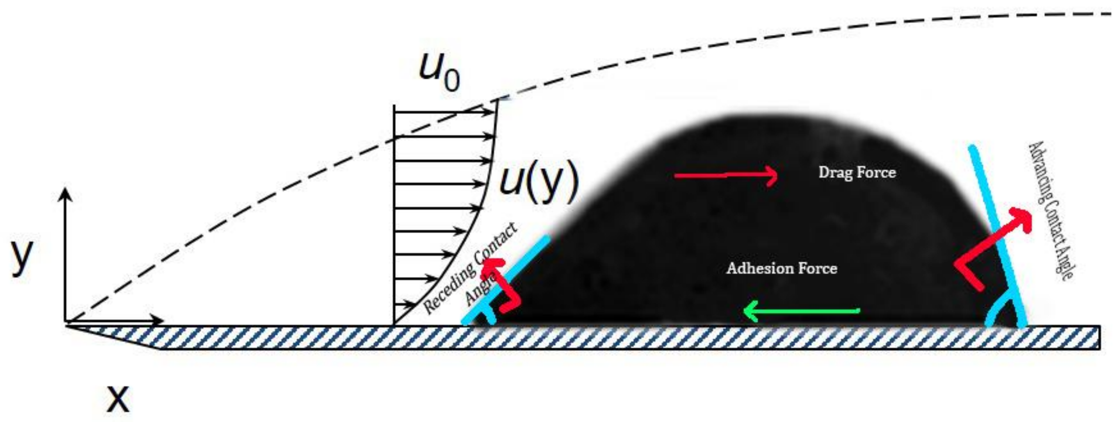

Figure 1-3: A schematic of a droplet located in a boundary layer of an air flow

1.2.2 Air flow over sessile droplets: experimental studies

The experimental studies so far, however providing insightful information, have all failed to provide a comprehensive analysis for the state of the shear flow that causes the shedding of sessile droplets. Using a point wise measurement technique, researchers have been unable to do a thorough investigation on the flow status upstream and downstream the droplet. Consequently, they could only report the free stream velocity which led to the incipient motion of the droplet. The literature refers to this value as the “Critical Air Velocity”. However, the shearing state and the drag force could vary based on the location of the droplet in a boundary layer air flow with a constant free stream velocity. The literature on drop shedding, however, fails to provide information on the state of shearing boundary layer and the location of the droplet with respect to the leading edge. This makes the reported “Critical Air Velocity” values only relatively correct. It means that these values are specific to the experimental setup used. In other words, if the same experiment -for the same liquid and substrate- is done in a different setup would probably have a different local Reynolds number. Consequently, the “critical velocity” values might not be necessarily the same. Thus, the reported critical velocities thus far, are not precisely universal. For these results to be repeatable and universal, a whole flow field investigation is necessity. This way, the critical air velocity is reported alongside the local Reynolds number. This information provided together with the velocity profile in the shearing boundary layer give a comprehensive understanding on the shedding of sessile droplets in different conditions. Plus, with the past investigations, the whole complexities regarding the aerodynamics of a droplet undergoing shedding, e.g., boundary layer effects, vortex shedding, and near wall effects, remained unanswered.

One of the recent studies that addresses droplet shedding is done by Seiler et al. [26]. In their study, they have reported the dynamics of droplet motion (the drop position and velocity) based on the mean flow velocity of a fully developed turbulent flow (being validated by hot-wire measurements) in the channel. They relate the dislodgement of the droplet to the mean flow velocity of the channel which is acceptable for their unique case of study. Because, they have reported the velocity profile inside the channel using hot-wire measurements at different elevations, the velocity profile is known. Plus, due to the presence of a fully developed flow inside the test section, the dependency of droplet shedding on the location is no longer a concern. Thus, the results reported are valid in that they could be repeatable in a different experimental setup which provides the exact same conditions on droplet shedding. However, as the experiment is investigated with a point-wise measurement technique, the various mentioned issues regarding the flow behavior around the droplet are not addressed in the study [26]. Also, they propose a model for a non-dimensional attack velocity. Attack velocity, in their definition, is the velocity of the incoming air velocity at half height of the droplet. This way, the attack velocity could be a representative for the near wall velocity profile that the droplet sees rather than the mean velocity of the flow. However, in their model they use a very simplified model for the adhesion force. This model considers the adhesion force to be as simple as the multiplication of the surface tension and the diameter of a truncated sphere representing the drop shape. This oversimplification leads to inaccurate results for the attack velocity of the droplet by disregarding the distribution of contact angle over the contact line.

In a study by Fan et al. [27] the air velocity needed for the initiation of droplet shedding is reported for various liquids on surfaces with different wettabilities, using an open wind tunnel and a high-speed camera. However, it does not provide information on the state of the flow e.g., velocity profile or what exactly is the velocity they reported (how and where it was measured). It only mentions that the droplet is sitting in a boundary layer –which is obvious- but not addressing the velocity profile. Consequently, even if the reported velocities are measured in the free stream core of the test section the issue of not knowing the local Reynolds number still remains. Plus, like the study done by Seiler et al. [26], it fails to address various phenomena contributing the wake patterns behind the droplet. This is all mainly due to the absence of whole flow field measurement in their investigations. They also used an analytical model showing that the model they used which was derived for the drag force of a solid particle attached to a plane [28] agrees well with the droplets in their study. However, as mentioned earlier, the deformation of a droplet exposed to airflow are so severe that even assuming them as a rigid truncated sphere is not valid. Thus, simplifying them as a solid particle (rigid sphere) could lead to results which are not accurate. Regarding the adhesion force they take a better approach compared to [26]. In their model, Fan et al. [27] considered the contact angle distribution to be equal to the receding angle on the upstream half, and advancing contact angle on the downstream half of the droplet. They also consider the contact angle to be linearly increasing along the contact line from the upstream of the flow to downstream. However, they do not use the correction factor in their simplified models. That makes the adhesion force relations not precisely valid and the drag force relation even more inaccurate. This all leads to a poor correlation and hardly reliable results in regards of droplet incipient motion due to the early mentioned observations made by Antonini et al. [11].

Regarding the experimental studies, one of the notable works so far has been done by Milne and Amirfazli [10]. In their systematic study, the effect of wetting characteristics has been investigated by using various surfaces from hydrophilic to super-hydrophobic. Plus, many simplifications that had been done in the past for modelling the contact line and the distribution of the contact angle are considerably improved leading to more reliable results. However, this study also does not provide the velocity profile and the state of the flow inside the test section. Therefore, the repeatability of the reported results is not guaranteed in other experimental setups with different possible states for the shearing flow. Similar to other studies mentioned before, this study also fails to address the unique state of the flow pattern past the shedding droplets due to the absence of whole flow field measurement. A study by Razzaghi and Amirfazli [29] further points out that it is a requirement to visualize the air flow around sessile droplets and quantitatively study the aerodynamics of the problem affecting the shedding of droplets. In [29] they investigated the critical air velocity for a pair of droplets placed side by side and in tandem arrangements and for various spacing. After a threshold, the interaction of droplets is negligible for the drag force and they are considered as two independent droplets being shed. However, below the threshold, the critical air velocity is different than that of a single droplet and the trends are also different for two arrangements. This implies that the air flow around the droplets is affected by the presence of another droplet. Thus, more forceful airflow is required to impose the same drag force to start the process of droplet shedding depending on the spacing and the arrangement. To justify their results, they used the interaction of side by side and tandem spheres on the flow patterns behind them. That is because, their experimental setup did not provide them with a whole flow field measurement. Thus, likewise other studies, they could only report the free stream velocity that led to the incipient motion of the droplet. More importantly, they used the flow pattern information for the spheres, because there was no information on the flow pattern past shedding droplets to be adapted. This adds to all the justifications why, the investigations on the shedding of sessile droplets should be done using whole flow field measurement. As, not only a whole flow field study to realize the unique state of flow patterns past a shedding droplet is needed but also, this way, a framework for the analysis of aerodynamic interactions of multiple sessile droplets is used.

In conclusion, whole flow field measurement studies of droplet shedding shall be considered as in this way:

1. A detailed information for shearing flow that leads to the incipient motion of the droplet is needed, thus, making the results repeatable and universal with the provided conditions.
2. Various aerodynamic phenomena associated with the shedding of droplets to be addressed e.g., the effect of boundary layer, near wall effects, the effect of three-dimensional separation points, vortex shedding of the oscillating sessile droplet.

3. A comprehensive framework to address the significant differences of multiple sessile droplets being shed to that of a single droplet to be studied.

The most promising technique to study the flow field is Particle Image Velocimetry (PIV) which is a non-intrusive whole flow field measurement technique. A study using PIV could address all the aerodynamics insufficiencies that is found in the literature of droplet shedding.

1.2.3 Air flow over sessile droplets: numerical studies

So far, we have concluded that the experimental studies to date have failed to address various aerodynamics aspects of droplet shedding because of a lack of analysis based on whole flow field investigations. Some aspects of shortcomings in experimental studies are addressed in numerical modeling studies. Having been able to address some aerodynamical aspects for droplet shedding, the numerical studies however have shown to have some issues. The issues associated with the numerical modelling for droplet shedding studies, make the results not quite reliable. There are two main issues with almost all the numerical studies on droplet shedding. Primarily, the simulations are done for 2D droplets. The results would have hold true, if a sessile droplet -in reality- was an infinitely elongated shape of the 2D profile used in numerical simulations. These simulations, then, cannot be regarded as reliable and comprehensive enough as to form the basis knowledge on the aerodynamics of droplet shedding studies. This way, all of the wakes created because of the three-dimensional shape of the droplet cannot be captured. Thus, it only reveals parts of the truth about the nature of flow patterns past the sessile droplet and leaves the rest uncaptured. Another issue with 2D simulations yet is that they disregard the distribution of contact angle along the contact line and the shape of the droplet which affects the drag force as well. Finally, most of these simulations are done for shedding of sessile droplets inside the Gas Diffusion

Layer (GDL) of fuel cells. The air flow of GDL is mostly of low Reynolds number and viscous. Thus, only applies to the aerodynamics of droplet shedding in GDL and cannot be applied to other applications which mostly deal with significantly higher Reynolds numbers.

For example, Dimitrakopoulos and Higdon [30] investigated the displacement of 2D droplets from solid surfaces numerically while considering low Reynolds number shear flow to be the only case. Such simplifications lead to a numerical modeling that could significantly change the results to that expected as explained earlier. In another study, Zhu et al. [31] investigated the emergence of a water droplet through a lateral opening to a microchannel gas stream. They investigated the flow behavior past a 2D droplet which is associated with critical air velocities. In that, they used volume of fluid (VOF) method to explicitly track the liquid-gas interface, giving valuable information on the process. The same critical issues is present in all numerical studies. In a noticeable study by Jarauta et al. [32] an embedded Eulerian-Lagrangian formulation was used to track the fluid-fluid interactions in a droplet shedding process. In this 2D numerical study, Eulerian formulation was used to model the air flow and Lagrangian framework was used to simulate the 2D water droplet. They did an outstanding job on defining the geometry of the water droplet validating the results with experimental observations and considering the oscillations of the water droplet. However, all above studies and several others like them, e.g. [33,34], suffer from the earlier mentioned issues for 2D numerical studies.

this study is no exception in regards of the earlier mentioned issues for numerical studies. This is all the same with several other studies like [33,34].

To circumvent this restriction in numerical studies (the droplets being 2D and the flow being of low Reynolds number), and to further address the phenomena observed in [29], Razzaghi et al. [36] studied the shedding of multiple sessile droplets by air flow. They presented considerably promising results for air flow around “Simulated Droplets”. These simulated droplets are 3D unlike those simulations done in a 2D plane. However, these are rigid droplets not considering severe deformations the droplets go under in this process. This is mainly because, the 3D model of a non-rigid sessile droplet exponentially increases the complexity of the problem to consider the oscillations of droplets in a 3D framework. Consequently, these results, however probably closer to reality, are still not quite comprehensive because of the rigidity of the simulated droplets and ever-present inevitable errors associated with simulations depending on the modeling used. As an example, this study cannot capture the vortex shedding due to the oscillations of the droplet. Plus, because of the deformable state of the droplet, the separation points are different than those of a rigid body. Thus, the wake patterns would be different.

Considering 3D numerical modeling, those simulations studying the air flow over hemispheres could also be informative. Kim and Choi [37] studied laminar flow past a hemisphere up to $Re = 300$ numerically. They found that the unsteady flow past a hemisphere is significantly than that of a sphere. Their study shows a fixed separation point over the hemisphere (90°) for $100 \leq Re \leq 300$ which is quite different from the flow past a sphere. They found the transition of the flow from “steady axisymmetric” to “unsteady (aperiodic in time) asymmetric” to be happening quite sooner compared to flow over a sphere. Such that after a Reynolds number of 280 the flow is completely unsteady and asymmetric. They also reported that the drag coefficient decreases with increasing the Reynolds number.

Finally, even if numerical studies of 3D sessile droplets exposed to air flow are carried out, there needs to be a universal, reliable experimental study in regards of droplet shedding for the numerical results to be validated with.

1.2.4 PIV studies on air flow over rigid bodies

As there are no droplet shedding studies using PIV technique in literature, we examine studies concerning the dynamics of air flow around objects in boundary layer and more specifically of those wall-mounted objects. Jang and Lee [18] found it necessary to go beyond the point-measurement experimental investigations and numerical studies and studied the wakes behind a sphere at high Reynolds numbers using PIV. However, finding it difficult to track the velocity beside the sphere (due to low tracer particle density in that area), they were able to quantify the large scale and small-scale vortices behind the sphere at $Re = 11000$ in a circulating water channel. They obtained 500 instantaneous velocity fields each giving 4096 velocity vectors across the field. With these, they were able to analyze the formation and shedding of vortices behind the sphere where point-wise measurements and conventional flow visualization failed to provide the spatial quantitative data. Plus, these results would be a basis for numerical methods to be validated making their results reliable for various numerical cases of study upon validation. Being quite remarkable with their promising results for near wake studies, this study however, is one of many studies that considers the fluid-structure interactions out of the boundary layer. In other words, the object is exposed to the free stream of fluid and avoids near-surface effects as complexities (also because of different objectives these studies have). This is addressed by Ozgoren et al. [19] in which a Rhodamine dye injection technique and PIV technique was used. The objective was to qualitatively observe and quantitatively investigate the water flow around a sphere located in a boundary layer, with the sphere being placed at different distances from the plate. Thus, primarily, they investigated the effects of non-uniform incoming velocity and near surface effects on the wake formation and shedding of the vortices behind the rigid sphere. To that end, they used velocity fields, patterns of sectional streamlines, vorticity contours, and distributions of velocity fluctuations namely all obtained by PIV data. Their results indicate a substantial difference when the spacing between the sphere and the plate is changed at the same longitudinal location in a boundary layer. The differences are evident in wake patterns and thus the quality of the flow around the sphere. For instance, they have reported that when the sphere is located on the surface ($^{G\ (Gap)}/_{D\ (Sphere\ Diameter)} = 0$) the fluid flow is blocked downwards because of the contact point the sphere makes with the plate. This makes the vortices to be shed only from the top as the shedding of vortices is being prevented on the lower section. Then, clockwise vortices with helical form are shed on the top section of the sphere downstream of the flow. Plus, because the sphere is being placed in the boundary layer (non-uniformity of the incoming velocity) various small eddies are formed around and in the larger vortices downstream due to Kelvin-Helmholtz instability in the boundary layer region. They have also observed that due to the three-dimensional separation the entrainment of the flow downstream the sphere is magnified, thus, making many small eddies behind the sphere. This, yet, adds to all the reasons why a two-dimensional numerical modeling of the flow around droplet is not quite promising. It is also inferred, that as the gap between the sphere and the plate is reduced, the wake patterns become asymmetrical. Consequently, when the sphere is located on the plane, the most asymmetric patterns of wakes and vortex shedding is observed. This is so significant that at some Reynolds numbers for $^{G}/_{D} = 0$, there is only one large clock-wise vortex created behind the sphere not resembling a symmetrical horseshoe vortex. This is the case, while a horseshoe vortex is mostly present behind a sphere subject to free stream without the near surface effects being present. There are also the instabilities inside the boundary layer that leads to different wake patterns around the sphere, e.g., different separation points. However, getting average over hundreds of consecutive velocity fields derived from consecutive pairs of particle images, gives time averaged streamline patterns and vortices to have a generalized analysis on the problem. This, all implies that the generalization of the dynamics of the air flow around objects when they are suspended and far from the boundary layer would not lead to accurate interpretations of those inside the boundary layer and attached to the wall. Likewise, the study of aerodynamics of sessile droplet shedding cannot be simplified to the dynamics of air flow over suspended droplets. In other words, the near surface difficulties associated with such studies (shedding of sessile droplets) cannot be avoided this way.

Ozgoren et al.'s [19] results for a sphere attached to a wall, cannot be directly related to sessile droplet shedding for two reasons. Firstly, it is the shape of the object which may approximately apply only to those droplets with very high advancing and receding contact angles (drops lying on superhydrophobic surfaces). Secondly, it is the oscillations of the droplets that will be overlooked this way and thus significantly affect the outcome.

Amongst common rigid bodies, over which the air flow is studied, the closest shape to a sessile droplet is hemisphere. Johnson and Thurow [38] studied the volumetric flow in the wake of a hemisphere using plenoptic particle image velocimetry. The Reynolds number (based on hemisphere height) was 4570 and the boundary layer thickness to hemisphere height ratio was 2.4. Their main objective was to study the topology of large-scale vortices in the wake of a hemisphere immersed in a turbulent boundary layer. They studied 986 instantaneous velocity fields and observed a variety of phenomena, depicting the unsteady nature of the flow.

There are also other PIV studies concerning the dynamics of the air flow around wall mounted objects which are not droplet like, e.g., air flow behind surface mounted permeable ribs by Panigrahi et al. [39]. Their focus was mostly the differences of flow patterns behind various permeable ribs and comparing them with the flow behind a solid rib. This study, also, indicated that behind a solid rib a considerably large “recirculation bubble focus” is made behind the rib which excels the counter-clockwise focus made on the lower section in size. Also, unlike the mentioned studies thus far, which were conducted in water channel, this study concerns the air flow around a surface mounted object. However, the results cannot be applied to droplet shedding directly due to the reasons mentioned earlier. This is also evident in a study by Wang et al. [40] in which the dynamics of the flow inside a square channel with periodic ribs on one wall were investigated using 2D PIV in vertical and horizontal planes. The focus was on the turbulence mechanism associated with separation, reattachment, and subsequent redevelopment of the flow. This gives insights about the development of the wakes behind periodic ribs, however, as the distance between the ribs is constant and the study has not focused on the effect of ribs spacing on the wake patterns and dynamics of the flow, it cannot give clues on the effect of droplets proximity on the incipient motion. In another PIV study by Panigrahi [41] investigating the flow around wall mounted and detached square cylinders, the effect of wall on the flow pattern behind an object was investigated. The results indicate that considerably different wake patterns behind ribs with different vertical distance from a horizontal surface is present.

On the influence of the proximity of droplets on the air flow and thus the critical air velocity, similar studies for spheres have been done using PIV technique [42,43]. However, as the spheres are not located in a boundary layer and the near-surface effects are not present the results cannot be applied to a typical droplet shedding problem directly. This is, in addition to their rigid shape which is not close to a deformed non-rigid droplet sitting on a plate being exposed to a non-uniform velocity in a boundary layer. In summary, it should be noted that these studies which are considerably different than droplet shedding studies, considering their scale, shapes, deformability, or even the fluid, are the closest studies to droplet shedding in PIV investigations. In these studies, it has been clearly pointed out that how much various conditions e.g. boundary layer, near surface effects, 3D separations points, could be defining in an aerodynamics problem. Plus, the fact that all these aspects can be investigated using Particle Image Velocimetry.

1.3 Scope of thesis

Despite various great studies in the field of sessile droplet shedding, many questions become unanswered in this field. Especially, due to absence of whole-flow-field experimental studies for shedding of sessile droplets, and the shortcomings of numerical studies, certain studies in this regard should be done. The studies need to address various aspect, yet not systematically addressed so far. Of those many, some are listed below:

- Understanding the effect of wettability (from hydrophilic to superhydrophobic) on air flow structure
- Understanding the effect of drop size on air flow structure
- Understanding the effect of wettability (from hydrophilic to superhydrophobic) on coefficient of pressure
- Understanding the effect of drop size on air flow structure
- Understanding the effect of wettability (from hydrophilic to superhydrophobic) on turbulence
- Understanding the effect of drop size on turbulence intensity in the flow field
- Understanding the effect of drop oscillations on air flow structure for different surface wettabilities at different accelerations for air velocity
- Understanding the effect of drop oscillations on air flow structure for different drop sizes at different accelerations for air velocity

- Understanding the effect of droplets proximity on changing the air flow structure for droplets on different surface wettabilities (for different arrangements e.g., side by side, and tandem)
- Understanding the effect of droplets proximity on changing the air flow structure for different drop sizes (for different arrangements e.g., side by side, and tandem)
- Understanding the effect of droplets proximity on changing the pressure coefficient for droplets on different surface wettabilities (for different arrangements e.g., side by side, and tandem)
- Understanding the effect of droplets proximity on changing the pressure coefficient for different drop sizes (for different arrangements e.g., side by side, and tandem)
- Understanding the effect of droplets proximity on changing the turbulence for droplets on different surface wettabilities (for different arrangements e.g., side by side, and tandem)
- Understanding the effect of droplets proximity on changing the turbulence for different drop sizes (for different arrangements e.g., side by side, and tandem)

However, these are only some of the questions that are to be addressed. And the studies need to provide understanding on the 3D flow or at different planes.

The current study is an attempt to address the air flow field characteristics, e.g., velocity, pressure, and turbulence statistics, in a plane that bisects a sessile droplet streamwise. The air flow is studied around a single sessile droplet of the size 10 μl, 20 μl, and 30 μl. Reynolds numbers based on free stream velocities and droplet heights are in the range of $600 < Re_h \leq 1000$. Reynolds numbers based on free stream velocities and the position of the droplet with respect to the leading edge of the aerodynamic deck (which is set at a constant value of 10 cm) are in the range of

$3 \times 10^4 \leq Re_x \leq -7.2 \times 10^4$. Thus, the droplets are exposed to laminar boundary layer flow. The field of view spans more than $4 \times Droplet\ Contact\ length$, and $4 \times Drop\ Height$ in length and width, respectively, for all the cases. The surface wettabilities were chosen from hydrophilic to hydrophobic such that the effect of surface wettability on air flow over sessile droplets is examined (through changing the shape of the droplet and contact angle hysteresis). Also, for each wettability, the experiments were done for droplets in different sizes to understand the effect of droplet size on air flow characteristics for each surface wettability. The effect of oscillations is only seen for the droplets at the verge of shedding for which the air velocity is slowly accelerated ($2.8\,\frac{m/s}{min}$) to reach to that value (slightly below the critical air velocity).

1.4 Objectives

Objectives of this thesis are listed below:

1. To design, fabricate and set-up a PIV experimental setup to make systematic whole-flow-field studies on the boundary layer and air flow over sessile droplets possible
2. To understand the effect of surface wettability on the structure of air flow (streamlines, velocity contours, velocity profiles, vorticity contours, and recirculation lengths for upstream, on, and downstream the sessile droplet for each drop size)
3. To understand the effect of drop size on the structure of air flow
4. To understand the effect of drop oscillations on the air flow structure
5. To understand the effect of surface wettability on the pressure around sessile droplets
6. To understand the effect of drop size on the pressure around sessile droplets
7. To understand the effect of wettability on the turbulence statistics of the flow over a sessile droplet
8. To understand the effect of drop size on the turbulence statistics of the flow over a sessile droplet
9. To understand the effect of drop oscillations on the turbulence statistics of the flow over a sessile droplet

2 Experimental setup: design and fabrication

2.1 Wind Tunnel

Wind Tunnels are designed to provide uniform velocity and straight air flow inside their test section. Wind tunnels are categorized based on the velocity in the test section and the circuit for the air. Wind tunnels are subsonic (M < .8), transonic (.8 < M < 1.2), supersonic (1.2 < M < 5.0), or hypersonic (M > 5.0) considering the velocity criterion. Wind tunnel in this study is a low speed ($M < 0.3$) one i.e. subsonic. Considering the air circuit, wind tunnels are either “Open Circuit” or “Closed Circuit”. “Open Circuit” wind tunnels take the surrounding air and run it through the test section and then exhaust the air to the open space through the outlet. The air that is drawn to the wind tunnel could be either from the outdoor or a laboratory. There are suck-down tunnels in which the is air sucked through the tunnel using a fan downstream of the test section. If the fan is placed upstream of the test section, it blows the air inside the test section making the wind tunnel a blower tunnel. Wind tunnels which circulate the air through a loop are called “Closed Circuit” wind tunnels. In general, one could say that “Closed Circuit” wind tunnels provide more uniform air flow inside the test section than open circuit wind tunnels [44]. As the emphasis in most of the studies is on wind tunnels with low levels of turbulence and unsteadiness, most of the high performance and large wind tunnels setups are designed as a closed-circuit type. In this study, as the air flow speed needed inside the test section is not required to exceed $20\ {}^{m}/_{s}$ [10, 36] ($M = 0.0725 < 0.3$), a low-speed wind tunnel was needed to be designed. Consequently, a closed-circuit wind tunnel was chosen to be built given better flow quality expected. Figure 2-1 illustrates different types of low speed wind tunnels. The details about certain elements of the designed wind tunnel is explained here accordingly.

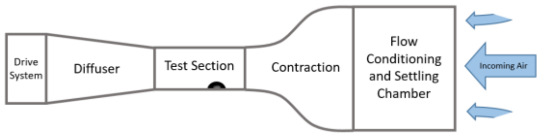

A

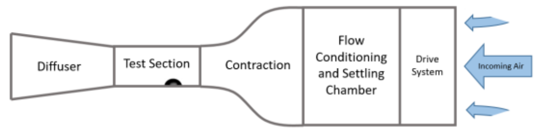

b

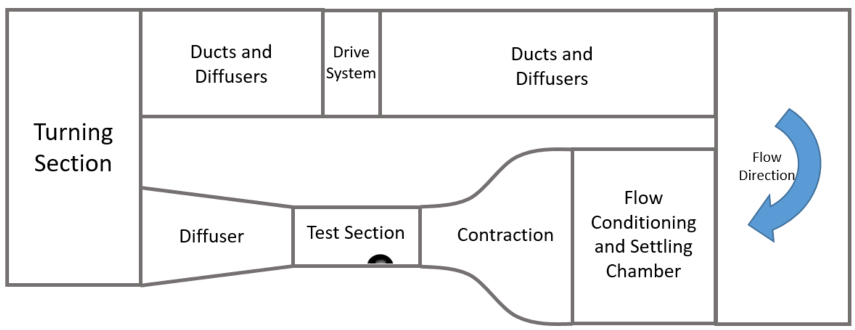

c

Figure 2-1. Schematics of different types of low speed wind tunnels. a) Suction open wind tunnel b) Blow-down open wind tunnel c) Closed wind tunnel

2.1.1 Test Section

One should be quite diligent in defining test section dimensions as it would affect the whole setup and more importantly the quality of air in regions of interest. In a previous study by Milne and Amirfazli [10] a free stream velocity of $0 - 20\ {}^{m}/_{s}$ was found to be sufficient to shed sessile droplets from various surfaces. It is necessary for the area of interest to lie in a region in which there is no boundary layer upstream as it adds several unknowns to the study making the investigation less systematic. Thus, a test section is needed which can provide uniform air flow over a plate, for velocities of $0 - 20\ {}^{m}/_{s}$. Then we should derive the formula that relates the dimensions of the test section to the quality of the air flow using fluid dynamics. The details for calculating the boundary layer development inside the test section is given in section AA.1, then the dimensions of the test section were defined as $11\ (w) \times 8(h) \times 30\ (l)\ cm^3$. Figure 2-2 shows the designed geometry of the test section used for the wind tunnel.

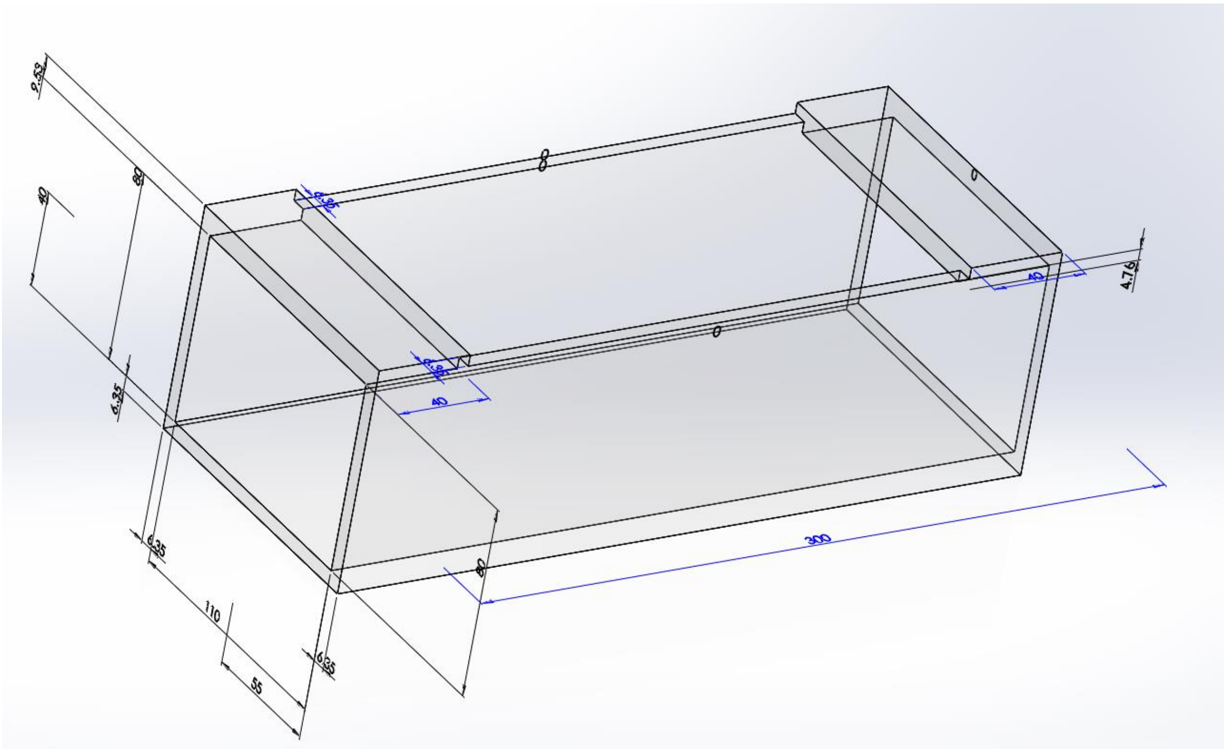

Figure 2-2. The dimensions of the test section of the designed wind tunnel

2.1.2 Contraction Zone

The most critical part of a wind tunnel is the "contraction zone". Contraction zone accelerates the flow to the test section while reducing axial turbulence fluctuations and increasing lateral turbulence. The most important factor about a contraction zone is the contraction ratio which is defined as [44]:

$$N = \frac{A_{CZ_{entrance}}}{A_{TS_{entrance}}} \tag{2-1}$$

In which, “N” is the contraction ratio while “$A_{CZ_{entrance}}$”, and “$A_{TS_{entrance}}$” are the entrance areas of contraction zone and test section respectively. The rule of thumb for contraction ratio is that, the larger the contraction ratio, the more uniform the flow inside the test section [44]. However, like many engineering design problems there is a compromise in defining the contraction. That being the higher costs and overall larger components for the wind tunnel that is associated with larger contraction ratios. Plus, quite high contraction ratios might lead to noise problems and possible separation at the end of the contraction zone [44].

In accordance with Batchelor [45], if a contraction chamber with a contraction ratio of N is used, then turbulent quantities can be reduced by the factors of:

u-Component mean velocity: $^1/_N$ (2-2)

v or w-component mean velocity: $\sqrt{N}$ (2-3)

u-component rms intensity: $\frac{\sqrt{3(ln\,4N^3-1)}}{2N}$ (2-4)

v or w component rms intensity: $\frac{\sqrt{3N}}{2}$ (2-5)

In which u, v, and w are x-velocity, y-velocity, and z-velocity components, respectively. According to Mehta and Bradshaw [44] contraction ratios between 6-9 are mostly used for the wind tunnels (specially for smaller wind tunnels).

A contraction ratio of 8.04 was chosen for the wind tunnel which conformed to the dimensions for 3D-printing the contraction chamber with MakerBot Z18 3D printer (see appendix B.3). The dimensions, also, did not give rise to unreasonably large components for the wind tunnel and provide uniform air flow for the test section with considerably low levels of velocity variations.

The length of the contraction section also dictates the quality of the flow. A short length causes adverse pressure gradients leading to flow separation; a long segment causes significant boundary layer development along the walls.

One must also consider the shape of the contraction section. One might think of the shape of the contraction chamber as a “nozzle” to increase the velocity by reducing the pressure. But one must be aware of possible adverse pressure gradients and less uniform velocity profile associated with a simple straight wall nozzle. According to Mehta and Bradshaw [44] “The old-style contraction shape with a small radius of curvature at the wide end and a large radius at the narrow end to provide a gentle entry to the test section is not the optimum”. There is a danger of boundary-layer separation at the wide end, or perturbation of the flow through the last screen. Good practice is to make the ratio of the radius of curvature to the flow width about the same at each end.

The profile developed by Bell and Mehta [47] was such that low boundary layer development and little risk of air flow separation in contraction zone was expected. The profile is described as a fifth order polynomial has become a design standard [48]:

$$h = [-10\xi^3 + 15\xi^4 - 6\xi^5](H_i - H_o) + H_i \tag{2-6}$$

Where h is the is the current y position for a certain ξ in a x-y-diagram, H_i is the curve height at the inlet of the contraction, H_o is the height at the outlet and $\xi = {}^{X}/_{L}$, where L is the overall length of the contraction zone. The profile is shown in Figure 2-3. The final design of the contraction chamber conforming to all the design considerations is shown in Figure 2-4.

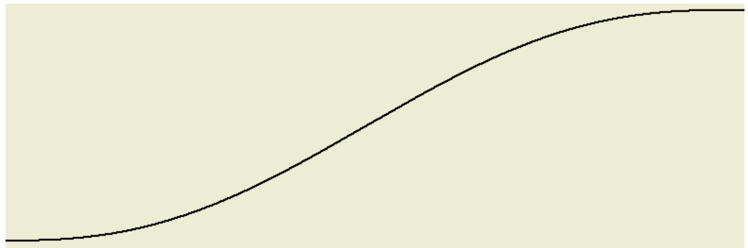

Figure 2-3. Contraction zone: curved shape

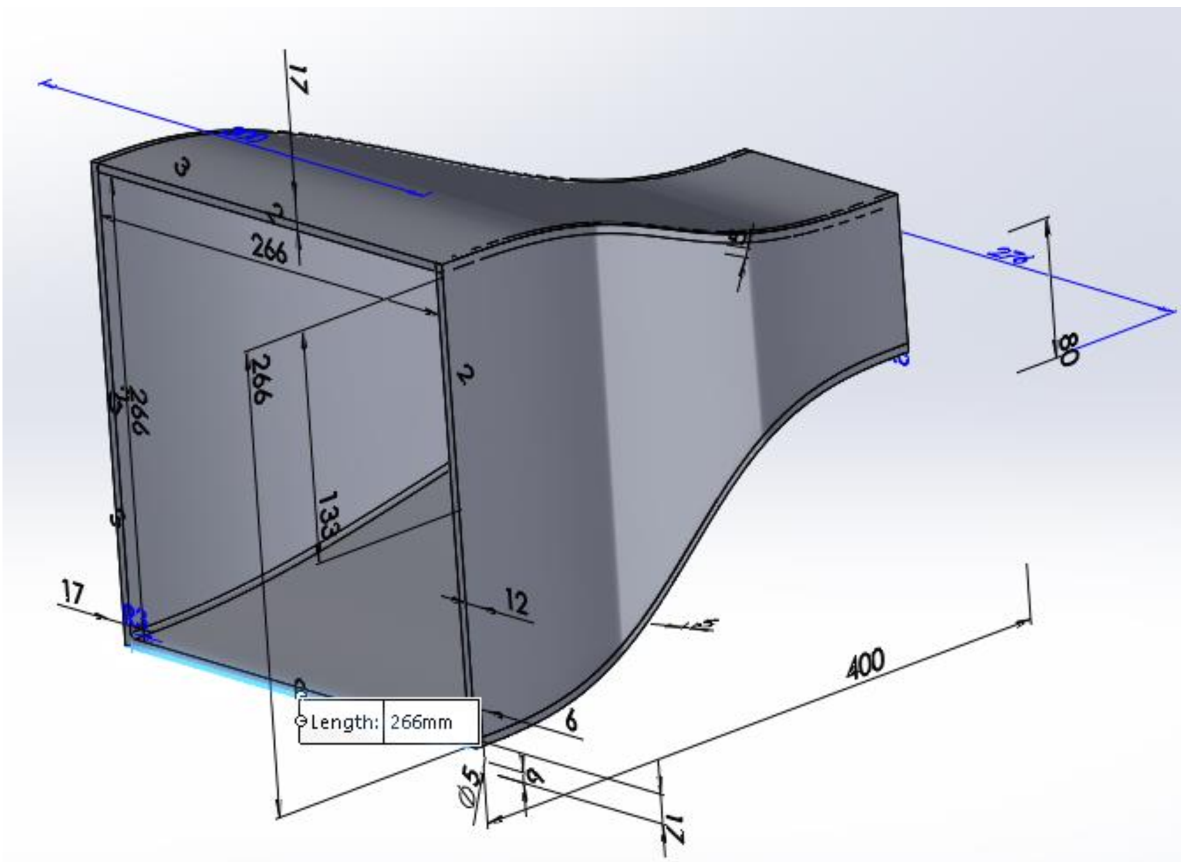

Figure 2-4. Design of the contraction segment

2.1.3 Flow Conditioning and Settling Chamber

Passing through the diffusers, corners, and other elements in the wind tunnel, instabilities are added to the flow, which need to be eliminated. That is due to requirements of the test section, which requires the flow to have the lowest boundary layer and turbulence. The huge boundary layer created through the loop and the turbulence of the flow, then need to be eliminated in a station before the test section. This station is called the “flow conditioning zone”, “settling chamber” or a combination of both. Calling the whole zone “settling chamber” is not really preferred much as, technically, settling chamber is only a part of this whole section. The position of flow condition zone is after the last corner and before the contraction zone [44]. This way the developed boundary layer thickness is reduced or ideally perished, and the turbulence of the flow is the least before getting into the test section. Knowing where to place the flow conditioning zone, now, its elements are explained in the following sub-sections.

2.1.3.1 Screens

Screens assist in reducing the boundary layer thickness to make the flow velocity profile more uniform. This is achieved by the pressure drop that is associated with this component and is proportional to $(Speed)^2$. If the pressure drop coefficient for this component is conventionally denoted by K, it is believed that when $\mathrm{K} = 2$, all variations in the longitudinal mean velocity is removed [44]. Plus, the turbulence intensity is reduced in the whole flow field as the flow passes a screen [44]. The pressure drop coefficient for screens is calculated via different empirical relations suggested by various studies in literature [44, 46] in which the dominant parameter is the open area ratio (β). One of the mostly used relations is [44]:

$$K = \frac{1-\beta}{\beta^2} \tag{2-7}$$

It has been recommended in [44] to use a mesh as small as possible for a given open area ratio as it would be more efficient in reducing the pre-existing turbulence. From the equation (2-7) it is inferred that the smaller the open area ratio (β), the higher the pressure drop coefficient, thus, a more uniform flow at the end. But the following constraints should be considered:

i. Power of fan should be considered

ii. More importantly, below a threshold there is going to be some turbulence produced by the screens because of the unreasonably low open area. [44, 46]

The threshold is reported to be $\beta = \%57$ by various studies [44, 46]. Thus, screens (each with open area ratios higher than $\%57$) with cumulative pressure drop coefficient of ~ 2 were used. This would be optimal to eliminate almost all the pre-existing turbulence and reduce the variations of longitudinal mean velocity of satisfactory level with reasonable pressure drop. Considering above, two screens for which the specifications are given in Table 2-1 were chosen.

Table 2-1 The specifications of the selected screens for the flow conditioning chamber

Screens	**Mesh Size**	**Opening Size**	**Open Area Ratio β**	**Wire Diameter**	**Pressure Drop Coefficient K**
1st Screen	32*32	0.025”	63%	0.0065”	0.932
2nd Screen	38*38	0.02”	57%	0.0065”	1.323

These screens will give a pressure drop coefficient more than K=2 combined, which conforms to the considerations formerly stated. It is the best practice, if the coarsest screen is placed upstream and the finest, downstream before the settling area, which is the case for the designed wind tunnel [42].

2.1.3.2 Honeycombs

Honeycombs are mostly used to remove swirls and lateral mean velocity variation of the flow. This is done effectively when the yaw angle of the flow is less than $10°$ [44]. Otherwise, the flow in cells "stall", adding turbulence to the flow and causing further pressure drop. The complete removal of the turbulence is achieved by a length of $5 - 10$ cell diameters [44]. The shape of the cells is mostly hexagonal but could also be circular or square-shaped for ease of construction. Aluminum honeycombs used for aircraft sandwich construction have more precise dimensions than otherwise made honeycombs like those made by paper. Based on the smallest available cell size in the market ($1.27\ cm$) , three layers of honeycombs with cell sizes of $1.27\ cm$ were placed in the flow conditioning zone each having a thickness of $1.9\ cm$. The arrangement of the honeycombs and screens inside the flow condition and settling chamber is in a way that the coarsest screen is placed upstream and the finest screen is placed downstream. The settling zone is after the finest screen with a length of 20 percent of the hydrodynamic diameter of the flow condition chamber [44]. The distances between the screens and the honeycombs are accordingly set not to add turbulence to the flow and for the flow to decay certain turbulence after the element [44]. The honeycombs used is shown in Figure 2-5.

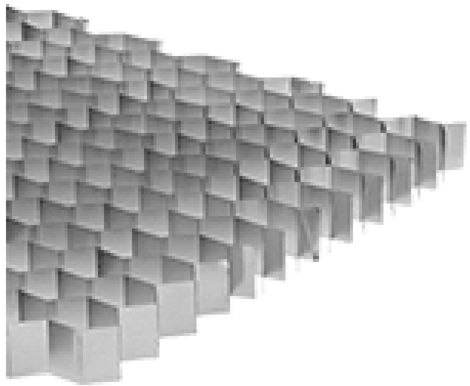

Figure 2-5. The honeycombs used inside the flow conditioning zone (the picture is used with permission from McMaster-Carr)

2.1.4 Corners

For a wind tunnel to perform as closed-circuit, there needs to be certain number of corners. Corners are not a simple 90° straight wall bends. This is so for two reasons:

i. Avoidance to add unnecessary turbulence to the flow

ii. To minimize the pressure drop

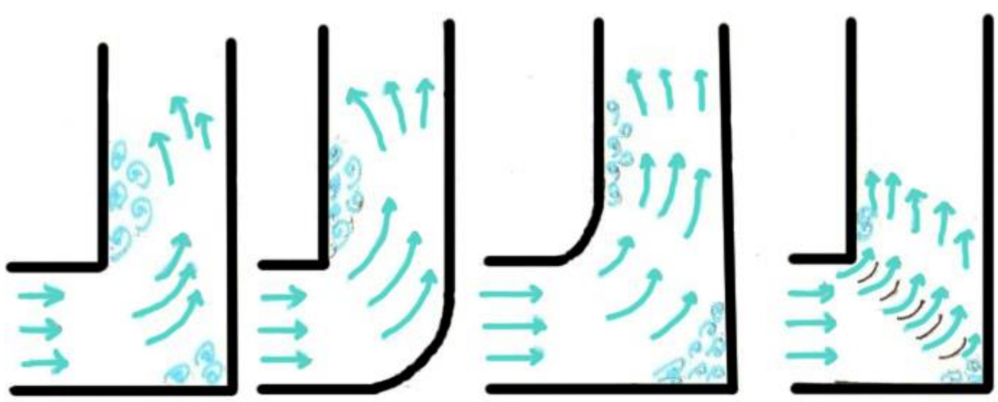

Figure 2-6. Schematics for turbulence level in various elbow designs

Figure 2-6 illustrates the severity of the turbulence made by sharp elbows. As shown in Figure 2-6, the turbulence caused by elbows can be reduced using corner vanes. These vanes are used to guide the airflow around the 90° corners. To achieve a better turning duct, yet, one could apply these corner vanes inside a curved elbow (with round heals and throats). This way, the lowest pressure drop with the most insignificant turbulence is achieved through using the corners. Plus, using corner vanes avoids boundary layer separation and maintains flow uniformity throughout the corners.

On the geometry of the vanes, the usual practice is to make the vane as a circular arc, with short straight extensions at the leading edge [44, 46]. The trailing edge of the vanes is aligned parallel with the axis of the downstream duct while it is suggested to set the leading edge at a positive "angle of incidence" of 4° with the axis of the upstream leg [44]. The designed corners (curved elbows with turning vanes) is shown in Figure 2-7.

A

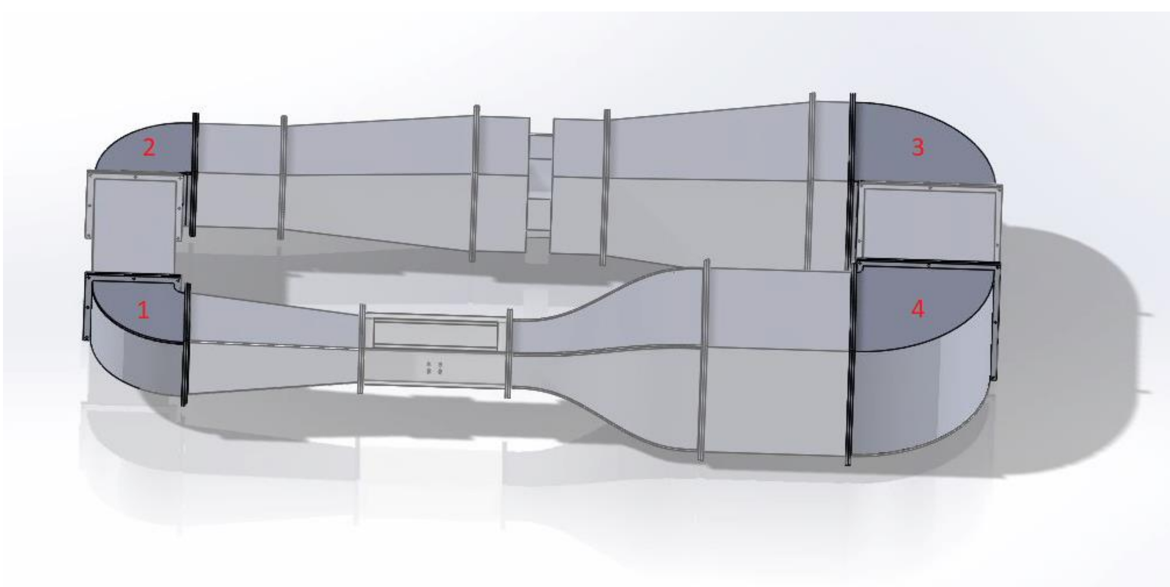

Continues next page…

B c

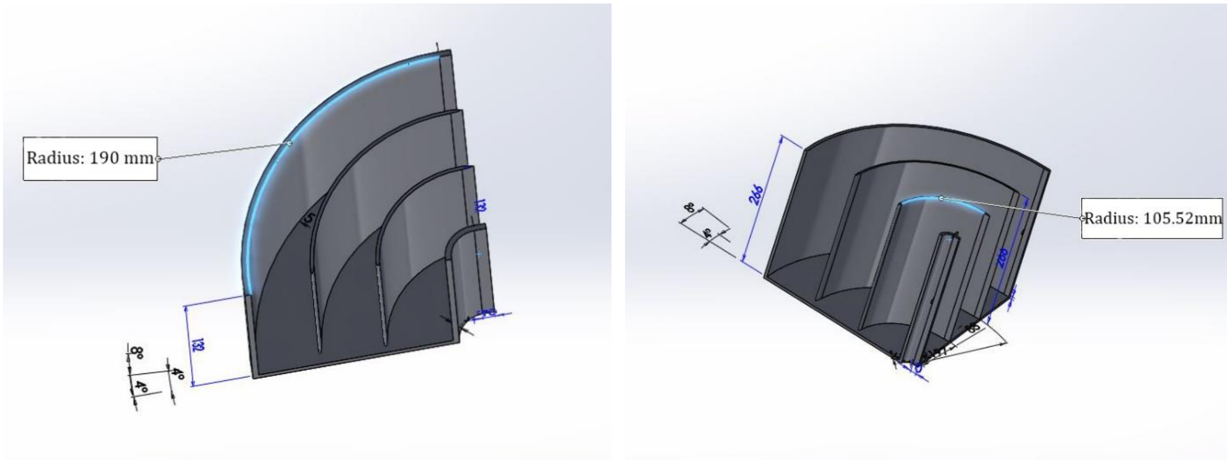

Figure 2-7. a) curved elbows used in the wind tunnel. b) The geometry of the second small elbow (with the designed turning vanes) c) The geometry of the second large elbow (fourth elbow) (with the designed turning vanes)

2.1.1 Diffusers

Diffusers play an important role in wind tunnels as they provide static pressure recovery and join small test sections to several times (depending on the contraction ratio) larger settling chambers. They also reduce the load of the fan which is important especially when axial fans are used. The flow inside a diffuser varies based on the diffuser geometry defined by the area ratio, diffuser angle (2θ), wall contour and the diffuser cross sectional shapes. It is also the initial conditions, boundary layer control method and the presence of separation which could affect the flow through the diffusers. All that, makes the prediction of flow inside the diffusers very difficult. That is why almost all of the information on diffusers in wind tunnels are empirical. The diffusers in wind tunnels are generally two types: small angle diffusers, and wide-angle diffusers. Wide-angle diffusers are used when the space is limited. The abruptly expanding profile of a wide-angle diffuser causes flow separation which is undesirable in wind tunnels. To fix this issue with wide angle diffusers, several screens, based on the area ratio and the diffuser angle should be placed inside the diffuser. The design rules on the screen spacings and which screens (pressure drop coefficient values) to use are found in [44].

For the current wind tunnel, the design criteria is such that quite high velocities inside the test section is needed ($20\ {}^{m}/_{s}$). For the diffuser which is placed right after the test section, the dynamic pressure could be very high which results in significantly high pressure drops while the screens are used. Also, since an axial fan was used, total pressure available is a constraint. Consequently, it had been decided not to use the wide-angle diffusers. Then, with the use of small angle diffusers, the wind tunnel was supposedly to be made longer compared to when the wide-angle diffusers are used. However, after iterative rough calculations, it was decided to use a diffuser after the test section only long enough to decrease the dynamic pressure such that the pressure drop in the small corners is reasonable. Then, a few other diffusers could be placed in the second half of the loop. This makes the wind tunnel considerably smaller than a wind tunnel in which a very long diffuser is attached to the test section and a straight duct is placed in the second half of the loop.

The first diffuser -which is connected to the test section- is the most important one. In case of a flow separation, the pressure pulsation is transmitted upstream to the test section. Then the tests performed in the test section would be affected by pressure and velocity non-uniformities. Based on empirical results on the small angle diffusers, it has been stated that the diffuser angle (2θ) should not exceed 10° to avoid the possible adverse pressure and flow separation [44]. Three small angle diffusers were used in the wind tunnel to completely recover the static pressure and to efficiently make the wind tunnel as small as possible. The diffusers are shown in Figure 2-8.

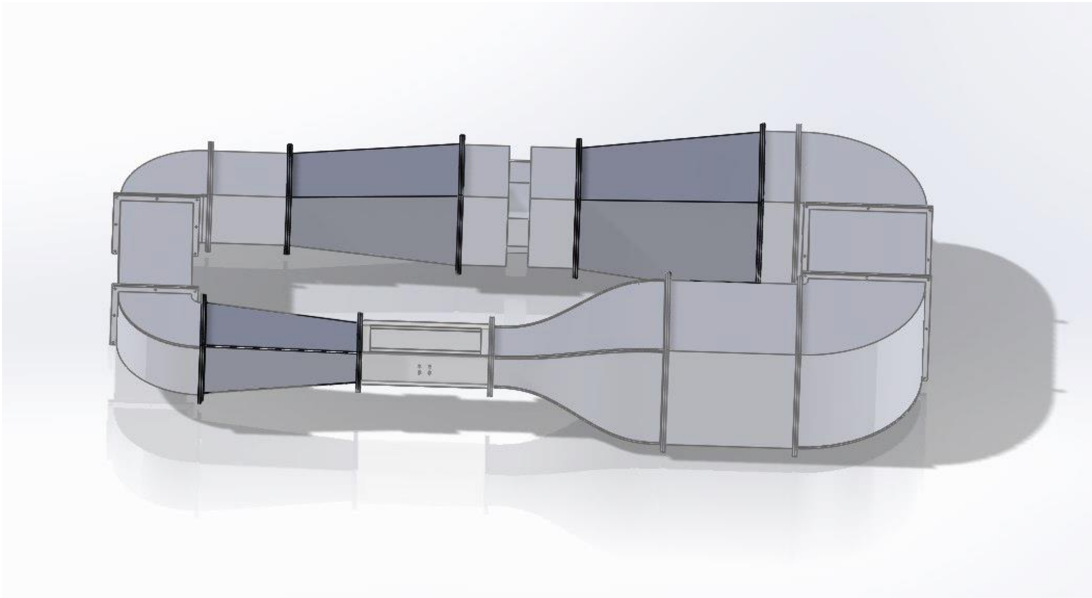

Figure 2-8. The small angle diffusers (darker color segments) used in the wind tunnel

2.1.2 Driving system

Two primary drive systems are commonly used for wind tunnels i.e. fans and compressors. Fans, which could be either axial or centrifugal, push/pull air through the test section. Compressors, on the other hand, use pressurized air from storage tanks and provide it to the tunnel through controlled valve or regulator. With the compressors, one could expect high pressure ratios, thus, they could basically be used for high speed facilities. However, the issue with the compressors is that they are limited regarding the duration of test run. Based on the storage capacity, the compressors could perform only for a couple of minutes in a single run. Given the conditions which does not require high velocities and the preference for the wind tunnel to be able to operate constantly for long runs, an axial fan was chosen. The only drawback of axial fans could have been the high cost which was not really the case for this tunnel (~$200). Given the calculations on the pressure drop for required head/flowrate, an axial fan from Ebmpapst was selected (2214 F/2 TDHH0). Further information on the system (axial fan) could be found in section B.1.

2.1.3 Plate inside test section

In order to place the substrates in the middle of test section (to have control over the growing boundary layer) an aerodynamical plate (deck) was designed. Figure 2-9 shows the designed plate. There is a slot made to fit the substrates flush so that the flow quality being exposed to droplets meet the requirements. The left side of the plate (leading edge) shown in Figure 2-9 faces the upstream of the flow in test section. The aerodynamical shape of the leading edge was designed asymmetrical based on the recommendations by Hanson et al. [49] (A3 profile). Also, to control the stagnation point, a flap with the angle of 3° (to make sure that a back flow does not happen) was considered [49] downstream of the plate.

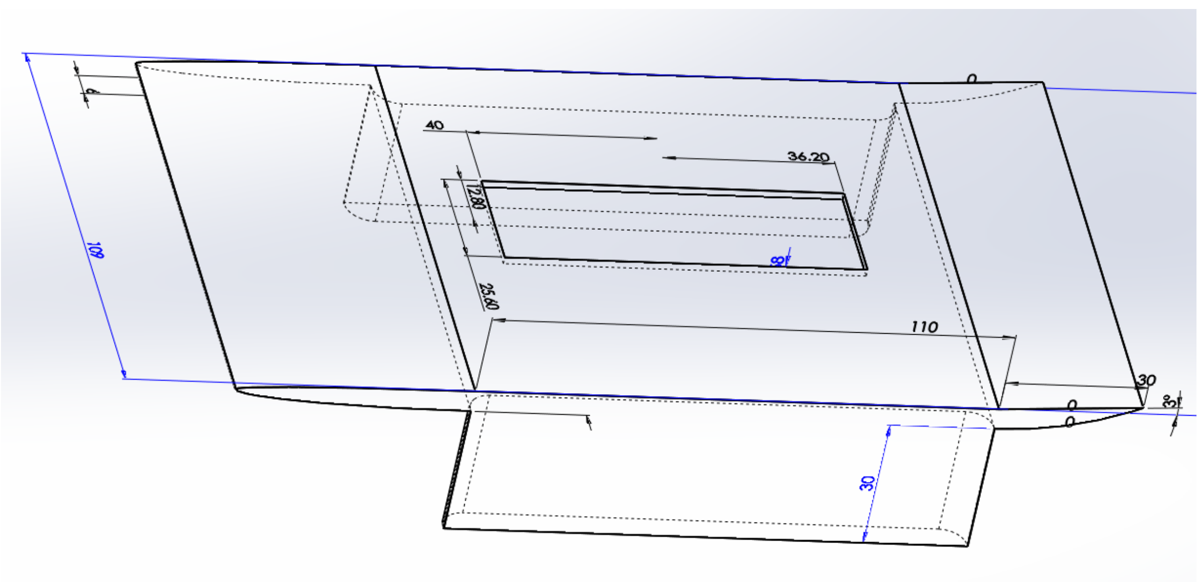

Figure 2-9. The designed plate to put in the test section

2.1.4 Fabrication

To fabricate the wind tunnel, different materials and procedures were used. Optical access to the test section needs to cause the least optical distortion and conform to the requirements of the laser light passing through them for the PIV application. The laser light sheet passing through the windows should experience as little reflection and refraction as possible. Also, the test section material should tolerate the heat from the laser sheet. The chosen material to fabricate the test section was Borosilicate glass sheets, which are annealed through the fabrication process and are exceptionally tolerant to heat. This, beside the clear, undistorted view that they provide, makes the annealed Borosilicate glass sheets a very good candidate for high-temperature viewports and the current application i.e. PIV. The glass sheets were cut to size, then glued together using silicone glue.

The ducts were sorted into two groups: The ones which either had an elaborate geometry or their profile was very critical for the intended uniform flow in the test section. The second group included the ducts for which the shape was simple and the flow quality was not as critical as the first group. The ducts in the first group were 3D-printed using the CAD models and the MakerBot Z18 from the department (see appendix B.3 for specifications). The plate inside the test section was also 3D printed. PLA was used as the filament for 3D-printing the elements in the first group e.g., elbows with the turning vanes, contraction chamber and the first diffuser. For the ducts in the second group, Polyethylene sheets were cut using a laser cutter and then glued using the appropriate epoxy (JB Weld – 50133F). Polyethylene sheets have a low friction. They are impact resistant, wear resistant and reasonably chemically resistant. This makes them a good choice for fabricating the ducts. To fabricate the ducts out of the laser-cut Polyethylene sheets, the locations of bonding were sufficiently roughened using coarse sandpapers (40- to 60-grit) (to make the bonds strong). It is also worth mentioning that Polyethylene are not as easily cut by laser cutters as they are Thermoplastics. To that end, the laser cutter was used to cut the sheets halfway and more importantly to mark the outline based on the CAD models. The sheets were completely cut using common cutters then.

Several flanges were used to join the ducts together. For the wind tunnel to be made modular, the flanges were glued to the both ends of a duct, then, the flanges were connected using several screws and nuts; to make the airtight connections using rubber gaskets between the connecting flanges, rubbers were put in between. Flanges were cut from 7 mm thick aluminum sheets. To cut the inner square of the flanges, using manual cutting tools, one should be quite diligent not to distort the thin sheet, and to cut the profile such that there is no protrusion in the flow. A schematic of the CAD model of the closed wind tunnel is shown in Figure 2-10.

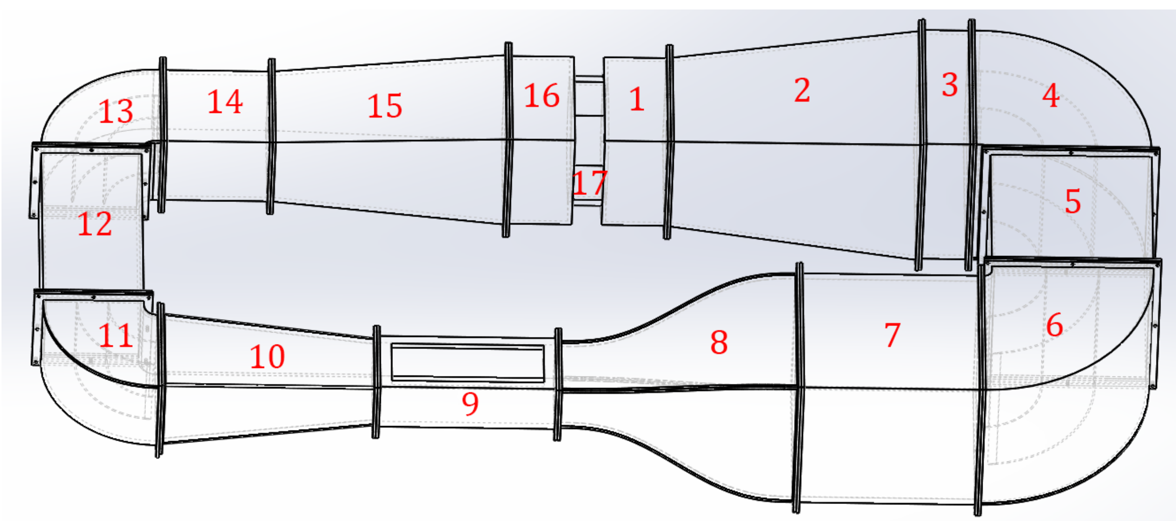

Figure 2-10. The designed wind tunnel. (1,3,5,12,14,16) straight ducts. (2,10,15) small angle diffusers. (4,6,11,13) corners. (7) flow conditioning and settling chamber. (8) contraction zone. (9) test section. (17) axial fan

2.2 PIV data acquisition system

2.2.1 Seeding

The measurement in Particle Image Velocimetry Technique is indirect. Meaning that the motion of the scattered particles in the fluid is investigated and regarded as fluid motion behavior. The selection of seeding particles and how to introduce them to the flow, then, has a direct impact on the results; the results which are to be derived from the consecutive images mostly created by the scattered light from those particles. The details about seeding particles (fluid mechanical properties and their light scattering behavior) is given below.

2.2.1.1 Fluid Mechanical Properties of the Seeding Particles

If we take the particles' shape as spherical and consider them in a viscous fluid with low Reynolds number, using Stokes' drag law we will have the following relation for gravitationally induced velocity, U_g [50]:

$$U_g = {d_p}^2 \frac{(\rho_p - \rho)}{18\mu} g \tag{2-8}$$

Where ρ and ρ_p are the densities of the fluid and the particles, respectively, and d_p is the diameter of the particles. Also, the dynamic viscosity of the fluid and gravitational acceleration are shown as μ and g, respectively. Equation 2.9 shows that if the densities of particles and fluid are the same, the velocity induced by gravity (which could be a considerable cause of error) for the particles would be zero. Practically, this is not the case with seeding particles in air. One can lower U_g by choosing small particles as it affects the order of magnitude of U_g significantly, see Equation (2-8).

2.2.1.2 Light Scattering Behavior of the seeding particles

Factors affecting the light scattering of seeding particles are mainly:

1. The refractive index of the particles to that of the surrounding medium
2. Particles' size, and their shape
3. Observation angle

For spherical particles with diameters larger than the wavelength of the laser -which is $532\ nm$ in this study- ($d_p > \lambda$) Mie's scattering theory can be applied [48]. As the particle becomes larger, the intensity of scattering light is magnified, making the larger particles better for light scattering behavior. This added to the fact that smaller particles are better for following the flow makes the selection of particles size to become a compromise. However, there are ways to keep the size of particles still rather small. For one reason, the scattering intensity of light in air is favorable (at least on order better compared to seeding particles in water-based PIV applications). This is because the refractive index of water is considerably larger than that of air. Plus, when light hits the particle, it scatters in every direction. The light sheet hitting lots of particles, creates a massive multi-scattering. The multi-scattering of the light makes the particles to not only scatter the source light in the desired direction but also scatter the lights that they receive from other particles. Hence, not only the size of the particles helps the light to be scattered desirably but also the number density of the particles, when increased, reflects an amplified light towards the camera.

2.2.1.3 *Seeding of air flow in application*

There are powder-seeding of airflows which are not common due to many reasons e.g., failure in mixing properly with the air flow. The most common application for air flow seeding is use of Laskin atomizers and vegetable oil [51]. Vegetable oils are considered less unhealthy (for the operator) than other particles. The size of the particles can vary depending on the choice of the oil and nozzle pressure, but mostly, are in the range of 1 μm. They are also desirable for small scale turbulence measurement due to their good tracking ability and high stability. On the other hand, theatrical fog is of higher concentration than the particles made by Laskin atomizers, and it has favorable uniformity which makes it a good choice for seeding the air flow. The particles made by Laskin nozzles using vegetable oils are smaller. Choosing between these two is a trade-off between the quality and the concentration of particles. For this experiment a theatrical fog generator was chosen, because they are considerably cheaper than using Laskin atomizers. The particle size using the fog generator is less than 5 μm following the flow well and showing a noticeable light scattering behavior.

2.2.2 Illumination

The laser system used was a double oscillator Q-switched Nd:YAG (1064 nm) with a harmonic generator to convert infrared to visible light ($1064\ nm$ to $532\ nm$) [52]. The laser used has two independent oscillators to generate two successive pulses at 1 ns. The two laser beams created by independent oscillators are combined in a polarizer. Laser head, which is the most important part of the laser system, is connected to power supply unit which comprises the control, power and cooling units. Finally, a remote control is connected to the power supply unit to gain control over the use of lasers and energy output remotely. There are three operation modes for timing of flash-lamp and Q-switch can be controlled:

1. Fully internal mode: In this mode the timing of the flash-lamp and Q-switch is controlled using the timing set by the factory which is mostly the case for fault detection.
2. External lamp mode: The timing of the lamp can be controlled externally, and Q-switch delay is controlled by factory time set.
3. Fully external mode: In this mode both the flash-lamp and Q-switch are set to be controlled externally. When Davis software is used to control the timing of pulses, this mode is used.

To convert the beam emitted from laser head, “Light Sheet Optics” from Lavision is used. It is basically comprised of two spherical lenses placed in a housing which can be coupled to a cylindrical lens to create a thin light sheet for the experiment. The two spherical lenses are used to control the thickness of the light sheet while the aperture and the height of the light sheet is solely controlled by the focal length of the divergence (cylindrical) lens and the beam diameter. The light sheet thickness set for the current study was 0.5 mm (which covers 9.7-18.8 percent of the drop width for different cases of study). Plus, the distance between the spherical lenses can be changed by turning the frame of the housing and thus, the thickness of the light sheet is changed.

The dimensions of the light sheet can be adjusted by refocusing the light-sheet thickness as well as by interchanging different divergent lenses. The height of the light sheet is mainly determined by the focal length of the cylindrical lens. The associated calculations are given in section A.2A.2.

The laser used for the current application is a NANO S 30-30 PIV laser from Litron Lasers shown in Figure 2-11.

a

B

Figure 2-11. a) Laser Head b) Power Supply Unit (the pictures are used with permission from Litron Lasers)

2.2.3 Image Acquisition

The main objective in manipulating various apparatus in a certain PIV experimental setup is to take high contrast clear consecutive images of seeding particle distribution in the flow. The images are taken for further image processing and extraction of desired results (mainly velocity vector field of the associated fluid flow). Thus, it wouldn't be an exaggeration to claim that all those considerations in the setup would be worthless if the image acquisition system fail to provide high resolution images with desirable frame rate and high signal to noise ratio namely.

The camera used for the setup is "Imager sCMOS" camera from LAVISION that offers an inter-framing time of $120\ ns$ in full resolution which is $2560 \times 2160\ pixels$ with each pixel being of the size $6.5\ \mu m\ \times 6.5\ \mu m$. This camera is associated with a CameraLink interface which connects the camera to the "Silicon software microEnable IV frame grabber" as a part of the computer. The camera works in “Global shutter” mode which means the exposure time is identical and simultaneous for all pixels making it suitable for flashlight-illuminated images. The specifications for the camera are brought in section B.4.

2.2.3.1 Lens Selection

Razzaghi et al. [36] studied shedding of multiple sessile droplets which is the closest available study to the work in this thesis. Considering the velocity contours for a pair of droplets and a single droplet in [36], the Field of View (FOV) for this study, was chosen as 25 mm wide rectangle for which the height is governed by resolution of the camera’s sensor (see Figure 2-12).

a

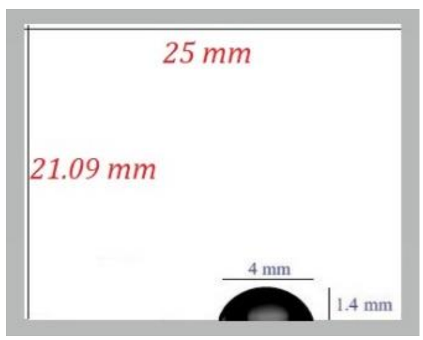

Figure 2-12. a) Field of View

As the field of view is considerably small, a lens with rather large focal length was required while the minimum focus distance is not significantly large. A C-mount lens “180mm F/3.5 Di SP MACRO 1:1 Lens” from TAMRON was selected. The minimum working distance of the lends is 47 cm at which -considering the FOV and the Sensor Size- a focal length of 187.5 is obtained (fairly close to 180 mm (the focal length of the lens)). The Calculations on selecting the proper lens and the specification of the chosen lens are given in section A.3 and section B.5 respectively.

2.3 The Setup

The Experimental setup designed in thesis is shown in Figure 2-13 and Figure 2-14.

Figure 2-13. The experimental setup made for PIV study on the air flow over droplets

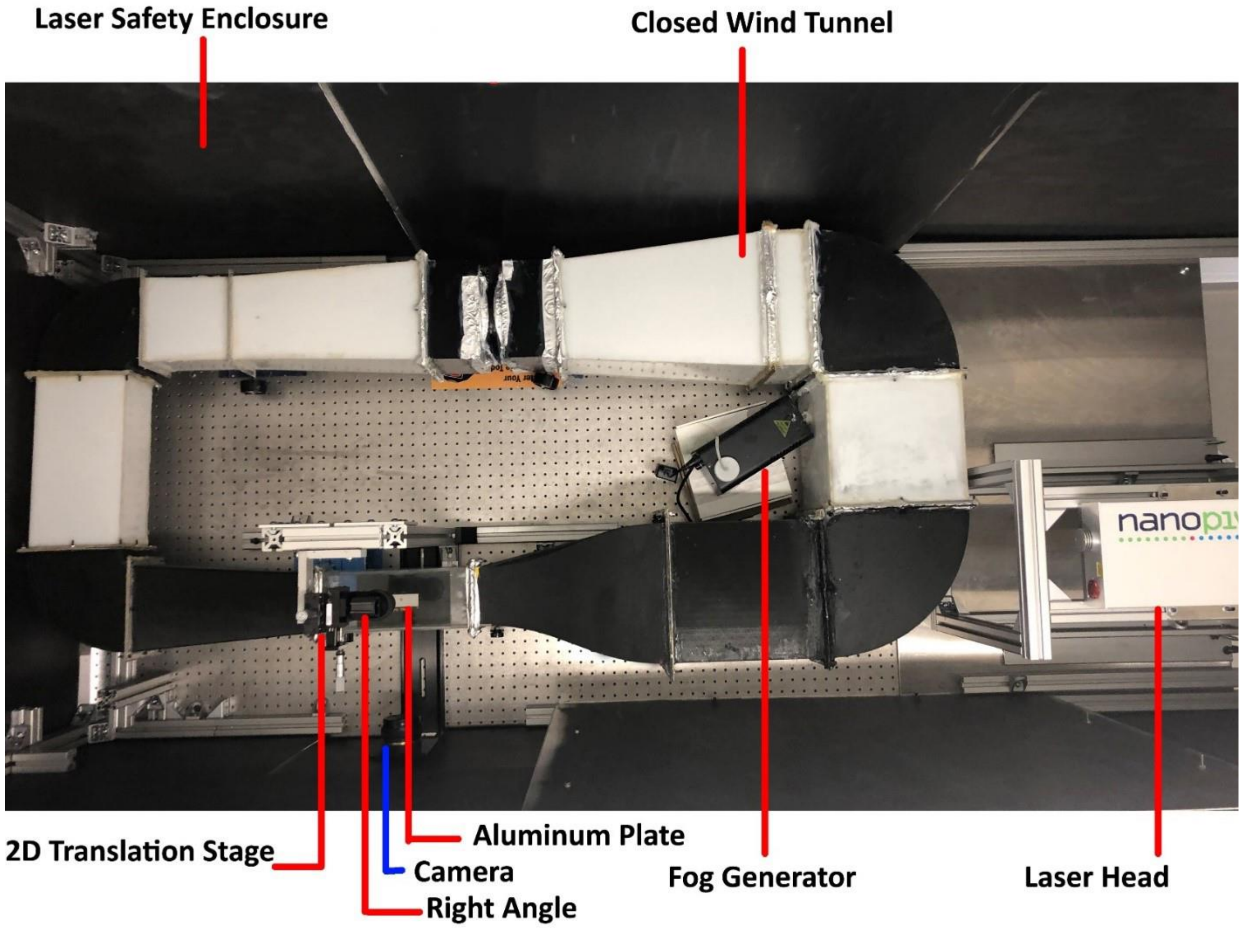

Figure 2-14. The experimental setup made for PIV study on the air flow over droplets (top view)

3 Methods and Materials

To conduct the experiments in this thesis, the following were considered:

1. Surface preparation
2. Particle image acquisition procedure
3. Processing and Post-processing of double-frame particle images to obtain the velocity fields
4. Checking the convergence of turbulence for successive velocity fields for time averaged results
5. Checking the evaporation of droplets in successive double frame imaging (limiting the number of instantaneous velocity fields due to evaporation of droplets)

Before getting to the details on how the tests are carried out, the statement of the problem is put forward to inform about the conditions of the designed experiments.

In the current study, the effect of surface wettability and drop size on the air flow characteristics are to be investigated. As such, four different surfaces (Teflon, PS, PEMA, and PMMA) were used (see Table 3-1). The contact angles were calculated using the PIV images (in ImageJ) which were done at the verge of shedding for droplets. The drop sizes varied from $10\ \mu l$ to $30\ \mu l$ (see Table 3-2). The droplet heights were measured using the PIV images in ImageJ. The air velocities were set just below the critical air velocity that onsets the incipient motion of the droplets (see Table 3-3). The velocity values were found using separate experiments (shadow-graphies) with the same conditions using the wind tunnel. The local Reynolds numbers ranged from 3×10^4 to 7.2×10^4. To calculate the local Reynolds numbers, the free stream velocity and the distance from the leading edge of the deck were used.

Table 3-1. Receding and advancing contact angle values for different surfaces

	Receding CA $\pm$ 2°	**Advancing CA $\pm$ 2°**
Teflon	104°	108°
PS	74°	91°
PEMA	62°	76°
PMMA	56°	70°

Table 3-2. Droplet heights

Height ± 0.05 ***(mm)***	$10\ \mu l$	$20\ \mu l$	$30\ \mu l$
Teflon	1.6	2.2	2.5
PS	1.2	1.8	2.0
PEMA	1.2	1.6	1.8
PMMA	1.0	1.4	1.7

Table 3-3. Free stream air velocities

Free Stream Velocity ± 0.05 ***(m/s)***	$10\ \mu l$	$20\ \mu l$	$30\ \mu l$
Teflon	5.6	4.8	4.5
PS	8.5	8.2	6.6
PEMA	8.9	8.3	8.1
PMMA	10.8	9.9	8.4

Table 3-4. Reynolds numbers based on droplet heights

$Re_h \pm 5$	$10\ \mu l$	$20\ \mu l$	$30\ \mu l$
Teflon	620	730	780
PS	730	1000	910
PEMA	730	900	990
PMMA	740	950	970

3.1 Surface preparation

Aluminum substrates with the thickness of 7 mm were used for all the coatings. This way, it is made sure that the roughness of the substrates does not vary significantly. To prepare the mentioned surfaces, solutions were made, and spin coated on the substrates. The following solutions were made for each coating:

Teflon: Teflon AF (DuPont Teflon AF 601s2-100-6) diluted with FC-75 (3M) in the ratio of 1:5

PS: 1wt% solution of Polystyrene (Aldrich Mw~35,000) in toluene

PEMA: 1wt% solution of Poly (ethyl methacrylate), (Aldrich Mw~515,000) in toluene

PMMA: 1wt% of PMMA (Aldrich Mw~120000) in toluene

The spin coater was set on 1100 rpm and kept spinning for 3 minutes for each substrate to coat the substrates.

3.2 Solid Droplet Mockups

To analyze the effect of drop oscillations, the sessile droplets were modeled in solid works. Figure 3-1 shows the models of a sessile droplet at the verge of shedding on a substrate. The models were then 3D-printed with a quite precise printer (Objet260 Connex3) (see section B.2 for specifications). The precision is high enough (16 microns) to imitate the topology of the droplets at that scale, but, the roughness of the modeled droplets is not as smooth as the surface of a sessile droplet is. With the modeled droplets imitating the topology of the droplets and being rigid, the differences should indicate how crucial the drop oscillations could be for the air flow over the droplets in the current study.

a)

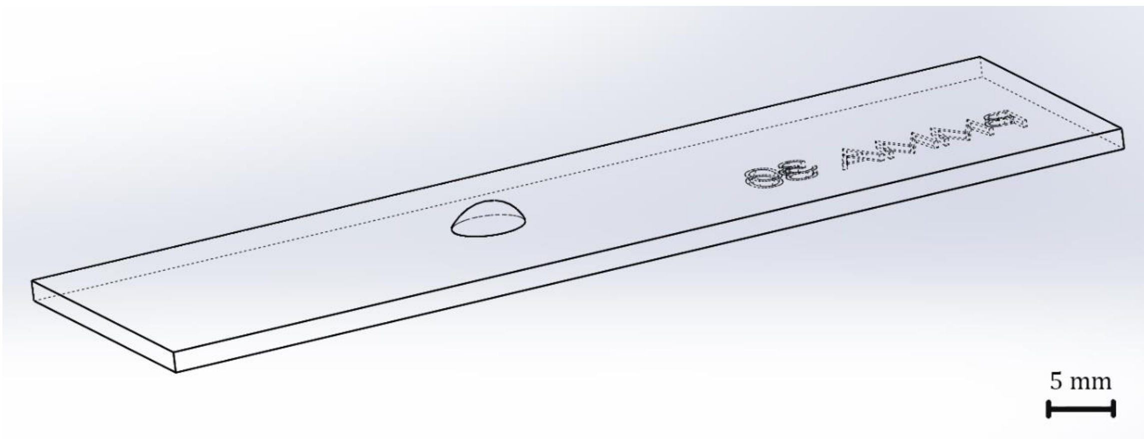

b)

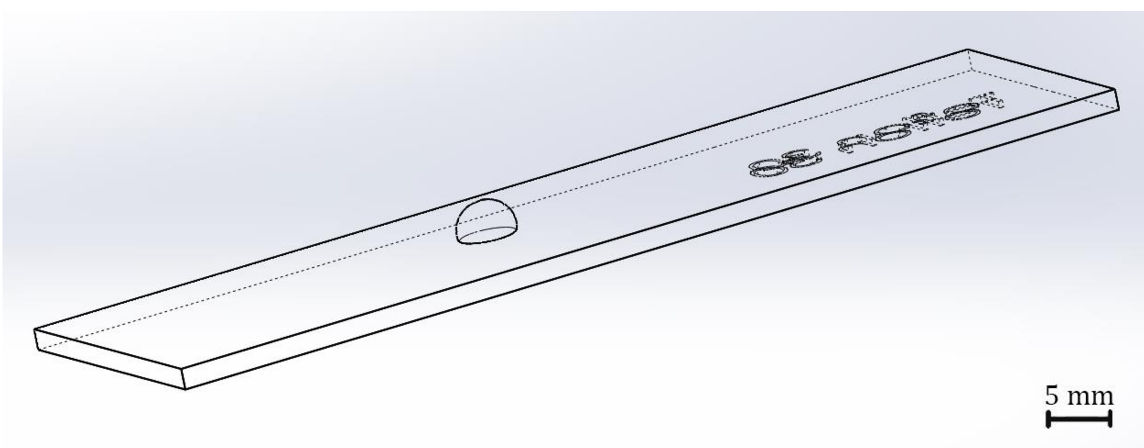

Figure 3-1. The designed models of a sessile droplet on a substrate at the verge of shedding. a) a droplet placed on PMMA. b) a droplet placed on Teflon

3.3 Particle image acquisition procedure

Particle Image Velocimetry is a technique used to obtain instantaneous velocity measurements. The air is seeded with tracer particles which, for sufficiently small particles, the movement of the particles represent the air flow. The air with entrained particles is illuminated so that particles are visible. The motion of the seeding particles is used to calculate speed and direction (the velocity field) of the flow being studied.

The steps to capture particle images in this study is as follows:

- First, the coated aluminum substrates were placed inside the slot that was designed on the deck (which is set in the middle of the test section)
- Then, all the equipment needed for the test are switched on (the laser is only ready to shoot and does not emit any beams unless given the command by DaVis). The fog generator needs $\sim$5 minutes to warm up (to be able to inject fog in the system) after being turned on. The scaling is done earlier. This is all important to be done before placing the droplet on the substrate as the evaporation is to be kept at the minimum level possible. The second power supply which provides the signal (to change the velocity of air flow) is to be turned on but kept at a low voltage (1 volt) that does not run the axial fan in the wind tunnel.
- Deionized water was used for sessile droplets. A micropipette with a precision of 0.01 μl was used to place a sessile droplet (with the sizes of 10, 20, and 30 μl) on the substrate.
- The test section cap is placed, the fog is injected through the wind tunnel, and the signal power supply starts the fan and reaches the required velocity with a ramp-up of about

$2.8\ \frac{m/_s}{min}$ in average done manually. The two lasers are fired, and the camera starts recording the double frame images.

The settings for the laser power, timing and recording are set before which was:

- The "Nano S 30-30 PIV" Laser is equipped with a physical external controller. Using the controller and the software, the power of both lasers and the frequency of the shooting could be set. The frequency of laser beam emission is set to 25 Hz, limited by the camera frame rate in its full resolution mode. This means that the two lasers shoot 25 times a second, shooting 50 beams in a second. The two laser beams are Δt (inter-framing time) apart from each other. To optimize the cross correlations, the interframe timing were optimized considering a 5-pixel displacement for the particles. In practice, however, the interframe timing was set higher than the time suggested by the optimizations calculated based on the free stream velocity. Because the optimizations are based on free stream velocity, while the wake area has a lower velocity and is even more important than the free stream velocity.
- The camera was set to full resolution (2560×2160) and the double frame mode was selected in DaVis, with T_A and T_B where $T_B - T_A = \Delta t$. The frequency of the recording was set to 25 Hz (maximum). A f-number of 3.5 was chosen to give the lowest depth of field which for the current setup is 0.3 mm. Then it was made certain that the camera was capturing the particles movement in the mid-plane of the sessile droplet. The numbers of double-frame particle image set to record depends on the evaporation of the droplet and convergence criteria (see below). Depending on the drop size, the number

of double frame image sets vary, e.g., 500 double frame image sets for 30 μl droplets, 400 sets for 20 μl droplets, and 300 sets for 10 μl droplets were used.

3.4 Processing and Post-processing of particle image sets

The images should be cross correlated to obtain the displacement of particles. Given that the time difference between each two frames in a double frame image set is equal to Δt, the velocity of particles was found using ${displacement}/_{\Delta t}$. The processing of the particle images could include image preprocessing and a post processing for the velocity field. The preprocessing and postprocessing, however, are not necessarily required for all particle images. If the particle images are clear and sharp, and there is no part in the image sets to be masked out, then they might not be preprocessed. Again, in an ideal case, with the particle images being perfectly sharp and clear, the concentration and distribution of the particle being favorable, and the processing options being chosen wisely for the associated particle images, the calculated velocity field might not need go through post-processing steps. The image pre-processing, processing and post-processing procedures applied to the particle image sets of the current experiments are provided herewith.

3.4.1 Image preprocessing

The process basically involves any image alternations before they go through the cross-correlation algorithms. The alterations do not change the state of the particles in the images indeed, and (if done correctly) only make them more recognizable by the cross-correlation algorithms.

The following filters were applied to the raw particle images:

- Subtract sliding background: In double frame PIV recordings, the exposure time of the second frame is always longer than the first frame (see Figure 3-2). This makes the background of the two frames different in a double frame image set (the second frame is brighter). To minimize the exposure difference between the background of the two frames in a set, the "Subtract sliding background" option in DaVis was used. This is a high-pass filter to filter out the local mean background intensity leaving only the local fluctuations. The filter was applied with a scale of 10 pixels.

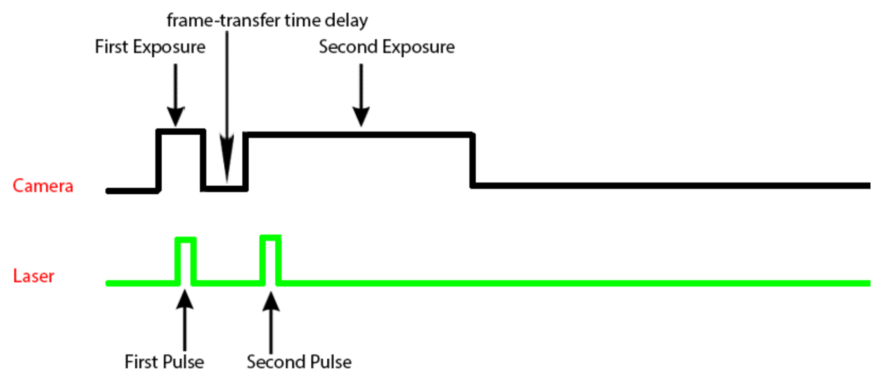

Figure 3-2. Camera exposures and timing of the illumination pulses for dual-frame recording

- Particle intensity normalization: which identifies the min/max intensities in the image and normalizes the min/max values. The min/max filter was used with a scale of 7 pixels. The effect of both "subtract sliding background" and "particle intensity normalization" is shown in Figure 3-3.

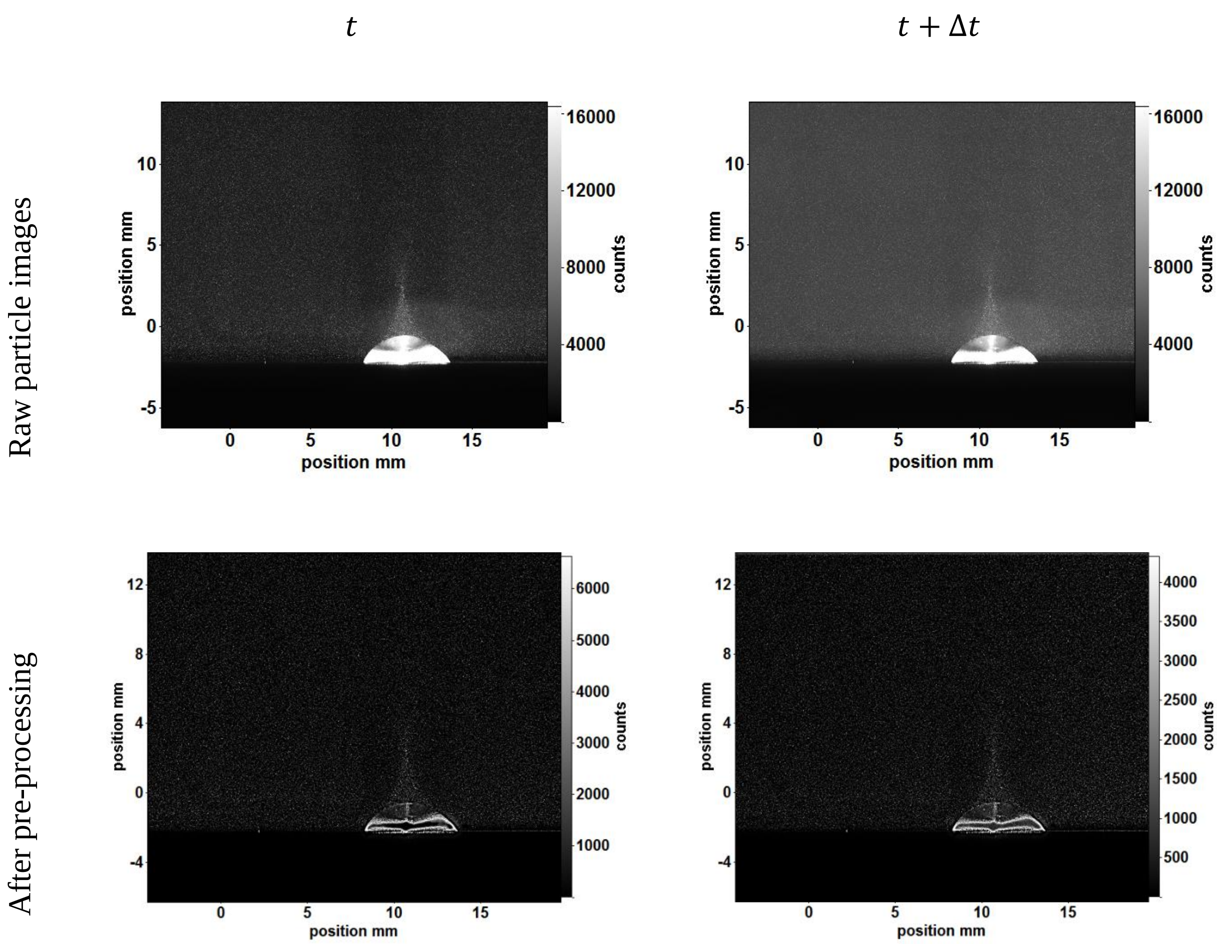

Figure 3-3. sample double-frame particle images before and after pre-processing (subtract sliding background + particle intensity normalization)

- Masking: In PIV recordings, it is mostly the case that only a part of the image contains the particles which displacements are of interest. The other regions (which are mostly black, not reflecting the light, or white, showing high reflections) would only give erroneous vectors during the cross-correlation process. This would require a high computing capability, longer computing time, and more importantly the vectors in those areas are physically meaningless. As such, images were masked. Geometric masks were used to only enable the region where the air flows (showing particles). Figure 3-4 shows a masked particle image.

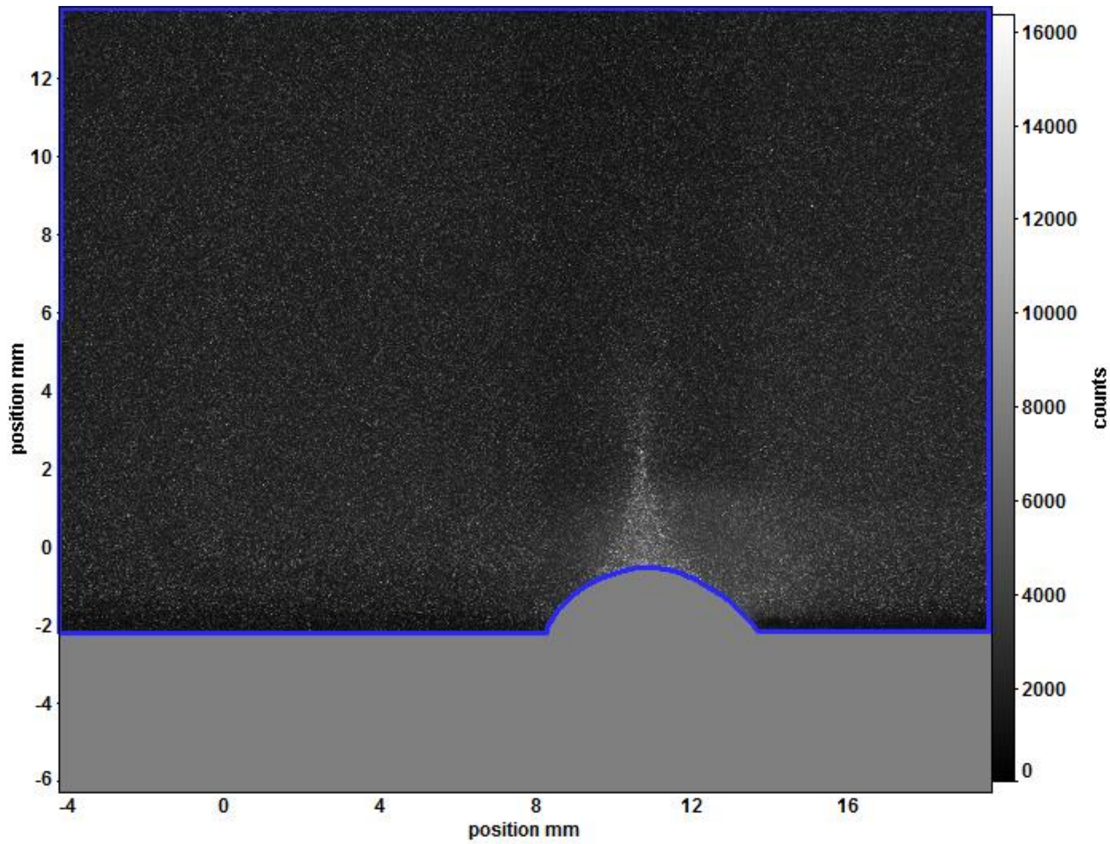

Figure 3-4. A sample of a geometric mask used to enable only the fluid flow (particle displacement) part of the frame to undergo cross-correlation computing

3.4.2 Image processing

To obtain a vector field, each frame is divided into interrogation windows. The standard cross-correlation PIV algorithm integrated in DaVis computes the 2D cross-correlation plane from the correlation of the two input image interrogation windows. The cross-correlation is done using the light intensities of two $N * N$ pixel interrogation windows -e.g. $32 * 32$ pixel- from the light exposure at the two frames in a set (which are e.g. 8 μs apart). The computation of the correlation is done using FFT, rather than adding up the correlation values directly.

In the correlation plane of size N $*$ N pixel at image position (x_0, y_0):

$$C(x_0, y_0) = I_1(t_1, x_0, y_0) \otimes I_2(t_2, x_0, y_0) \tag{10}$$

Finding the highest correlation peak, the displacement of the particles ($D(x_0, y_0)$) in that interrogation window from the first frame to the second frame is:

$$D(x_0, y_0) = position\ of\ highest\ peak\ in\ C(x_0, y_0) \tag{11}$$

Using the $D(x_0, y_0)$ and the interframe time delay (Δt), the velocity of the particles (or basically the fluid) is found at the location:

$$V(x_0, y_0) = {D(x_0, y_0)}/{\Delta t} \tag{12}$$

Having calculated the correlation planes for all interrogation windows, the velocity field can be determined. The resolution of the calculated velocity field depends on the size of the interrogation windows chosen. The rule of thumb is that there should be at least 10 particles in an interrogation window to gain high correlation values [49]. So, the size of the interrogation windows selected for a PIV recording, completely depends on the flow and the concentration of the particles in the flow. Other than the mentioned factors in the resultant calculated velocity field, the certainty of the calculations/results highly depend on the recording and whether certain practical measures (listed below) have been taken care of. The mentioned factors are listed below shortly:

1. The particle size and its concentration inside the area of interest
2. Appropriate scaling/calibration of the FOV
3. Adjusting the f-stop and the output power of the laser with respect to each other

4. Adjusting the focus ring exactly on the location of light sheet
5. Adjusting the time interval between two frames based on the velocity of the fluid in the area of interest, camera resolution, and focal length of the lens.

In this thesis, a multi-pass cross correlation was applied to images. In that, a one-pass cross-correlation with interrogation windows of the size $64 * 64$ pixels and a 50% overlap, were used as the first step of computation. Then, two passes of cross-correlation with interrogation windows of the size $32 * 32$ pixels and an overlap of 75% were applied to obtain the velocity field. The application of multi-pass computation has a significant advantage over the single-pass cross-correlation computation. This way, a larger interrogation window is used to calculate the velocities in a lower resolution. The larger interrogation windows usually give higher correlation peaks as the number of particles are higher in such windows [51]. Having found the coarse displacement of the particles, the smaller interrogation windows in the later passes can conformed to the broad displacement of their parent interrogation window in the previous pass. Meaning that, the interrogation window of the second frame in each set is moved according to the calculated displacement of the parent interrogation window. This way, fewer particles are missed in the small interrogation windows and higher correlation peaks are obtained. The standard FFT algorithm was used to calculate the correlation maps for the PIV recordings. Correlation plane is normalized between 0 and 1. A correlation of 0 means there is no match between the two interrogation windows and a completely erroneous vector is the output. A correlation peak of 1 is the identical vector as if every pixel of the interrogation window in the first frame is identical with the interrogation window of the second frame (if the first interrogation window is moved with the resultant displacement vector). Thus, as the correlation peaks increase, the results are more reliable. A correlation peak of 0.7 and more is believed to give a highly reliable vector in the interrogation window [54]. Correlation values less than 0.3 are accounted as to give not quite reliable vector data [54]. The correlation value map for the air flow over a sessile droplet is shown in Figure 3-5. The correlation values in the free stream is around 0.95 which is noticeably high. In the wake area, the values differ, but all are above 0.7.

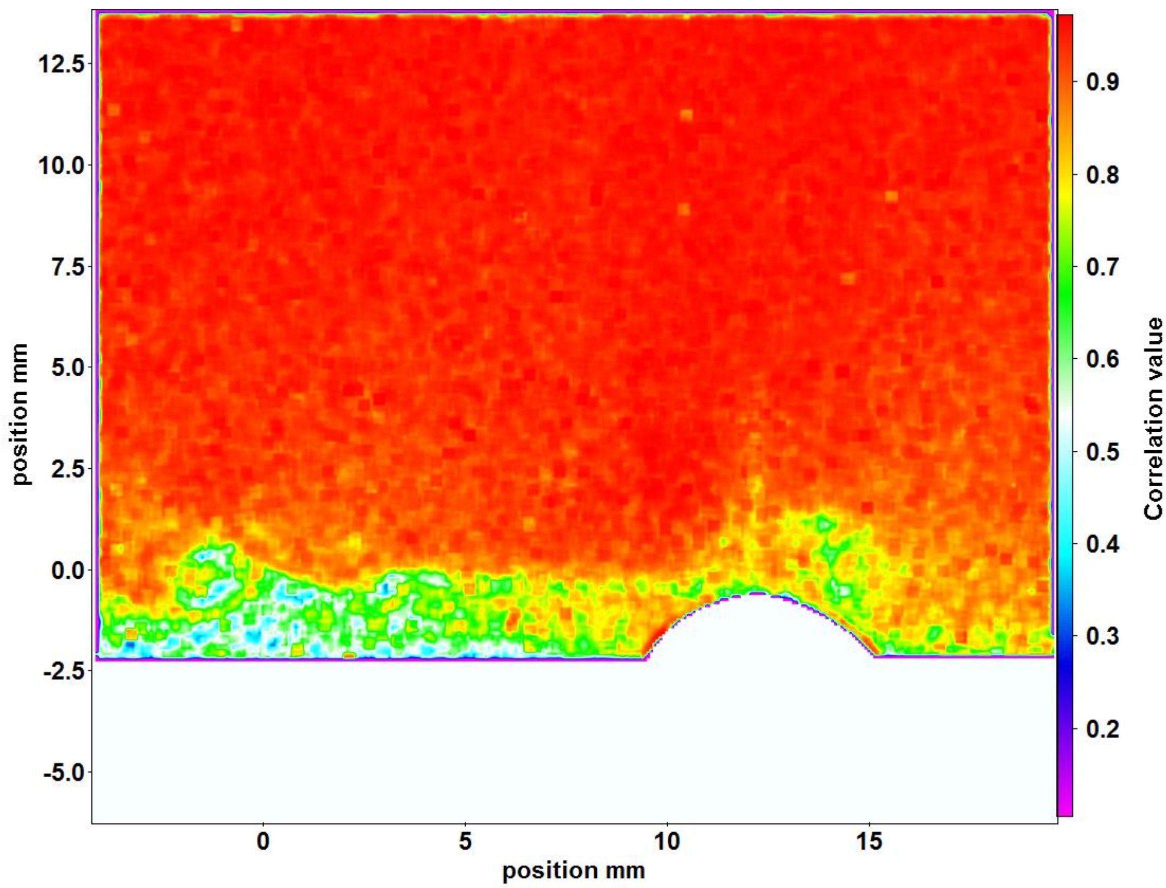

Figure 3-5. Correlation value contour for air flow over a droplet

Aside from the value of the correlation peaks, it matters that the second highest peak is less considerably less than the highest peak. If there are two high peaks which values are close, the displacement of the particles could be either of those. So, it is recommended that the peak ratio (Q) is better to be more than 2. The higher the peak ratio more reliable the results get.

Figure 3-6 shows correlation planes for two random interrogation windows in the free stream and the wake region; the highest peak is considerably higher than the second highest peak in the map. This makes the first (highest) correlation peak a reliable candidate to indicate the displacement of the particles. Figure 3-7 shows the peak ratio contour for air flow over a sessile droplet. Figure 3-7 indicates that most of the field have high peak ratios (more than 90). With the high correlation values shown for these areas and the significantly high peak ratios, the results are reliable. To make sure that the peak ratio across the field is not less than 2, the same correlation map as in Figure 3-7 is brought in Figure 3-8 with a different scaling. Figure 3-8 indicates that the peak ratio is not lower than 2 across the field. Then the correlated values (thus, the velocity fields) are reliable.

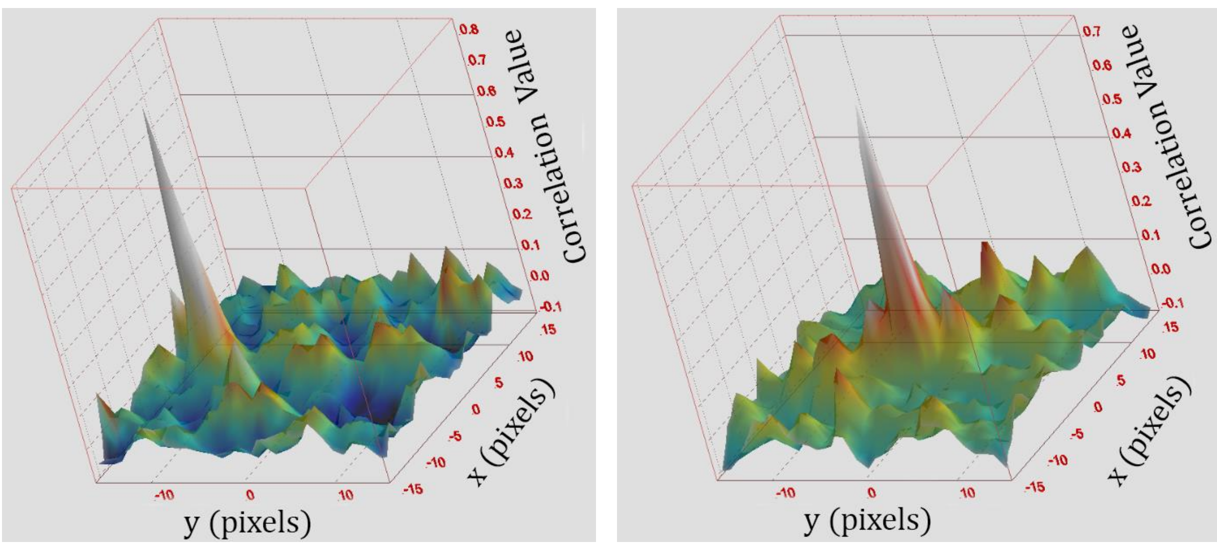

Figure 3-6. the correlation planes for a random interrogation window in: a) free stream b) wake area

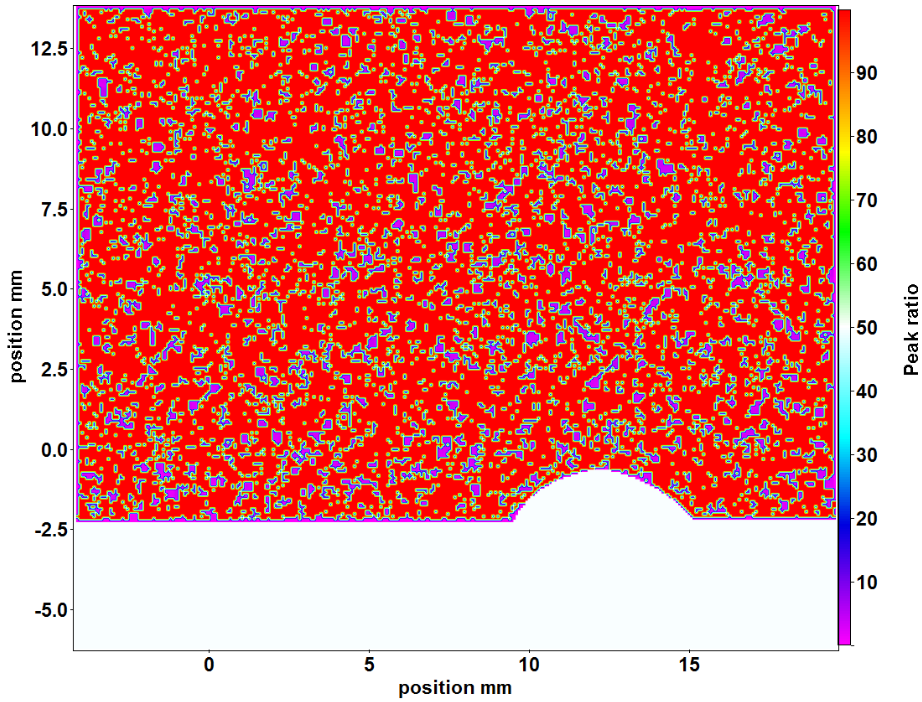

Figure 3-7. Peak ratio contour (a sample) for air flow over a sessile droplet (min-max scale)

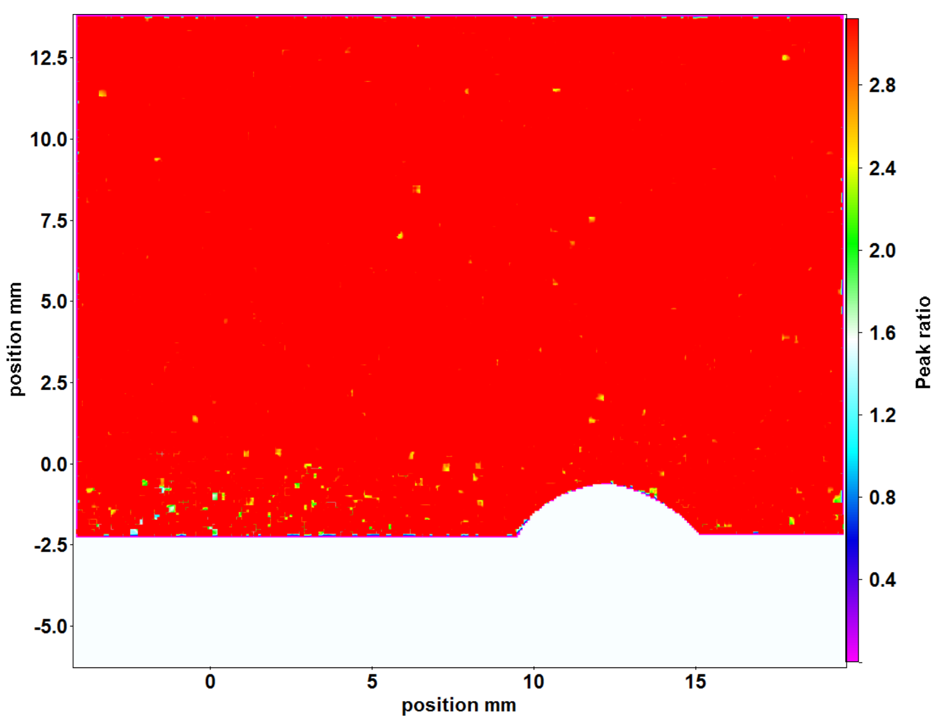

Figure 3-8. Peak ratio contour (a sample) for air flow over a sessile droplet (modified scale)

3.5 Averaging the instantaneous results over time

3.5.1 Checking the convergence of turbulence for successive velocity fields for time averaged results

Given the turbulence caused by the high velocity of the flow and created by the droplet, the instantaneous velocity fields show fluctuations. To take an instantaneous velocity field as the typical flow field for a certain wettability and drop size is rather flawed; as the instantaneous velocity field does not fully represent the flow (the properties change over time). Then, a certain number of instantaneous velocity fields are averaged over time. To define the number of successive velocity fields to average over time, the convergence of turbulence was plotted. To that end, the air flow over droplets placed on PMMA were assessed for all drop volumes. The reason why PMMA was chosen out of all surface wettabilities was due to the high critical air velocities required for droplets on PMMA. And that, the high free stream velocity flows have the potential to give rise to higher turbulence in the field. The convergence plots for air flow over a $30\ \mu l$ droplet on PMMA are given in Figure 3-9. The plots are given for random points in upstream, free stream, and downstream of the flow. After convergence, random spikes are seen which are negligible considering that more images mean more evaporation of the droplet and the least number of images to provide reasonable turbulence convergence are sought.

A

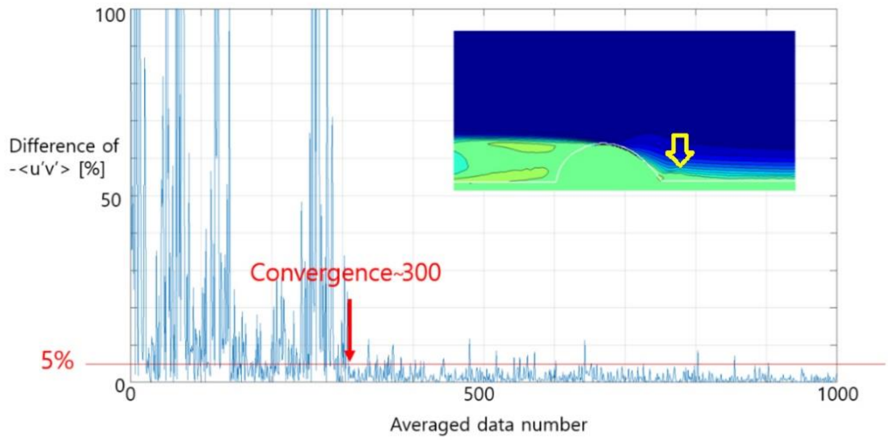

B

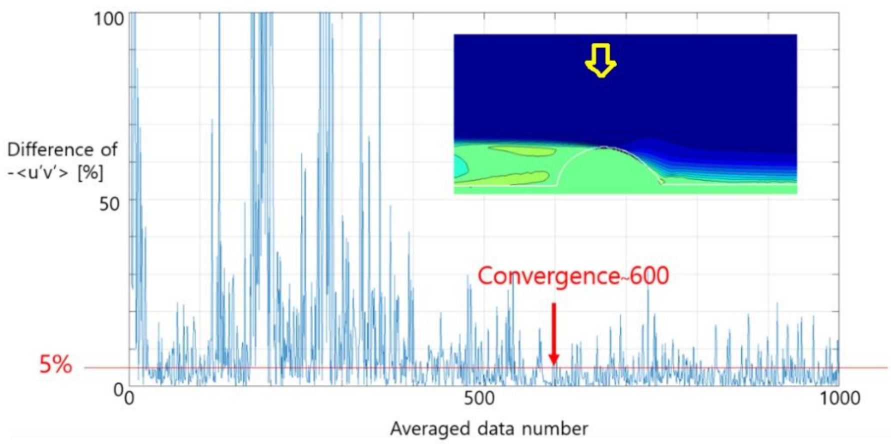

C

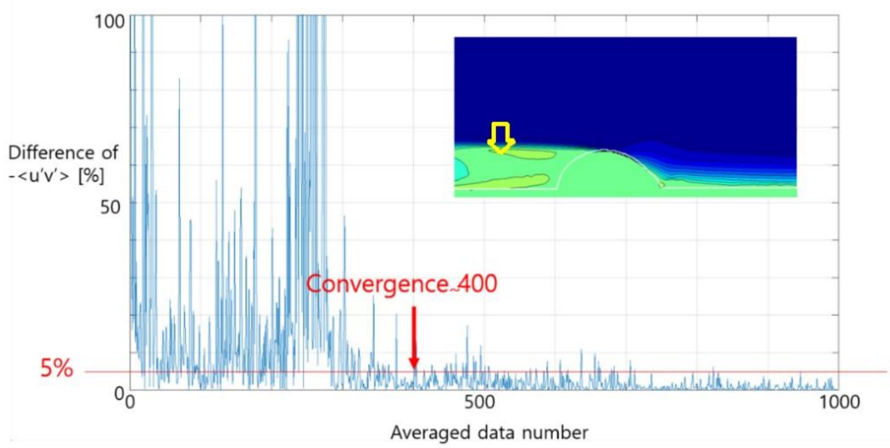

Figure 3-9. Convergence plots for random points for air flow over a 30 μl droplet on PMMA.

a) Upstream b) Free stream c) Downstream

Figure 3-9 indicates that considering a 5% convergence of the Reynolds stress, the following number of instantaneous velocity fields are required: 300 for the upstream of the flow to be converged, 600 for the free stream and 500 for downstream of the flow.

3.5.2 Evaporation of the droplets

The sessile droplets in the study evaporate being exposed to air flow and laser light. As the evaporation makes the sessile droplet, the air flow characteristics is subject to change. To realize the evaporation rate based on the number of successive double-frame images captured in a test, certain studies were done. To that end the profiles of droplets in particles images of air flow over a sessile droplet at the verge of shedding were used. Given the refraction of light by the droplets, the droplet profiles are not uniformly lit up and clear. Then using the image processing tools by any program would fail in binarizing the image such that the droplet profiles stand out. Several image processing algorithms in this case were used in MATLAB and the droplet profiles did not come out well. The particle images containing the droplet profile were exported then, manually modified using Adobe Photoshop, and then binarized using MATLAB. The manual modification using adobe photoshop adds some error to the calculations but is reliable enough to suggest the order of recorded images to maintain most of the droplet during the experiment. This way the reduction of drop area was calculated through time and the volume reduction (evaporation) was approximated using $V = A^{3/2}$.

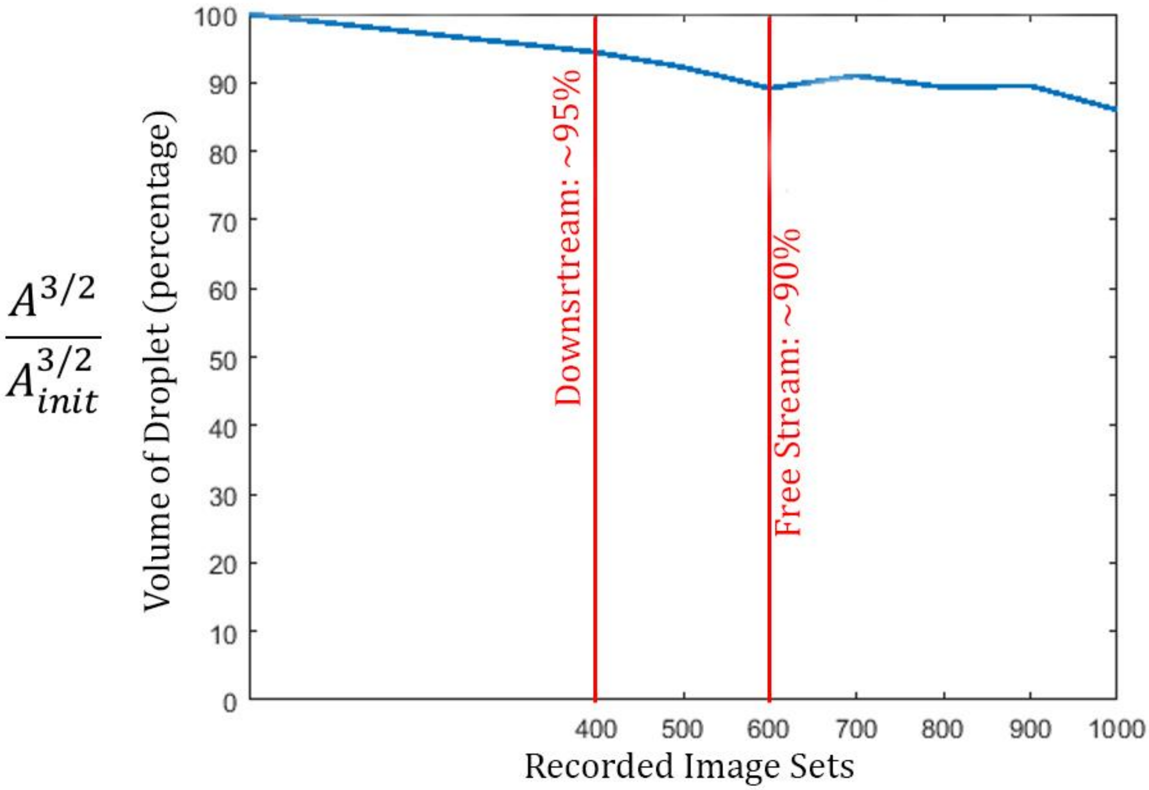

Figure 3-10. Volume of droplet vs recorded image sets for a 30 μl droplet placed on PMMA

Figure 3-10 shows the volume of a 30 μl droplet placed on PMMA through time (Volume of the droplet vs the number of captured double-frame images). The evaporation is increased due to the convective air flow and the Laser light sheets impacting the droplet. As indicated by Figure 3-10, for a 30 μl droplet on PMMA (which is the most critical in evaporation due to high air velocity), ~90% of the droplet volume is preserved with 600 double frame recording in the test condition. As the convergence of Reynolds stress downstream of droplet is most critical and the evaporation of the droplet is to be kept as low as possible, a 500 double frame recording was decided for 30 μl droplets.

The same procedure (to find out the convergence of Reynolds stress for air flow over sessile droplets and the evaporation rate of the droplet vs the captured double-frame images) was followed for 10 μl and 20 μl droplets. Given the convergence and evaporation data on those drop sizes, 400 and 300 double-frame recordings for 20 μl and 10 μl droplets were decided respectively.

3.6 Post-processing the results using MATLAB

The particle images was processed in DaVis to find the velocity fields. The results were exported in "vc7" format. Then, they were imported and read in MATLAB using the "PIVmat" library. Having the velocity and mask files read by MATLAB, the post-secondary data derived by the velocity (e.g., vorticity) were calculated. Accordingly, the time-averaged results were calculated.

The new mask and data files processed with MATLAB were exported as a DAT file. The DAT files were used in Tecplot to showcase the required results.

3.7 Sources of Error

The possible sources of error for the current experiments are listed below:

- Scaling: Depending on the resolution of the ruler used in the experiment (The printed scales on the ruler), the conversion of pixel to mm could be off a few pixels from reality (which is certainly kept at lowest using the zoom options and doing the scaling as precise as possible). In practice, a quite thin steel ruler was put in the field of view normal to the camera sensor. Then a sharp image of the ruler in the FOV is taken. Using the scaling option in DaVis software, the longest two marked positions on the ruler are chosen (to have the lowest conversion error). Given the horizontal number of pixels between those two points and the physical distance in mm, the scale factor is calculated. The scale factor for the experiments was 107 pixel/mm.

- Laser light sheet position relative to the droplet: Due to the scale of the laser light sheet ($\sim 0.5\ mm$) and the droplet, positioning the droplet such that the laser light sheet bisects the droplet exactly in mid-plane is not a trivial task. In that, quite precise measures were taken to avoid any possible misalignment. Due to manual positioning of droplets, the laser light sheet may not cross the mid-plane of droplets. Estimated misalignment was less than 0.1 mm.
- The depth of field: the depth of field was kept quite low such that the particles moving in the mid-plane were captured. The depth of field for the recordings in this study was 0.3 mm.
- Low quality particle images: Various reasons could lead to the particle images not being as sharp, clear and desirable (in terms of cross correlation process). A few important factors are listed below, which if not managed properly, would lead to considerably high errors in the results:
    - The size (∼5 micron), density ($\rho \sim 1\ kg/m3$), and concentration of the particles.
    - Adjusting the f-stop (3.5) and the output power of the laser (40% of the max output) with respect to each other.
    - Adjusting the focus ring exactly on the location of light sheet.
    - Lighting power/energy (40% of the maximum power).
    - Adjusting the time interval between two frames based on the particle displacement, Camera Resolution, and focal length of the lens ($6 - 10\ \mu s$).
- Evaporation of droplets: The evaporation of the droplet makes the droplet smaller. Thus, the air dynamics are subject to change as the droplet shape is changing (getting smaller).

In this thesis, it is made sure that only less than 10% of the droplet is evaporated through the recordings so that the errors are kept as low as possible.

4 Results and Discussion

The results of the air flow over sessile droplets are presented in this chapter. The results are advanced such that the objectives are the thesis are addressed successively. As air flows over bodies turbulence intensity of the flow increases. Instantaneous flow characteristics, velocity, pressure, etc. can be as important as the time averaged values. The reason is that the shedding (or depinning) of the droplet happens at a certain instant. For instance, the average drag coefficient might be such that it does not cause the incipient motion, while the turbulence can be so high at an instance to dislodge the droplet. So, the problem is analyzed in two ways: the time-averaged flow characteristics, and turbulence intensity (to gain insight on how the instantaneous values on the characteristics of flow could vary from the averaged values).

For each objective stated in chapter 1, the results are first presented for one case ($30\ \mu l$ droplets on PMMA coated surfaces) and fully analyzed/explained. Then, the same results for other cases (with different surface wettabilities and drop sizes) are put forward only to analyze the similarities/differences for all the cases.

As such, the results are given to comprehensively understand:

1. The effect of wettability on the air flow structure over a sessile droplet (through:)
   - Normalized x-velocity ($\bar{u}/U_\infty$) contour with streamlines
   - Normalized x-velocity profiles throughout the field
   - Normalized y-velocity ($\bar{v}/U_\infty$) contour
   - Vorticity contour
   - Recirculation length

2. The effect of drop size on the air flow structure over a sessile droplet
3. The effect of drop oscillations on the air flow structure
4. The effect of surface wettability on pressure coefficient
5. The effect of drop size on pressure coefficient
6. The effect of wettability on turbulence statistics
7. The effect of drop size on turbulence statistics
8. The effect of drop oscillations on turbulence statistics

4.1 The effect of wettability on air flow structure over a sessile droplet

To analyze the effect of wettability on air flow structure over a sessile droplet, the following results are presented and analyzed herewith:

1) Normalized x-velocity ($\bar{u}/U_{\infty}$) contour with streamlines
2) Normalized x-velocity profiles throughout the field
3) Normalized y-velocity ($\bar{v}/U_{\infty}$) contour
4) Vorticity contour
5) Recirculation length

All results in the following section are for midplane (in the direction of the airflow) of the droplets. The velocities are normalized with Free stream velocity (U_{∞}). The dimensions are normalized with the height of the droplet (h) in the associated experiment. The recirculation length is found using the velocity contour.

4.1.1 Normalized x-velocity contour with streamlines (PMMA - $30\ \mu l$)

The x-velocity contour (velocity magnitude in the direction of free stream flow, u) and the streamlines are certainly two of the most important visualization tools for flow structure over a body. The x-velocity contour informs us e.g., about boundary layer thickness, the shape and the size of low velocity (wake) region, and flow separation. The streamlines show the direction of the flow as they are tangent to the velocity vector at a certain point and time. Figure 4-1 shows the normalized x-velocity contour along with the streamlines for air flow over a sessile droplet (a $30\ \mu l$ droplet sitting on a PMMA coated aluminum surface).

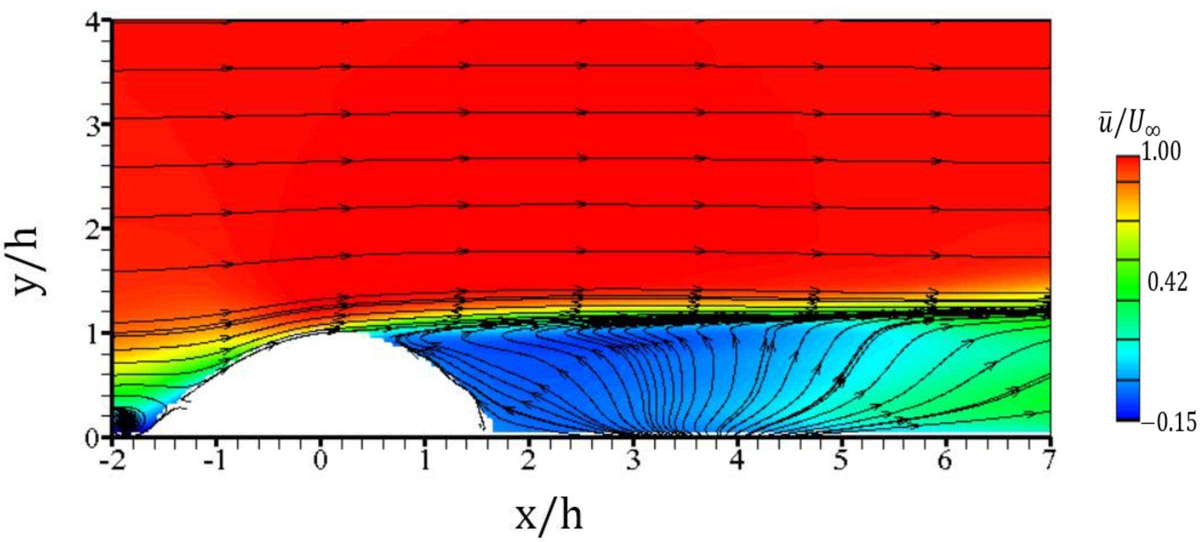

Figure 4-1. normalized x-velocity ($\bar{u}/U_\infty$ shows the x-velocity of each point in the field divided by free stream velocity, U_∞) contour with streamlines for flow over a sessile droplet (PMMA - $30\ \mu l$) (The center of the droplet contact line is located at "0" on the x/h_d axis), $U_\infty = 8.4\ m/s$

Upstream of the droplet in Figure 4-1, a vortex behind the droplet is created. The air coming at higher altitudes (approximately higher than half of the droplet height) follows the surface of the droplet until a flow separation happens. On the downstream of the droplet, there is a recirculation area with a characteristic immediate negative velocity (blue area) (until ${x}/{h} \approx 4$). In the recirculation zone, the air emerges from a source close to the wall. This pattern of air emerging from a "source" over the surface in the midplane is because the two symmetrical large vortices made from the periphery of the droplet is entrained in the mid-plane [36] (see Figure 4-2). This gives rise to a pattern in which the fluid seems to be emerging from a source at some point close to the wall in the wake area. The air that makes the recirculation length join the shear layer while going up, reattaches the main flow at an elevation slightly higher than the drop height. The fluid in the wake area reattaches the main flow at an elevation slightly higher than the droplet height along the way. That is where a high vorticity is expected, due to the direction of the flow changing immediately at the location. The shear layer could be seen more clearly using the vorticity contours shown in section 4.1.5.

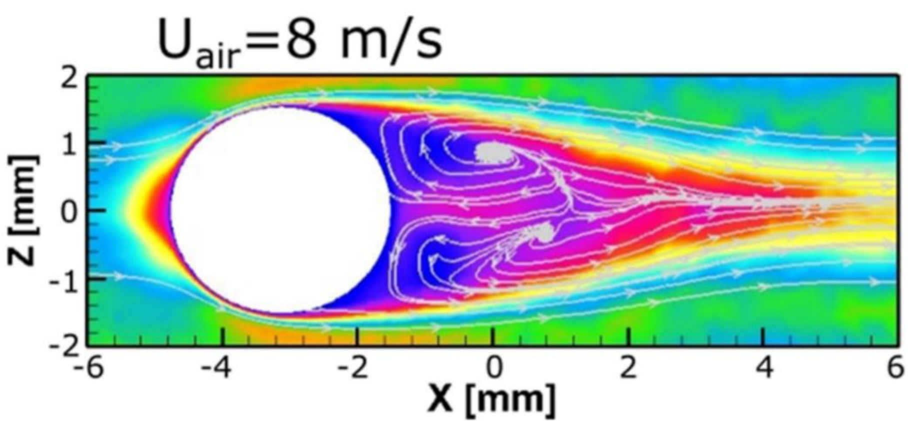

Figure 4-2. the pattern of air flow over a simulated sessile droplet at $0.5h_D$ (top view) [36] (with permission from the author)

4.1.2 Normalized x-velocity profiles throughout the field (PMMA - $30\ \mu l$)

The normalized x-velocity profiles for air flow over a sessile droplet is shown in Figure 4-3. The profiles are shown for three different tests done for the same conditions. The center of the droplet contact line is located at “0” on the x/h_d axis. The grid distances represent the value of “1” in terms of the normalized velocity. Meaning that, for instance, if the normalized velocity profile at some elevation reaches the next grid line, the velocity at that location is equal to the free stream velocity. The other values plotted in between (shown as velocity profiles) show a velocity value which is a ratio of the free stream velocity by scale. The profiles are shown in three different plots for upstream of the droplet, over the droplet, and downstream of the droplet. In the upstream and over the droplet plots, the spacings are equally set to 0.2 x/h_d. The plot showing the x-velocity profiles for the downstream of the droplet, illustrates the profiles in equal spacings of 1 x/h_d.

Velocity profiles in Figure 4-3, shows that the tests are repeatable hence promising in that sense. Figure 4-3a shows the normalized x-velocity profiles upstream of the droplet. The boundary layer upstream of the droplet is laminar ($Re = 5.3\ \times 10^4$ where $x/h = -2.6$). The boundary layer conforms to Blasius approximation of laminar boundary layers. For instance, the thickness of the boundary layer 9.5 cm away from the leading edge ($x/h = -2.6$) based on Blasius approximation is 2.04 mm. Figure 4-3a shows that at that location ($x/h = -2.6$) the velocity reaches $0.99U_\infty$, at $\sim 1.2\, y/h$ which notably conforms to Blasius approximation. Getting close to the droplet, a back flow close to the wall is seen. This corresponds to the vortex created upstream of the droplet.

Figure 4-3b shows the normalized x-velocity profiles over the sessile droplet. The profiles show a zero velocity at the droplet surface (at different elevations depending on $\mathrm{x}/\mathrm{h_d}$ location) showing the no slip boundary condition. A bit down the $x/h_d = 0$, the x-velocity starts from zero but then shows a very small negative value (opposing the main flow direction) near the droplet surface, which goes on following the x/h_d to downstream of the droplet. This shows the flow separation point (in the midplane) is on top of the droplet. The angle at which the flow separates is greater than 90° (i.e. the back flow is seen after $x/h_d = 0$ i.e. the midpoint of droplet contact line). The exact separation angle, however, is confirmed using pressure contours (see sections 4.4.1 and 4.4.2).

Figure 4-3c shows the normalized x-velocity profiles downstream of the droplet. The x-velocity at the locations of $x/h_d = 2$, and $x/h_d = 3$ exhibit negative values where $y/h_d \leq 1$ (i.e. below the shear layer). That area with negative velocity values, correspond to the recirculation zone downstream of the droplet. Starting from $x/h_d = 4$, the x-velocity shows positive values at every elevation, meaning the recirculation zone ends somewhere between $x/h_d = 3$ and $x/h_d = 4$, and the flow continues in the direction of the main stream.

A

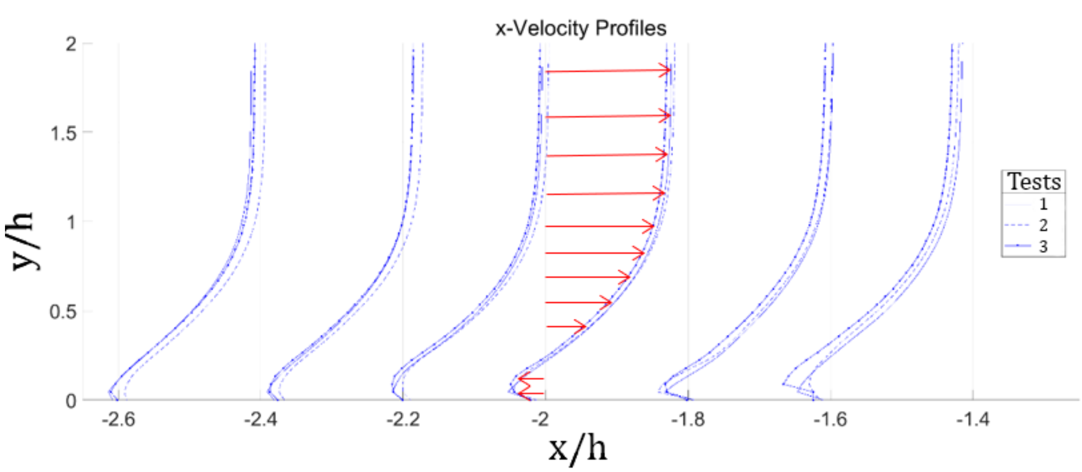

Continues next page…

B

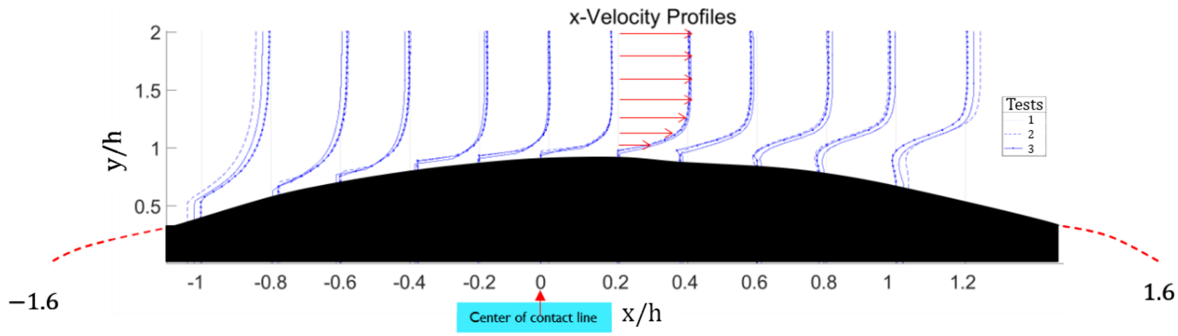

C

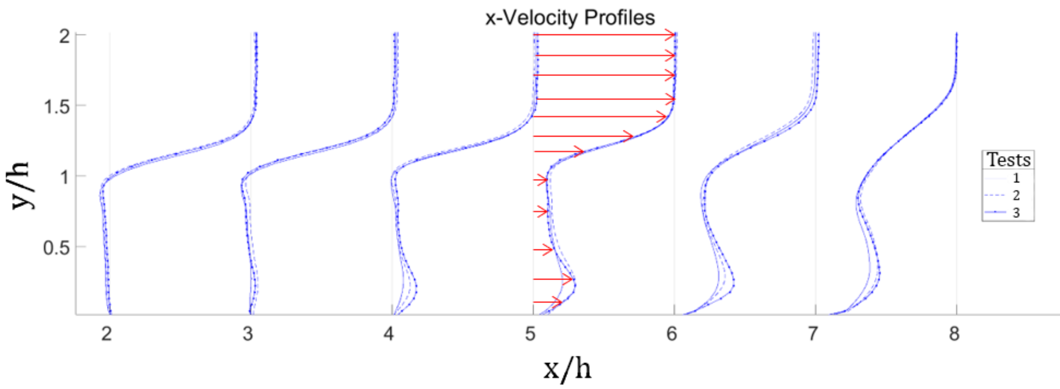

Figure 4-3. The normalized x-velocity profiles over a sessile droplet throughout the field (PMMA - 30 μl) shown for 3 different tests (for the repeatability purpose) (represented by three line types). (The center of the droplet contact line is located at 0). A) The profiles for the upstream of the droplet at equal spacings of 0.2 $^{x}/_{h_d}$. B) The profiles over the droplet at equal spacings of 0.2 $^{x}/_{h_d}$. C) The profiles for the downstream of the droplet at equal spacings of $^{x}/_{h_d}$. The distance between the grids is equal to 1 in terms of the velocity. $U_\infty = 8.4\ m/s$

4.1.3 Normalized y-velocity contour (PMMA - 30 μl)

Figure 4-4 shows the normalized y-velocity contour for air flow over a 30 μl droplet sitting on PMMA surface. Illustrated in Figure 4-4, the y-velocity is mostly quite close to zero throughout the field. Aside from that, two small regions behind (upstream) the droplet are seen. The one small blue area which represents a negative velocity is seen due to the vortex created there. The red area behind and on top of the droplet represents positive y-velocities in that region and that is due to the flow following the droplet surface. The other red area shown downstream the droplet corresponds to the flow joining the free stream after the recirculation zone. The flow in the recirculation zone also show a positive value for y-velocity, but the values are so small due to the low velocity in the wake area. Thus, the y-velocity for the recirculation zone is shown with darker green which relates to quite small positive values.

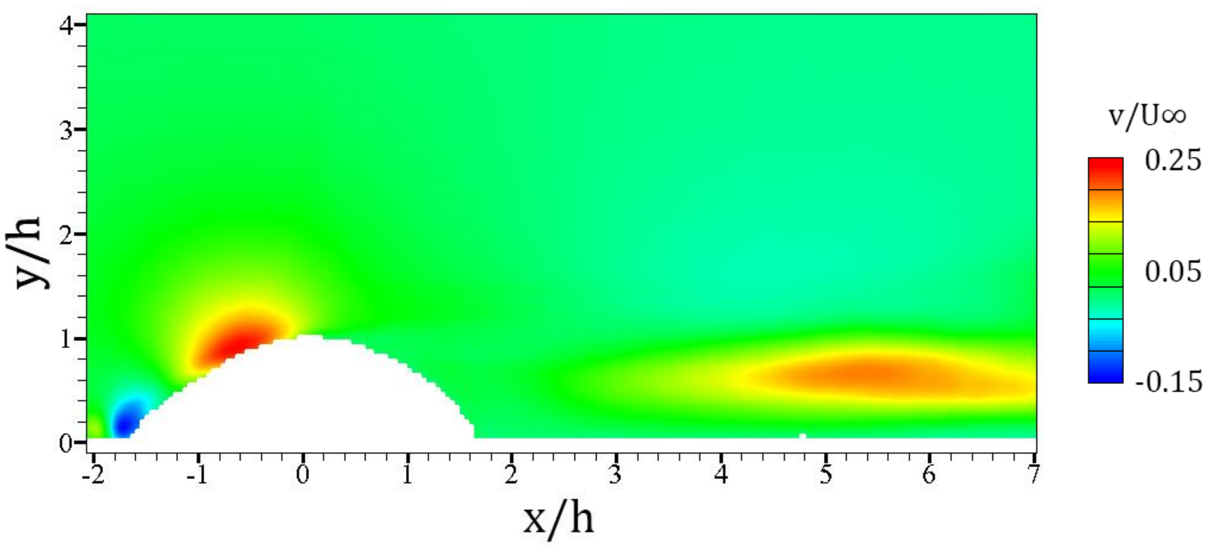

Figure 4-4. normalized y-velocity contour with streamlines for flow over a sessile droplet (PMMA - 30 μl). $U_{\infty} = 8.4\ m/s$

4.1.4 Recirculation Length

The wake area downstream of the droplet is called the "recirculation zone"; the velocity magnitude is low and the flow direction is opposed to that of the main stream. The pressure in recirculation zone is significantly lower than the other areas in the field. Recirculation zone is important since it is a measure of how the flow is affected by the body (droplet). For instance, lower separation angle lead to longer recirculation zones. Or, even more importantly, recirculation length becomes very important in studies concerning the shedding of a system of droplets (multiple droplets) [36]. In that, droplets with longer recirculation lengths need to be placed farther from each other in order to be shed with the same critical air velocities as when are shed singly [29].

To analyze the recirculation length, the x-velocity contours were used; to be accurate, the contour values in the vicinity of zero velocity was used (see Figure 4-5). Due to the recirculation zone not being symmetric -which (being symmetric) is somehow the case for immersed bodies- the farthest point on the zone is used to calculate the recirculation length. The other end is the center of droplet contact line which is also the origin of the coordinate system. Then, based on Figure 4-5 the normalized recirculation length for a 30 μl droplet on a PMMA coated Aluminum surface is 4.2h [mm].

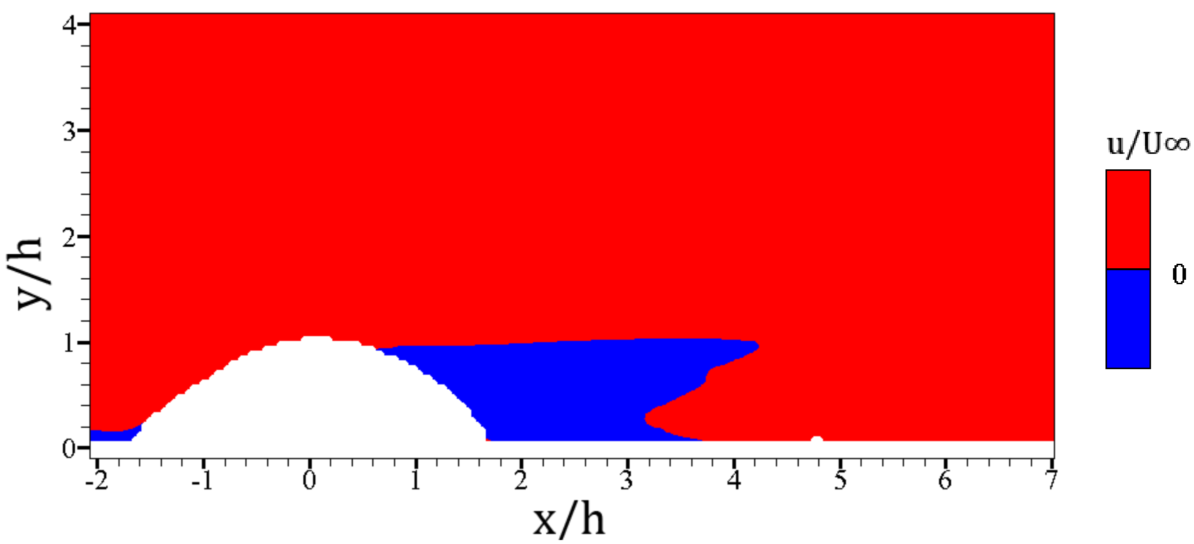

Figure 4-5. x-velocity contour used for the calculation of recirculation length for air flow over a 30 μl droplet on PMMA. $U_\infty = 8.4\ m/s$

4.1.5 Vorticity Contour (PMMA – $30\ \mu l$)

The normalized vorticity contour for a $30\ \mu l$ droplet on PMMA is illustrated in Figure 4-6. The normalization is done using the droplet height and the free stream velocity. Figure 4-6 indicates that the highest vorticity happens in the shear layer with the positive sign indicating a clockwise vorticity. This is in agreement with the expectations based on the results seen earlier for x-velocity contour and profiles. There are also areas below the shear layer with negative vorticity illustrated with a darker blue color. The negative vorticity shown with darker blue, shows that the direction of vorticity in recirculation zone is opposed to the shear layer which clockwise. Medium-level vorticities are also seen behind (upstream) the droplet and that is due to the immediate change in velocity and the vortex created behind the droplet. The level of the vorticity at the immediate vicinity of the droplet surface indicates the level by which the form drag (friction drag) is applied to the droplet.

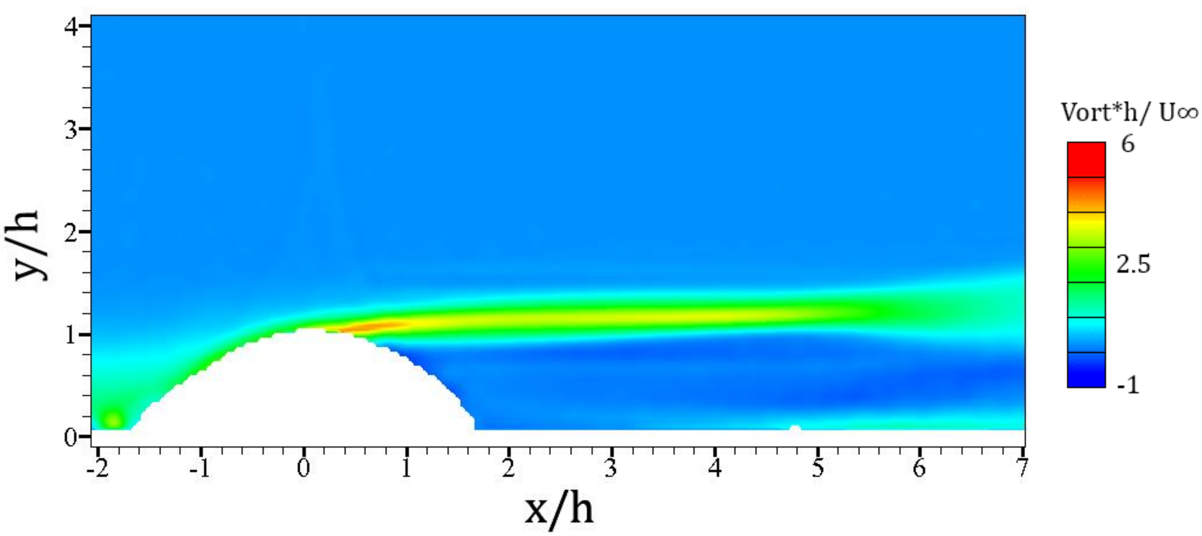

Figure 4-6. normalized vorticity contour for flow over a sessile droplet (PMMA - $30\ \mu l$).

$U_\infty = 8.4\ m/s$

4.1.6 The effect of wettability on streamlines and normalized x-velocity ($\bar{u}/U_\infty$)

The normalized x-velocity ($\bar{u}/U_\infty$) contours for the 12 cases studied (with 3 different sizes and 4 wettabilities) are shown below. Figure 4-7 shows the x-velocity contour and streamline patterns for droplets. The figure indicates, that irrespective of the wettability, the pattern of the x-velocity contours and streamlines are similar. Meaning that, a vortex is seen upstream the droplet for all cases. The patterns of streamlines in the recirculation zone, are similar to the one explained for a 30 µl droplet on PMMA (see section 4.1.1) and the shear layer is seen at $y/h \approx 1$.

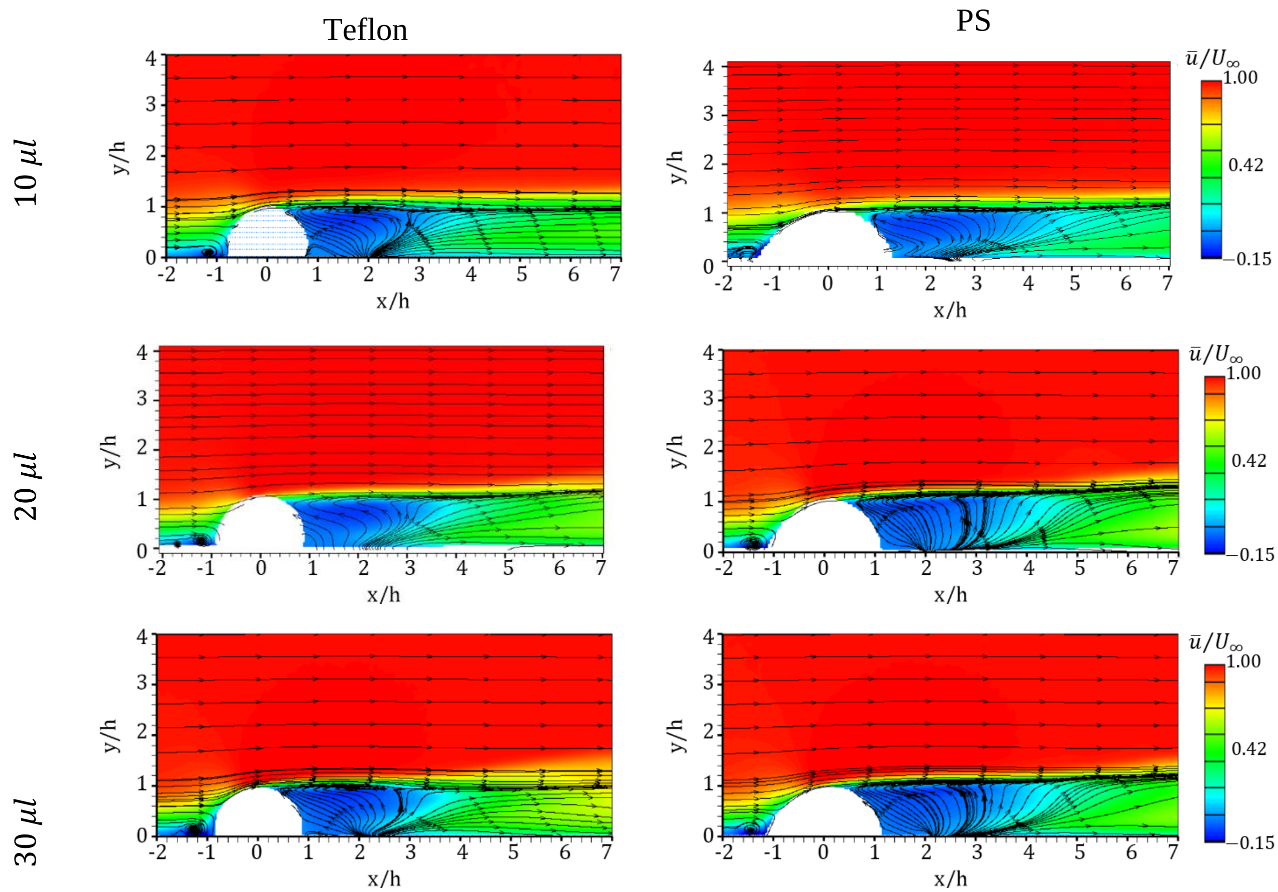

Continues next page…

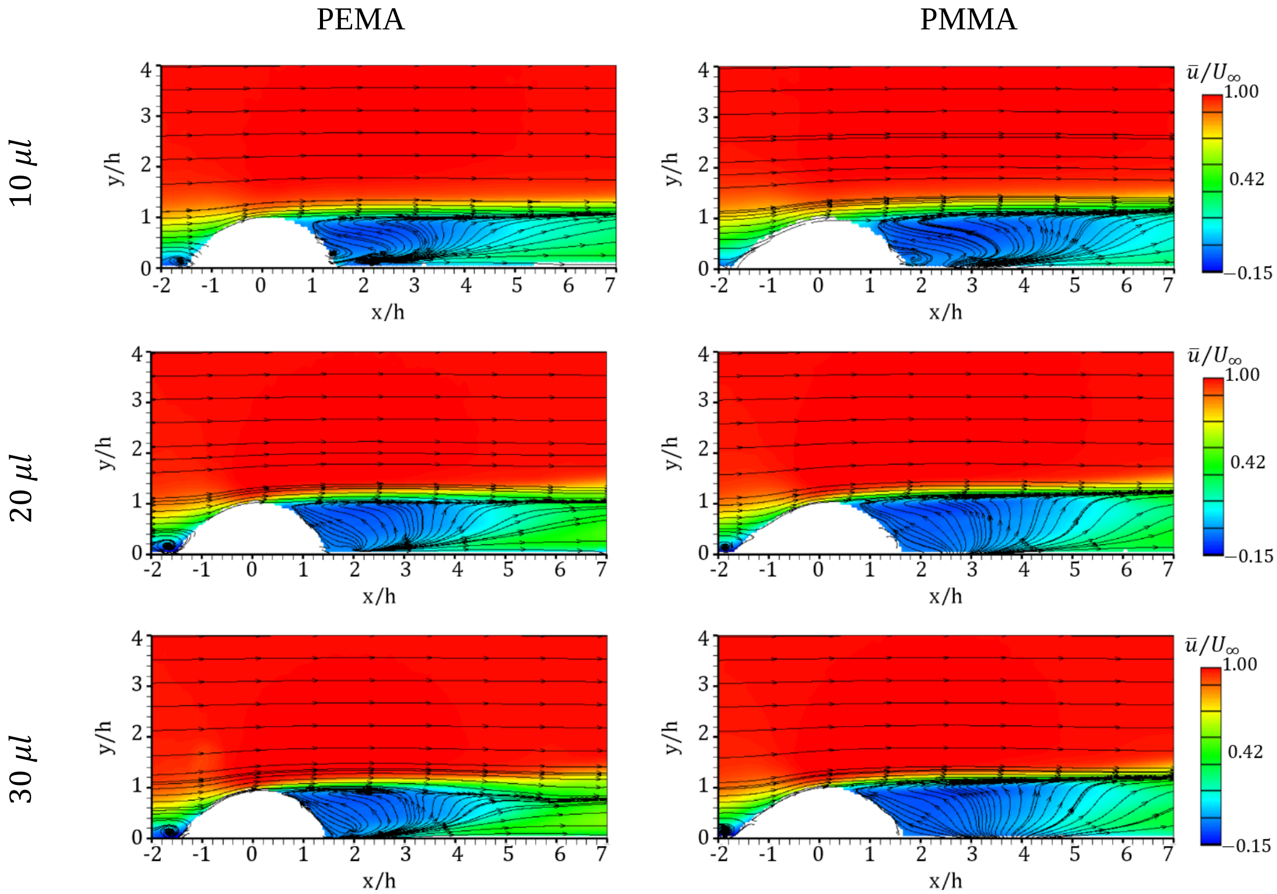

Figure 4-7. streamline patterns on x-velocity contours for different cases of study (wettability effect). Free stream velocities for droplets on Teflon: 10 μl) 5.6 m/s, 20 μl) 4.8 m/s, 30 μl) 4.5 m/s. Free stream velocities for droplets on PS: 10 μl) 8.5 m/s, 20 μl) 8.2 m/s, 30 μl) 6.6 m/s. Free stream velocities for droplets on PEMA: 10 μl) 8.9 m/s, 20 μl) 8.3 m/s, 30 μl) 8.1 m/s. Free stream velocities for droplets on PMMA: 10 μl) 10.8 m/s, 20 μl) 9.9 m/s, 30 μl) 8.4 m/s

Thus far, observed through the contours and streamlines, the wettability does not change the flow structure pattern. However, comparing contours could only help in general analysis. This means that the differences seen for shedding of droplets at different conditions (different surface wettabilities and drop sizes) are not due to the structure of the flow necessarily. To assess the similarities and differences in detail, velocity profiles, and recirculation length plots are used.

4.1.7 Wettability effect on normalized x-velocity upstream of the droplet (profiles)

Normalized x-velocity profiles upstream of the droplet is shown in Figure 4-8. The x-velocity profiles are shown for three different experiments for each case studied to show repeatability.

The profiles for all droplet sizes illustrated in Figure 4-8a, Figure 4-8b, and Figure 4-8c show that irrespective of the surface wettability, the normalized x-velocity contours upstream the droplets are similar. This is expected, as the Reynolds number are similar, and upstream of the droplet the flow is a typical "flow over a plate" not passing any obstruction.

The part that is close to the droplet that corresponds to the upstream vortex behind the droplet, also, was seen to be similar via the contours provided earlier. The profiles provide valid proof to the observations made by the contours and the streamlines, that regardless of the surface wettability, the normalized x-velocities upstream the droplet are the same. Meaning that, provided similar Reynolds numbers, the shearing boundary layer upstream the droplet is linearly effective with the free stream velocity (U_∞), for all surface wettabilities (since normalized velocity profiles are similar).

A

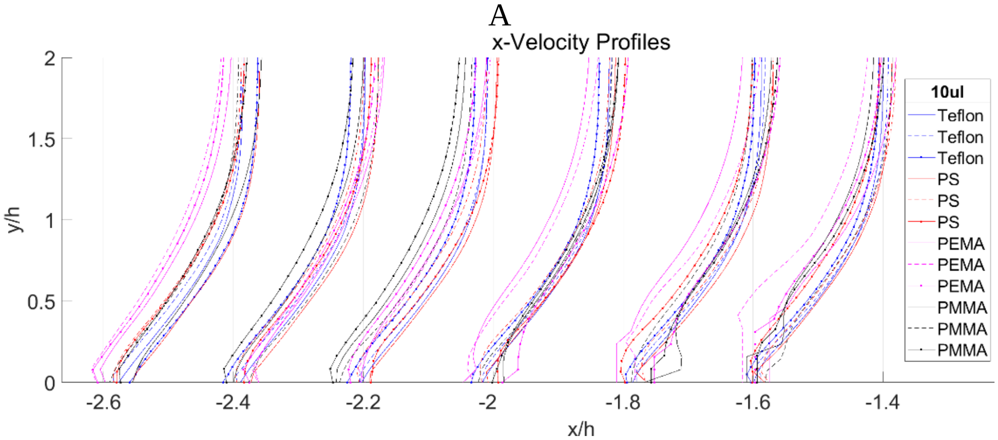

Continues next page…

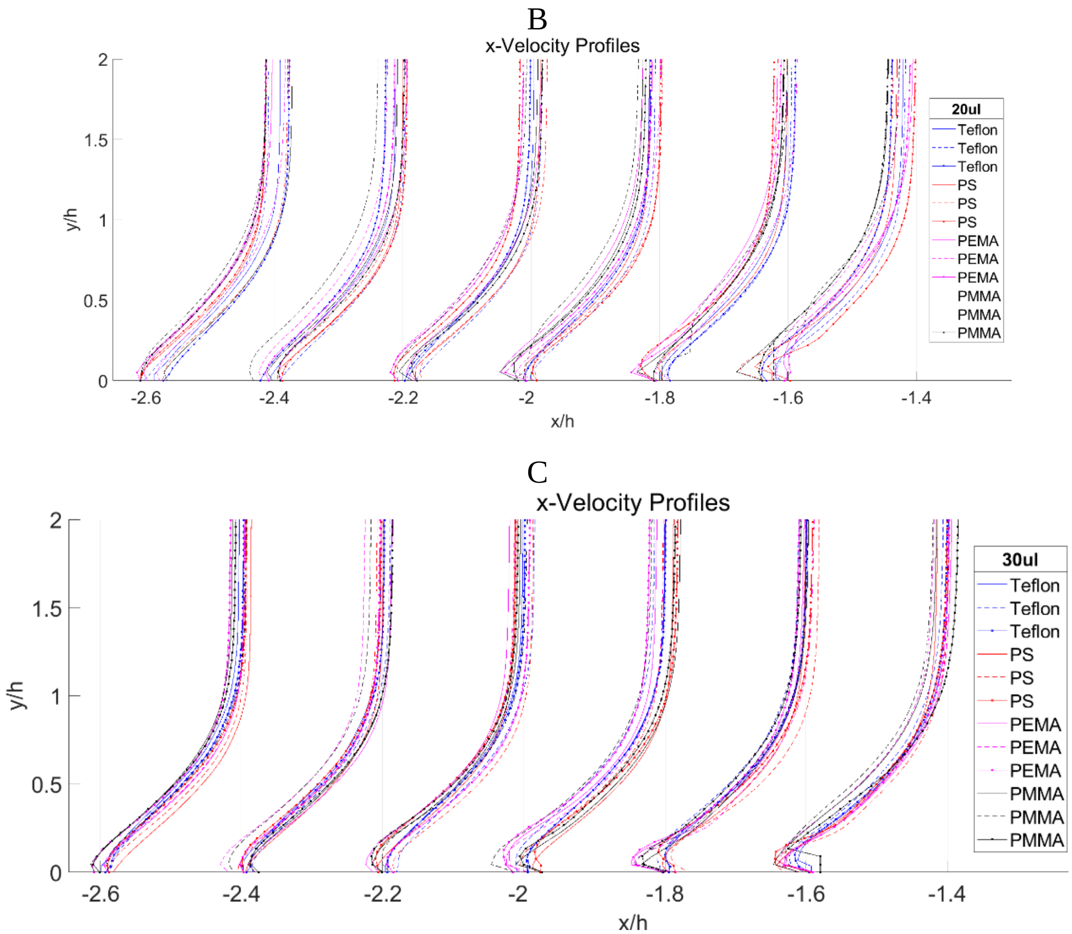

Figure 4-8. The effect of surface wettability on normalized x-velocity upstream the droplet. a) x-velocity profiles upstream the 10 μl droplets. b) x-velocity profiles upstream the 20 μl droplets. c) x-velocity profiles upstream the 30 μl droplets. Free stream velocities for droplets on Teflon: 10 μl) 5.6 m/s, 20 μl) 4.8 m/s, 30 μl) 4.5 m/s. Free stream velocities for droplets on PS: 10 μl) 8.5 m/s, 20 μl) 8.2 m/s, 30 μl) 6.6 m/s. Free stream velocities for droplets on PEMA: 10 μl) 8.9 m/s, 20 μl) 8.3 m/s, 30 μl) 8.1 m/s. Free stream velocities for droplets on PMMA: 10 μl) 10.8 m/s, 20 μl) 9.9 m/s, 30 μl) 8.4 m/s

4.1.1 Wettability effect on normalized x-velocity over the droplet

The normalized x-velocity profiles on the droplet are shown in Figure 4-9. Just as the profiles shown for upstream the droplet, the profiles for three different experiments for each case studied are illustrated for to show repeatability. It is seen that like the x-velocity profiles upstream of the droplets, irrespective of the surface wettability, the normalized x-velocity profiles match for all drop sizes in each x/h.

On the left end of the plots, however, some differences are seen where there is no slip condition. That is due to the droplets having different surface profiles. For instance, the velocity profile for Teflon starts at a higher elevation on the left side of the droplet, compared to PMMA. However, the plots show a quite similar normalized x-velocity profiles over the droplets, even on where the separation happens which is on the right side of the droplet.

Then, it is seen that the velocity profile upstream, and, on the droplet do not change noticeably with wettability. This is very important as it means that the coefficient of friction should be similar for droplets on different surface wettabilities.

A

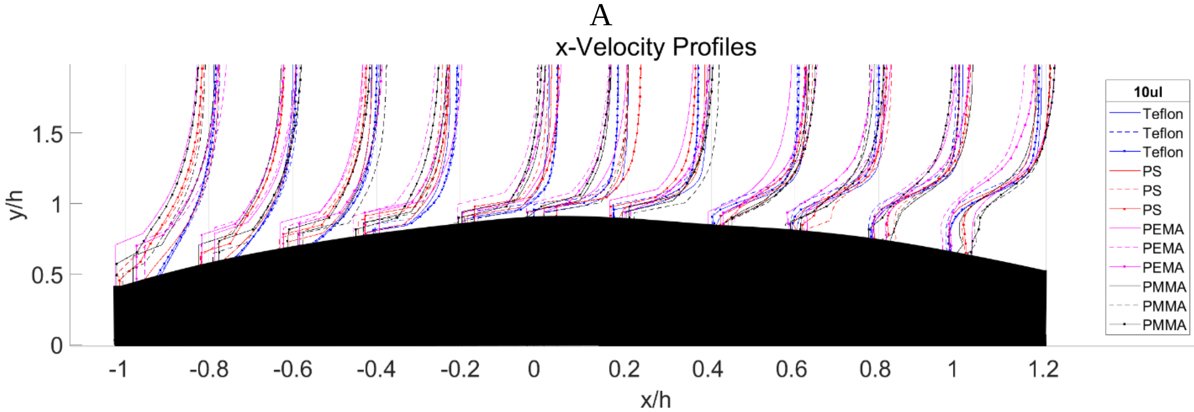

Continues next page…

B

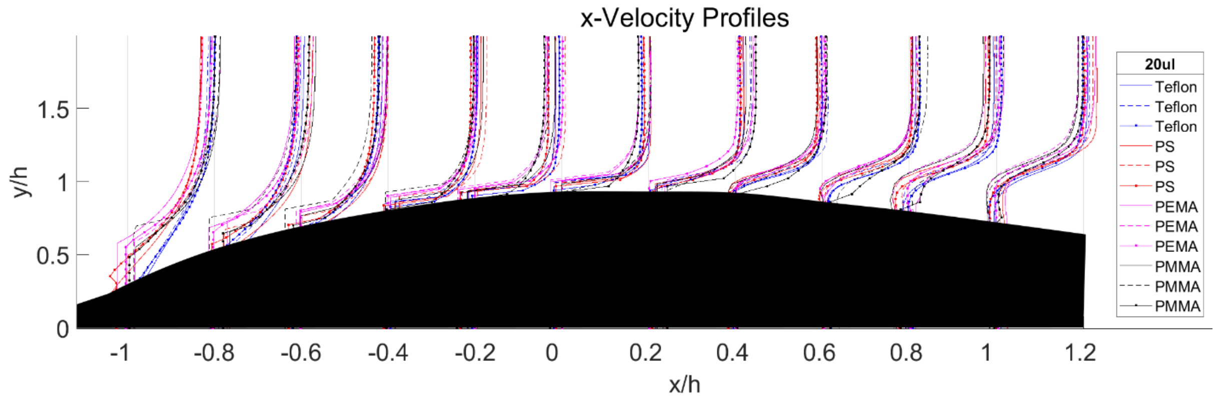

C

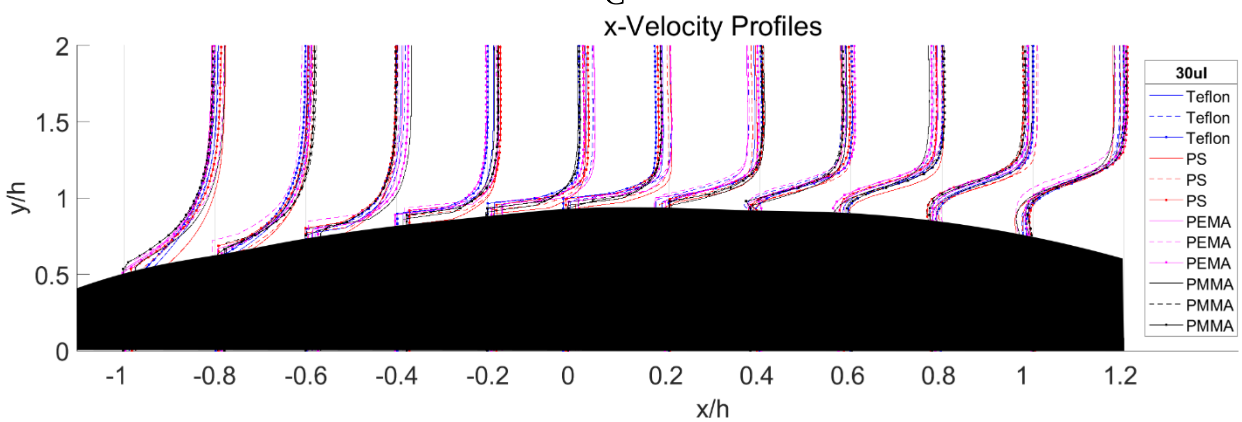

Figure 4-9. The effect of surface wettability on normalized x-velocity on the droplet. a) x-velocity profiles on the 10 μl droplets. b) x-velocity profiles on the 20 μl droplets. c) x-velocity profiles on the 30 μl droplets. Free stream velocities for droplets on Teflon: 10 μl) 5.6 m/s, 20 μl) 4.8 m/s, 30 μl) 4.5 m/s. Free stream velocities for droplets on PS: 10 μl) 8.5 m/s, 20 μl) 8.2 m/s, 30 μl) 6.6 m/s. Free stream velocities for droplets on PEMA: 10 μl) 8.9 m/s, 20 μl) 8.3 m/s, 30 μl) 8.1 m/s. Free stream velocities for droplets on PMMA: 10 μl) 10.8 m/s, 20 μl) 9.9 m/s, 30 μl) 8.4 m/s

4.1.2 Wettability effect on normalized x-velocity profiles downstream the droplet

The normalized x-velocity profiles downstream of the droplets are shown in Figure 4-10. The profiles for 10 μl droplets shown in Figure 4-10a, illustrate that the x-velocity below the shear layer, develops sooner for hydrophobic surfaces (Teflon and PS) compared to the hydrophilic surfaces (PMMA and PEMA). Meaning that the normalized x-velocities for Teflon and PS, reach higher values (closer to the x-velocity in the main flow) compared to PMMA and PEMA, which have lower normalized velocities below the shear layer. Especially, looking at the profiles at $x/_h =$ 4, the x-velocity for hydrophilic surfaces show negative values below the shear layer, while the profiles for hydrophobic surfaces show only positive values at the location. This means that longer normalized recirculation lengths for hydrophilic surfaces (PMMA and PEMA) are expected.

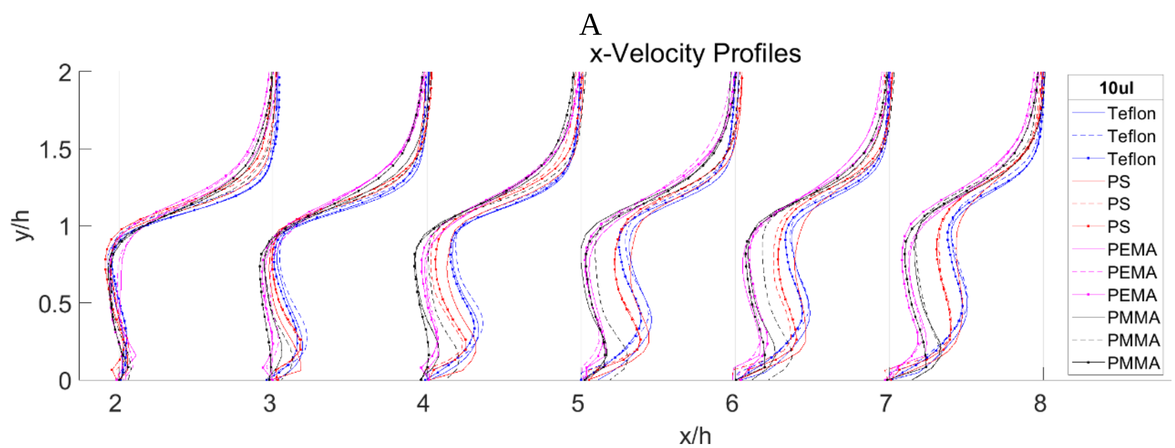

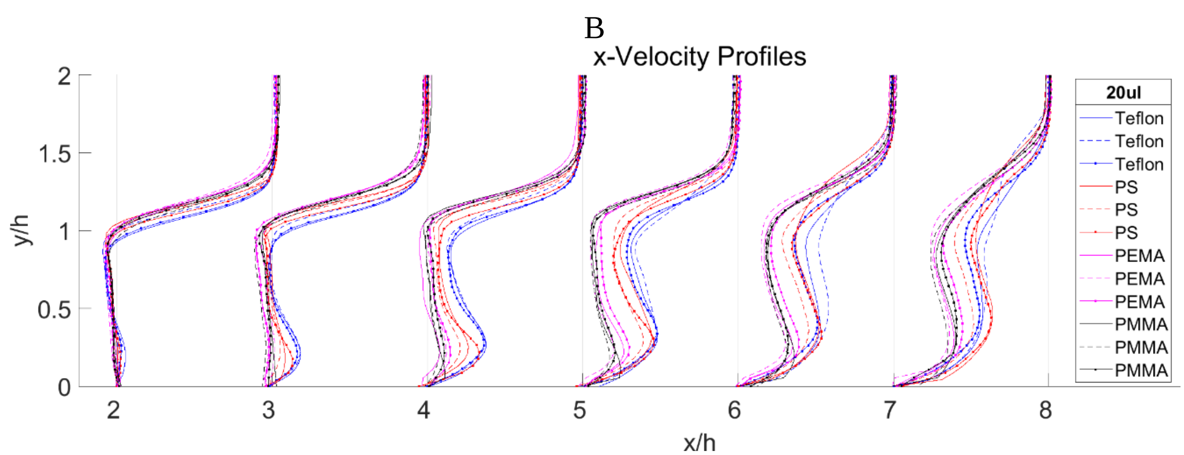

Continues next page…

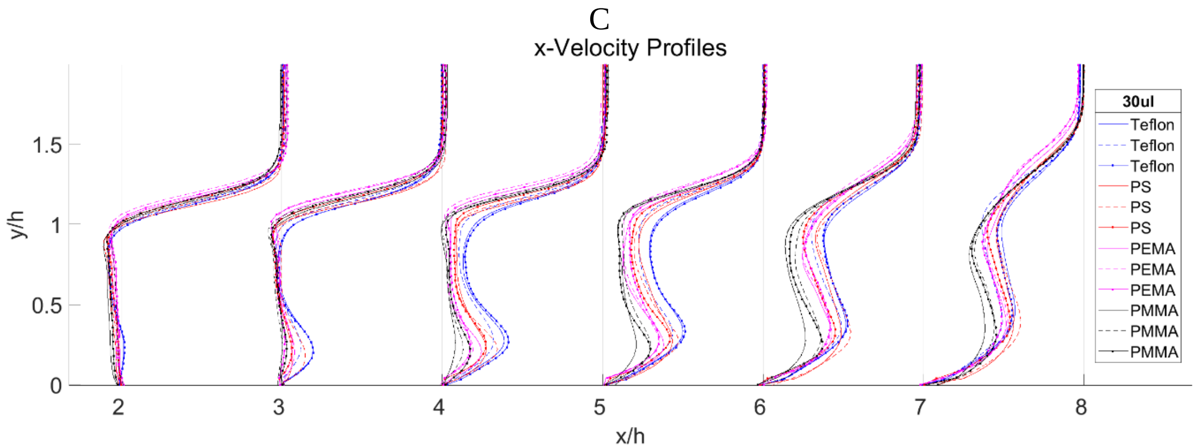

Figure 4-10. The effect of surface wettability on normalized x-velocity on the droplet. a) x-velocity profiles on the 10 μl droplets. b) x-velocity profiles on the 20 μl droplets. c) x-velocity profiles on the 30 μl droplets. Free stream velocities for droplets on Teflon: 10 μl) 5.6 m/s, 20 μl) 4.8 m/s, 30 μl) 4.5 m/s. Free stream velocities for droplets on PS: 10 μl) 8.5 m/s, 20 μl) 8.2 m/s, 30 μl) 6.6 m/s. Free stream velocities for droplets on PEMA: 10 μl) 8.9 m/s, 20 μl) 8.3 m/s, 30 μl) 8.1 m/s. Free stream velocities for droplets on PMMA: 10 μl) 10.8 m/s, 20 μl) 9.9 m/s, 30 μl) 8.4 m/s

Looking at the profiles for 20 μl and 30 μl droplets, illustrated in Figure 4-10b and Figure 4-10c respectively, the same implication could be made. However, these are not highly significant differences between the profiles.

This means that, with a slightly lower normalized recirculation length for hydrophobic surfaces and the considerably higher heights of the droplets placed on them:

- The “actual” recirculation length for sessile droplets on hydrophobic surfaces, are longer than those on hydrophilic surfaces; meaning that:
    - Droplets on hydrophobic surfaces should keep longer distances from each other to be shed independently (to depin at a critical velocity for a single droplet with the same conditions (wettability/size)).

4.1.3 The effect of wettability on recirculation length

The recirculation length values for air flow over sessile droplets on surfaces with different wettabilities are given in Figure 4-11. For 10 μl droplets as the hydrophobicity of the surface increases, the normalized recirculation length decreases. It means that, the more hydrophilic the surface, the longer the normalized recirculation length, which is in agreement with the observations made by velocity profiles.

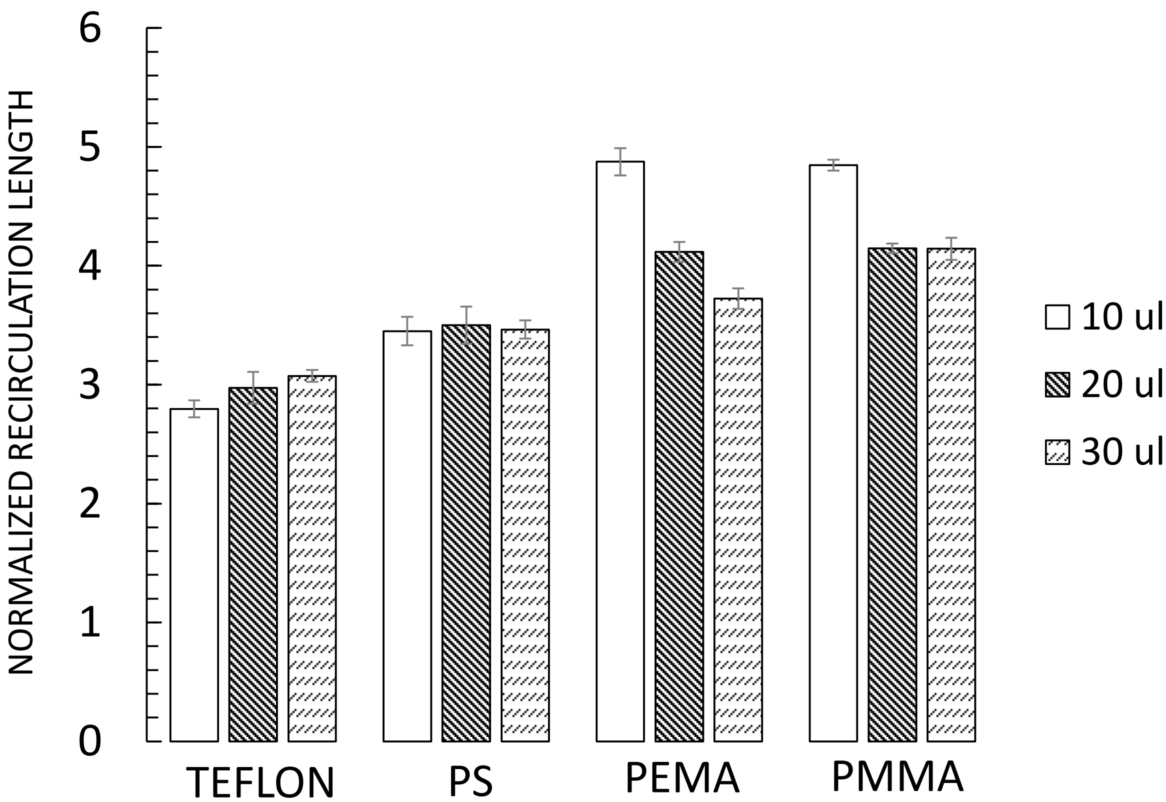

Figure 4-11. Normalized recirculation length values for air flow over sessile droplets. Free stream velocities for droplets on Teflon: 10 μl) 5.6 m/s, 20 μl) 4.8 m/s, 30 μl) 4.5 m/s. Free stream velocities for droplets on PS: 10 μl) 8.5 m/s, 20 μl) 8.2 m/s, 30 μl) 6.6 m/s. Free stream velocities for droplets on PEMA: 10 μl) 8.9 m/s, 20 μl) 8.3 m/s, 30 μl) 8.1 m/s. Free stream velocities for droplets on PMMA: 10 μl) 10.8 m/s, 20 μl) 9.9 m/s, 30 μl) 8.4 m/s

For 20 μl and 30 μl drops, the dependency of recirculation length to the surface wettability is the same as 10 μl droplets. This means that, irrespective of drop size (in the range considered), the more hydrophilic the surface, the longer the normalized recirculation length.

However, considering the heights of droplets on hydrophobic surfaces being significantly higher than those places on hydrophilic surfaces:

- The “actual” recirculation length for sessile droplets on hydrophobic surfaces, are slightly longer than those on hydrophilic surfaces; meaning that:
    - Droplets on hydrophobic surfaces should keep longer distances from each other to be shed independently (to depin at a critical velocity for a single droplet with the same conditions (wettability/size)).

4.1.4 The effect of wettability on the flow structure (conclusion)

To summarize the analyses made for the effect of surface wettability on the flow structure, the following points are put forward (considering the normalized data):

- The surface wettability does not change the overall flow structure around the droplet (in midplane). Meaning that the (patterns of) streamlines, x-velocity and y-velocity contours do not change considerably with the surface wettability (for all drop sizes).
- differences seen for shedding of droplets on different surfaces are not due to the structure of the flow.
- The velocity profiles indicate that the normalized velocity of air flow upstream and on a sessile droplet are identical for different surface wettabilities (for all drop sizes).

- provided similar Reynolds numbers, the shearing boundary layer upstream the droplet is linearly effective with the free stream velocity (U_∞), for all surface wettabilities (since normalized velocity profiles are similar).
- Coefficient of friction is similar for droplets on different surface wettabilities.
- The more hydrophilic the surface, the longer the normalized recirculation length (for all drop sizes).
- The "actual" recirculation length for sessile droplets on hydrophobic surfaces, are longer than those on hydrophilic surfaces. Meaning that, droplets on hydrophobic surfaces should keep longer distances from each other to be shed independently (to depin at a critical velocity for a single droplet with the same conditions (wettability/size)).

Having addressed the effect of surface wettability on the flow structure thoroughly, the following section focuses on the effect of drop size on the flow structure.

4.2 The effect of drop size on air flow structure over a sessile droplet

Having analyzed the effects of wettability on air flow structure over a sessile droplet, similar types of data are provided herewith to investigate the effect of drop size on air flow structure. As the sample results on air flow structure over a sessile droplet (PMMA - 30 μl) are provided in the previous section with a thorough analysis, the repetition in that case is avoided here. The results for air flow structure over a sessile droplet for the 12 cases of study (each being repeated three times) are provided in this section with an emphasis on the effect of drop size on the air flow structure.

4.2.1 The effect of drop size on normalized x-velocity ($\bar{u}/U_\infty$) contours and streamlines

The contours for normalized x-velocity of air flow over sessile droplets were shown in section 4.1.5. Figure 4-12 shows the normalized x-velocity contours with streamlines for sessile drops of different sizes on different surface wettabilities. Figure 4-12 strongly indicates that the drop size does not have a significant effect on the normalized x-velocity. This means that, the drop size does not change the pattern of the streamlines and the contours. Then, the differences seen for shedding of droplets in different sizes are not due to the structure of the flow.

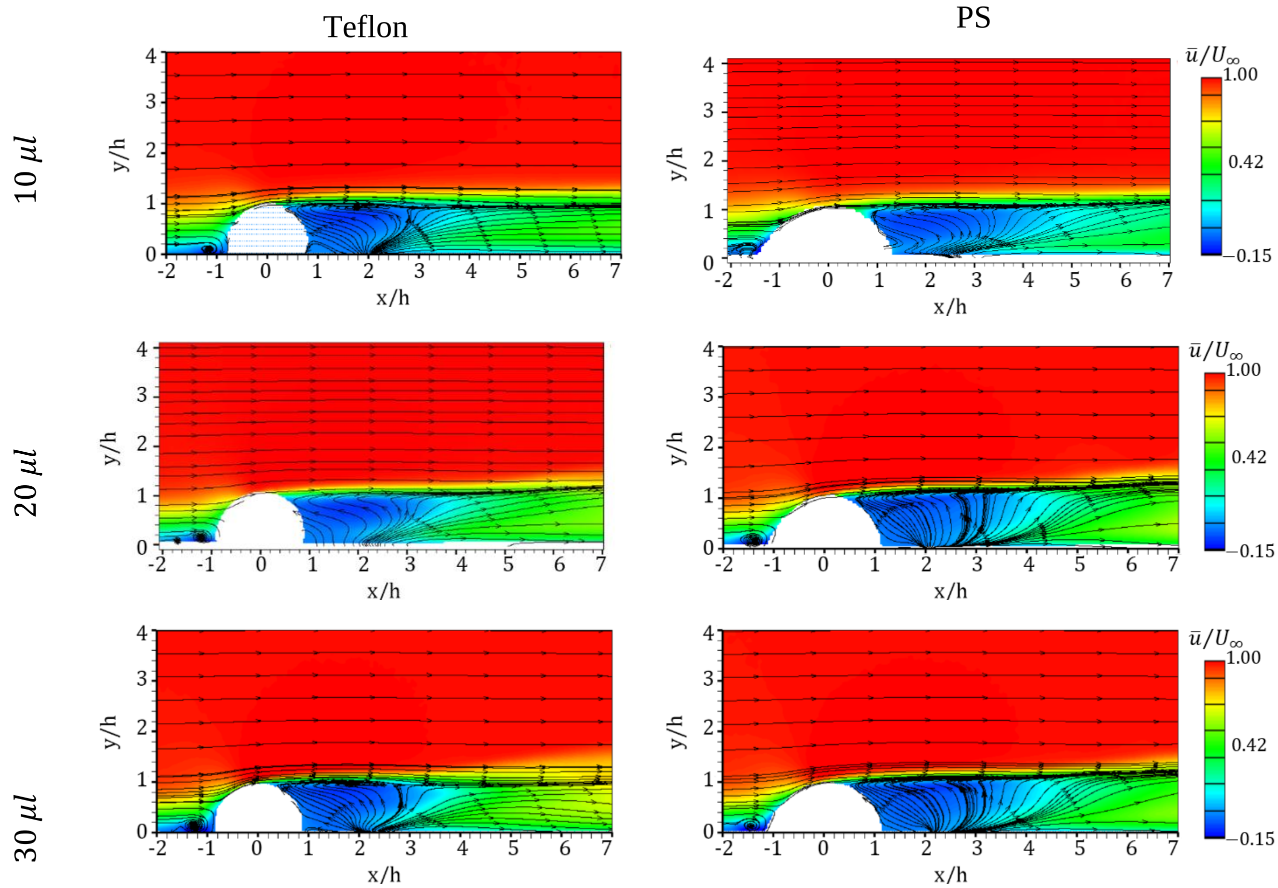

Continues next page…

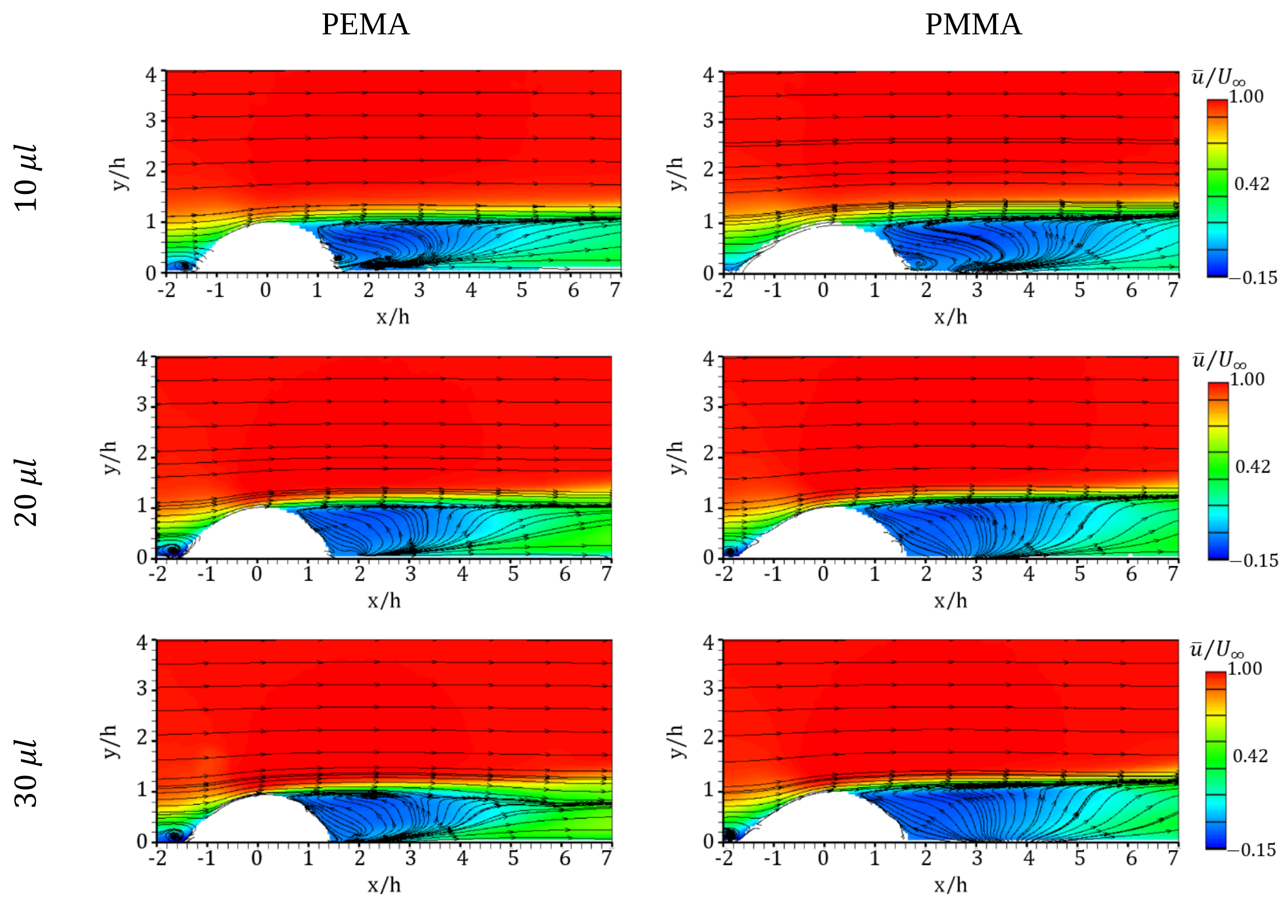

Figure 4-12. streamline patterns on x-velocity contours for different cases of study (drop size effect). Free stream velocities for droplets on Teflon: 10 μl) 5.6 m/s, 20 μl) 4.8 m/s, 30 μl) 4.5 m/s. Free stream velocities for droplets on PS: 10 μl) 8.5 m/s, 20 μl) 8.2 m/s, 30 μl) 6.6 m/s. Free stream velocities for droplets on PEMA: 10 μl) 8.9 m/s, 20 μl) 8.3 m/s, 30 μl) 8.1 m/s. Free stream velocities for droplets on PMMA: 10 μl) 10.8 m/s, 20 μl) 9.9 m/s, 30 μl) 8.4 m/s

To assess the effect of drop size more vigorously, however, x-velocity profiles and data on recirculation length is needed which is provided accordingly.

4.2.2 The effect of drop size on normalized x-velocity upstream the droplet (profiles)

The normalized x-velocity profiles upstream of the droplet are provided in Figure 4-13. The boundary layer upstream of the droplet is laminar for all cases ($3 \times 10^4 \leq Re_x \leq 7.2 \times 10^4$) and conforms to Blasius approximation. The x-velocity profiles upstream of the droplet does not change noticeably with drop size. This is expected as the profiles upstream of the droplet are the velocity profiles in the boundary layer and similar Reynolds numbers are expected to yield similar profiles in the boundary layer. For the region close to the droplet, the vortices from contours provided in 4.5.6, are seen to be similar in shape and size, so, them yielding to similar x-velocity profiles is reasonable.

The profiles provide valid proof to the observations made by the contours and the streamlines, that regardless of droplet size, the normalized x-velocities upstream the droplet are the same. Meaning that, provided similar Reynolds numbers, the shearing boundary layer upstream the droplet is linearly effective with the free stream velocity (U_∞), for all drop sizes (since normalized velocity profiles are similar).

A

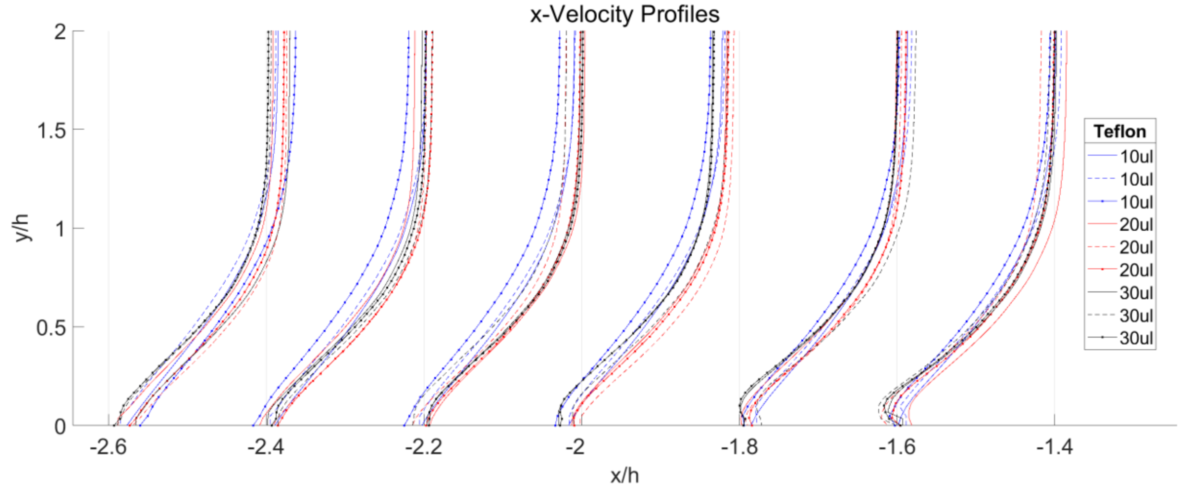

B

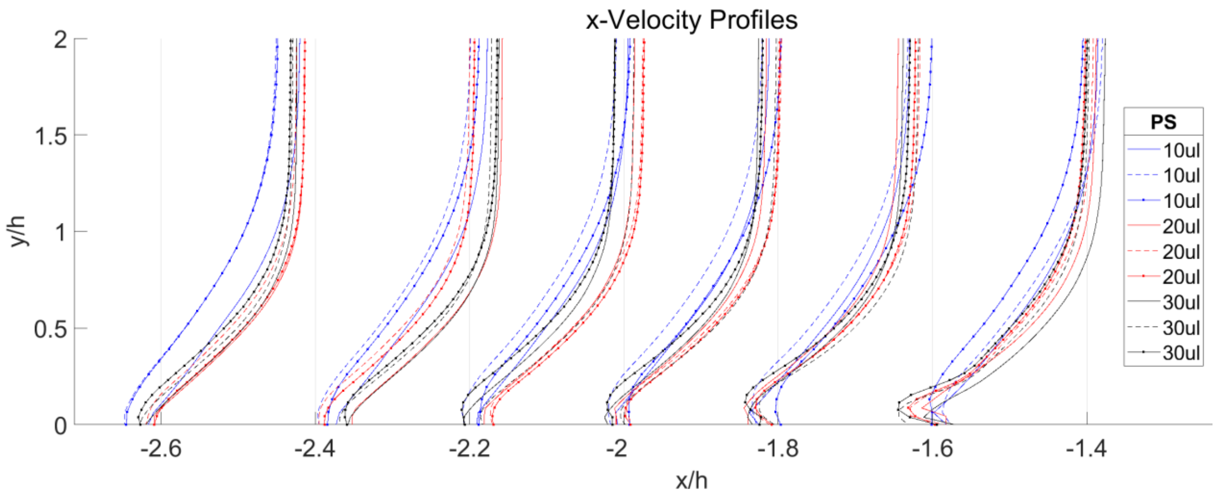

C

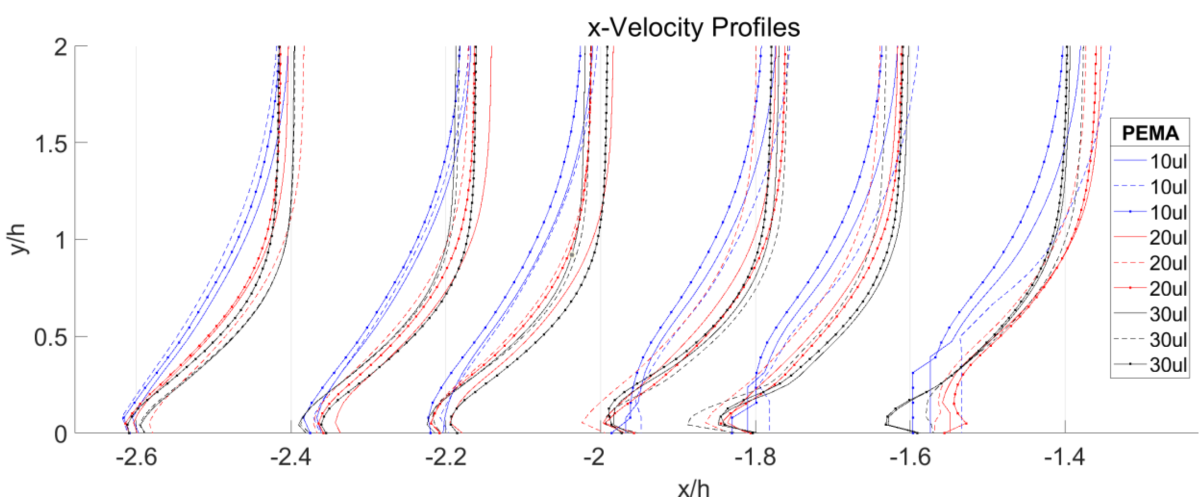

Continues next page…

D

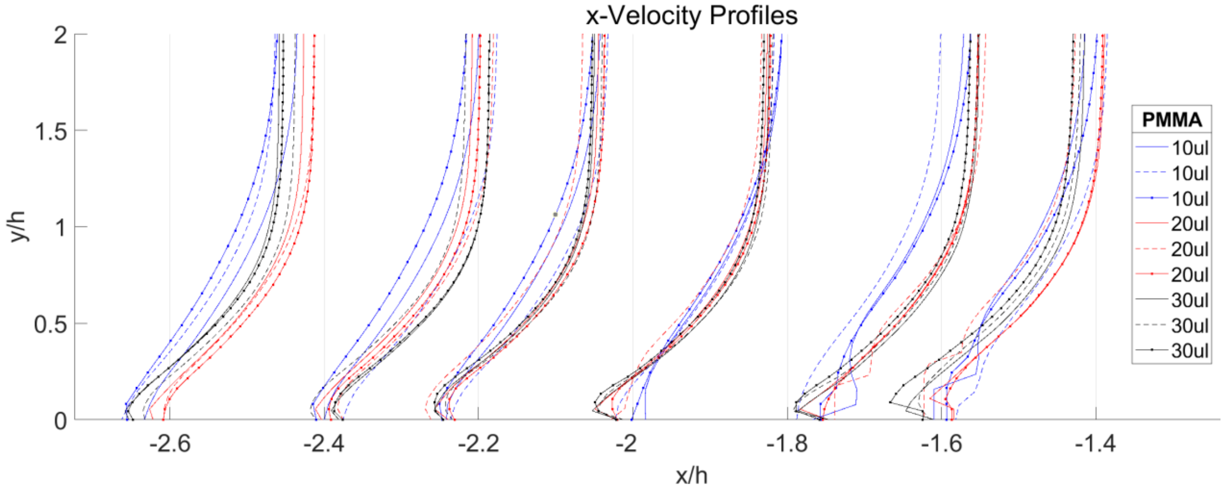

Figure 4-13. The x-velocity profiles upstream the droplet for different wettabilities a) The profiles for droplets with different sizes on Teflon b) The profiles for droplets with different sizes on PS a) The profiles for droplets with different sizes on PEMA a) The profiles for droplets with different sizes on PMMA. Free stream velocities for droplets on Teflon: $10\ \mu l)$ 5.6 m/s, 20 $\mu l)$ 4.8 m/s, 30 $\mu l)$ 4.5 m/s. Free stream velocities for droplets on PS: $10\ \mu l)$ 8.5 m/s, 20 $\mu l)$ 8.2 m/s, 30 $\mu l)$ 6.6 m/s. Free stream velocities for droplets on PEMA: 10 $\mu l)$ 8.9 m/s, 20 $\mu l)$ 8.3 m/s, 30 $\mu l)$ 8.1 m/s. Free stream velocities for droplets on PMMA: 10 $\mu l)$ 10.8 m/s, 20 $\mu l)$ 9.9 m/s, 30 $\mu l)$ 8.4 m/s

4.2.3 The effect of drop size on x-velocity profiles on the droplet (profiles)

The normalized x-velocity profiles on the droplets are shown in Figure 4-14 for four different wettabilities. Figure 4-14 shows that for all surface wettabilities, drop size do not change the x-velocity profiles upstream the droplet noticeably.

As seen so far, velocity profiles upstream, and, on the droplet do not change noticeably with wettability. The important message here is that the coefficient of friction should be similar for droplets with different sizes. The coefficient of friction ($C_f = \frac{\tau_w}{\frac{1}{2}\rho U_\infty^2}$) could be rewritten as follows:

$$C_f = 2\frac{\frac{du/U_\infty}{dy/h}}{Re_h} \tag{4-1}$$

A

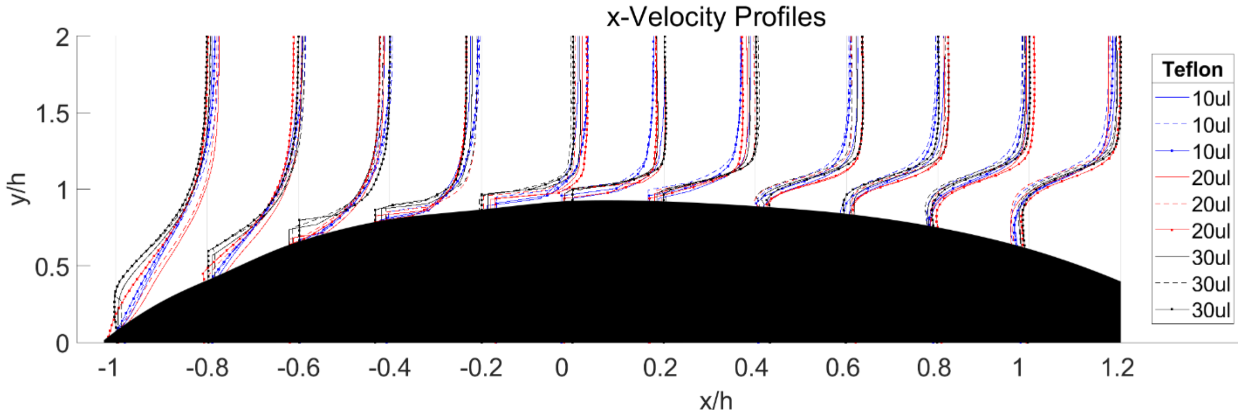

B

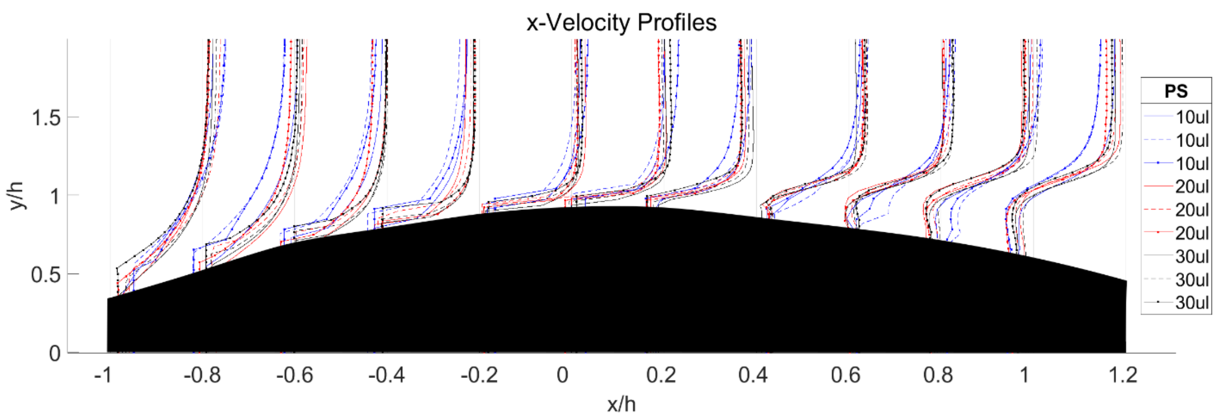

C

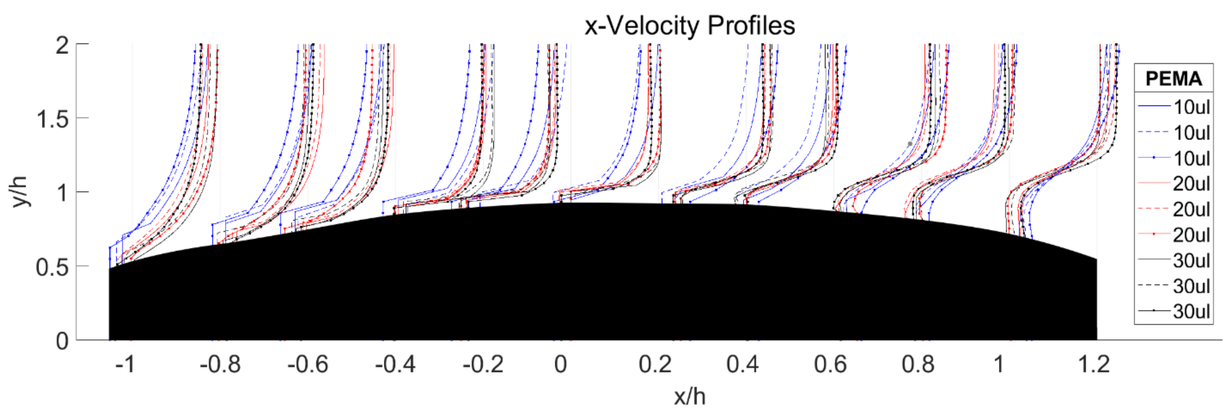

Continues next page…

D

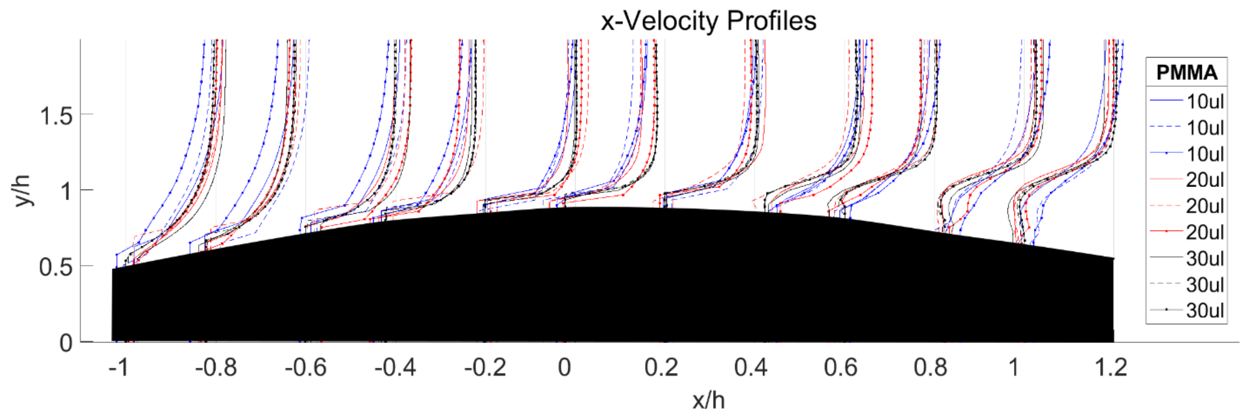

Figure 4-14. The x-velocity profiles on the droplet for different wettabilities a) The profiles for droplets with different sizes on Teflon b) The profiles for droplets with different sizes on PS a) The profiles for droplets with different sizes on PEMA a) The profiles for droplets with different sizes on PMMA (Each plot shows the normalized x-velocity profiles of air flow on droplets with three different sizes, which were done in three different experiments each). Free stream velocities for droplets on Teflon: 10 μl) 5.6 m/s, 20 μl) 4.8 m/s, 30 μl) 4.5 m/s. Free stream velocities for droplets on PS: 10 μl) 8.5 m/s, 20 μl) 8.2 m/s, 30 μl) 6.6 m/s. Free stream velocities for droplets on PEMA: 10 μl) 8.9 m/s, 20 μl) 8.3 m/s, 30 μl) 8.1 m/s. Free stream velocities for droplets on PMMA: 10 μl) 10.8 m/s, 20 μl) 9.9 m/s, 30 μl) 8.4 m/s

As the normalized velocity profiles on the droplets are similar (show similar slopes on the droplet profile), the coefficient of friction depends only on $\mathrm{Re_h}$. As Reynolds numbers based on drop heights ($\mathrm{Re_h}$) are similar for all cases, the drop size and wettability (as seen already) do not change the coefficient of friction of air flow over sessile droplets.

4.2.4 The effect of drop size on x-velocity downstream of the droplet (profiles)

The normalized x-velocity profiles for air flow downstream of the droplet are given in Figure 4-15. Figure 4-15a and Figure 4-15b indicate that there are no noticeable differences between the normalized x-velocity profiles with the drop size. This means that for hydrophobic surfaces, the drop size does not have a significant effect on changing the normalized x-velocity. Then, it is expected that the normalized recirculation length for droplets on hydrophobic surfaces do not differ considerably. Meaning that, as the droplets get larger, the recirculation length associated with them, increases linearly with their height. This means that, the distance to which two sessile droplets (on a hydrophobic surface) are shed independently from each other, proportionally changes with drop height.

A

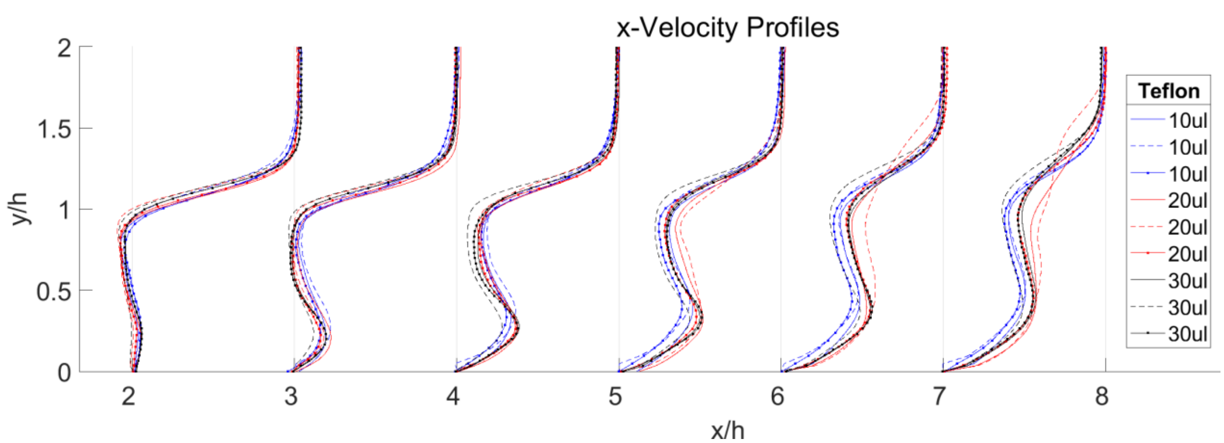

B

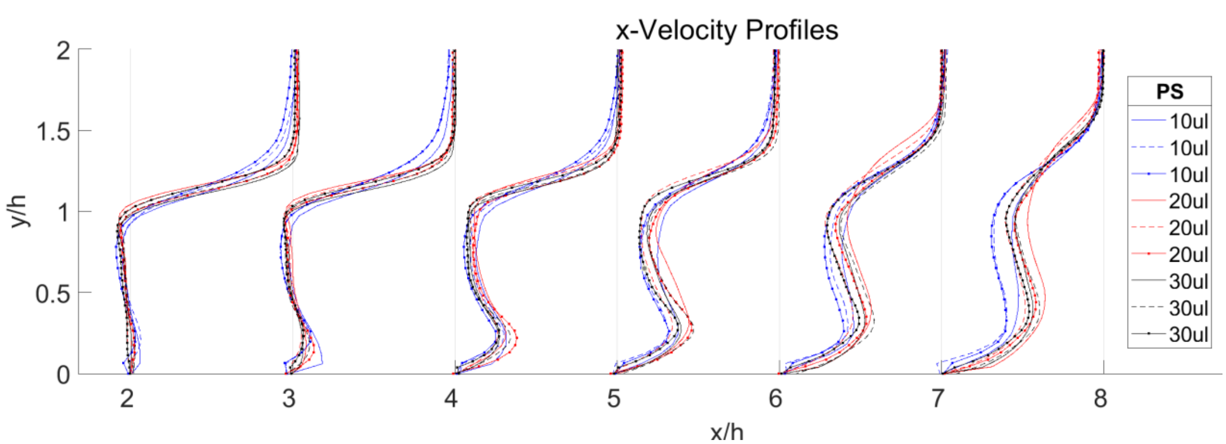

Continues next page…

C

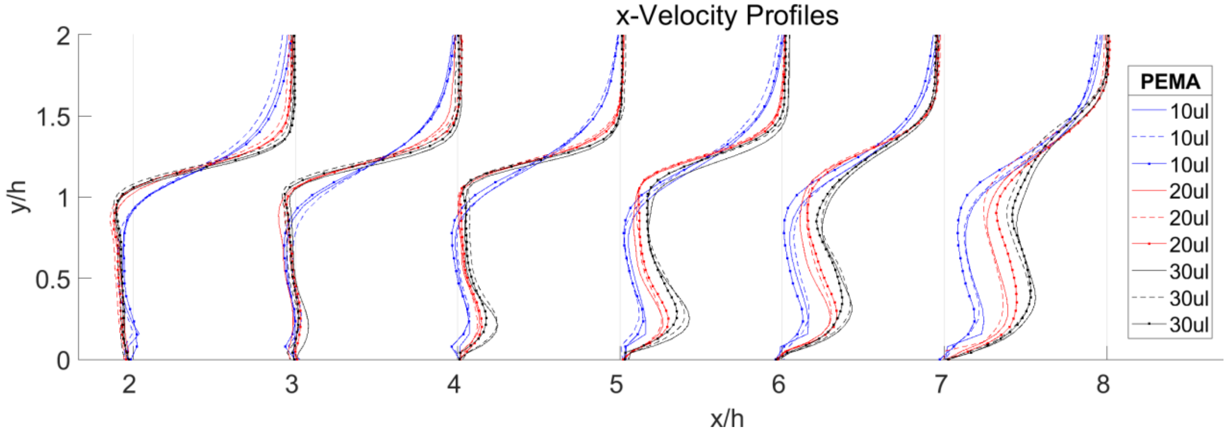

D

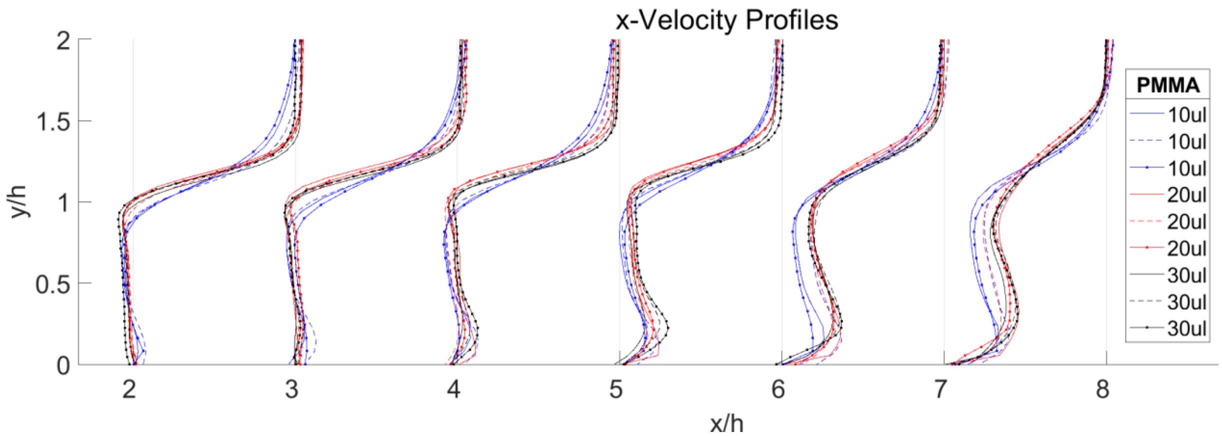

Figure 4-15. The x-velocity profiles downstream the droplet for different wettabilities a) The profiles for droplets with different sizes on Teflon b) The profiles for droplets with different sizes on PS a) The profiles for droplets with different sizes on PEMA a) The profiles for droplets with different sizes on PMMA. Free stream velocities for droplets on Teflon: 10 μl) 5.6 m/s, 20 μl) 4.8 m/s, 30 μl) 4.5 m/s. Free stream velocities for droplets on PS: 10 μl) 8.5 m/s, 20 μl) 8.2 m/s, 30 μl) 6.6 m/s. Free stream velocities for droplets on PEMA: 10 μl) 8.9 m/s, 20 μl) 8.3 m/s, 30 μl) 8.1 m/s. Free stream velocities for droplets on PMMA: 10 μl) 10.8 m/s, 20 μl) 9.9 m/s, 30 μl) 8.4 m/s

Figure 4-15c and Figure 4-15d, show the normalized x-velocity profiles downstream of the droplets placed on hydrophilic surfaces (PEMA and PMMA). The profiles indicate that, the smaller the droplet, the longer it takes for the velocity below the shear layer to develop and join the main flow. Then it is expected that the normalized recirculation lengths of smaller droplets (on hydrophilic surfaces) are longer than those of larger droplets.

Then it is expected that, the actual recirculation lengths of larger droplets (on hydrophilic surfaces) are only slightly longer than those of smaller droplets. Then, the distance to which two sessile droplets (on a hydrophilic surface) are shed independently from each other, increases only slightly with drop height.

4.2.5 The effect of drop size on normalized recirculation length

To understand the effect of drop size on normalized recirculation length, see Figure 4-16 for each surface wettability. The error bars show a "± standard deviation" from the average values calculated out of three separate experiments for each case study. For Teflon, Figure 4-16 indicates that with the size of droplets increasing, the normalized recirculation length increases slightly as well. For PS, the normalized recirculation length does not change noticeably with drop size. For hydrophilic surfaces, the Figure 4-16 illustrates that the smallest ($10\ \mu l$) droplets, cause the longest normalized recirculation length. And that the normalized recirculation length shortens with the droplets increasing in size (for hydrophilic surfaces).

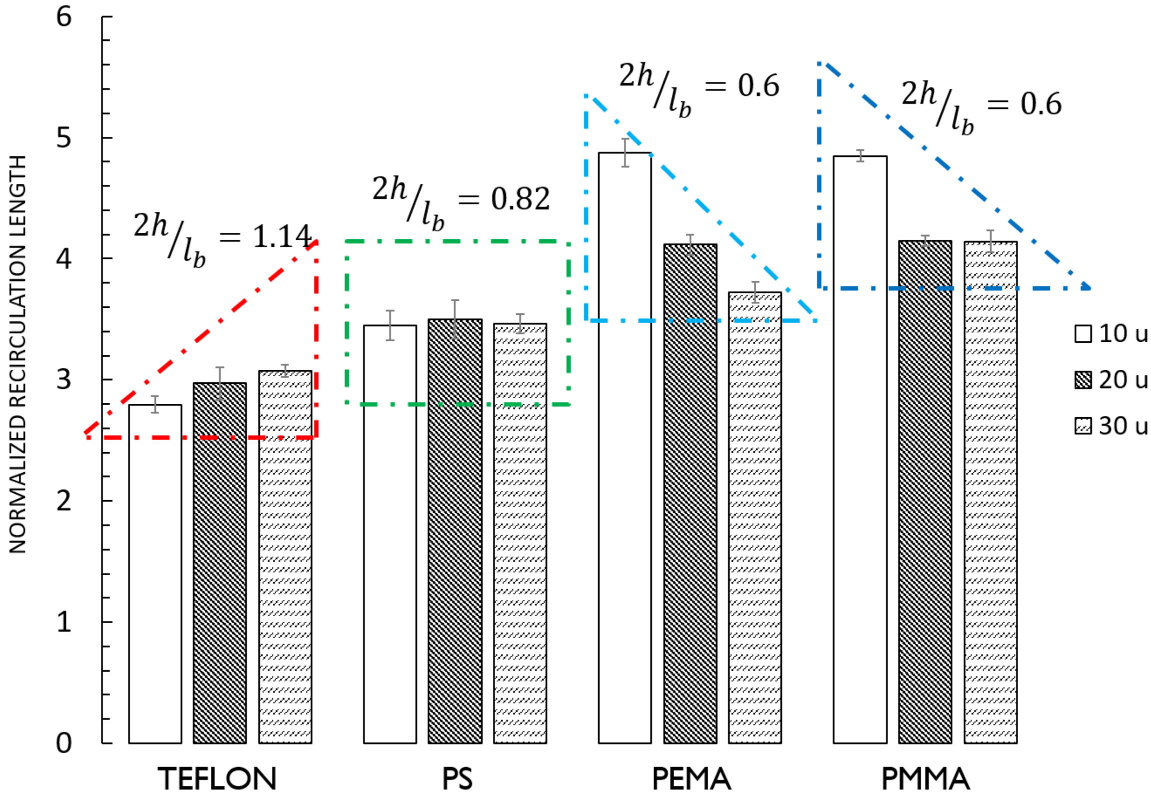

Figure 4-16. Recirculation length for air flow over sessile droplets (drop size effect). Free stream velocities for droplets on Teflon: 10 μl) 5.6 m/s, 20 μl) 4.8 m/s, 30 μl) 4.5 m/s. Free stream velocities for droplets on PS: 10 μl) 8.5 m/s, 20 μl) 8.2 m/s, 30 μl) 6.6 m/s. Free stream velocities for droplets on PEMA: 10 μl) 8.9 m/s, 20 μl) 8.3 m/s, 30 μl) 8.1 m/s. Free stream velocities for droplets on PMMA: 10 μl) 10.8 m/s, 20 μl) 9.9 m/s, 30 μl) 8.4 m/s

The reason why different wettabilities show different trends for the effect of drop size on normalized recirculation length, relates to different aspect ratios of drops on these surfaces. For hydrophobic surfaces (Teflon), the ratio of the height to the contact line radius ($\frac{h}{l_b/_2}$) is high. With the droplets on Teflon increasing in size, the height increases such that the droplet blocks the air flow more significantly than when the droplet was small. This causes the normalized recirculation lengths to be longer for larger droplets on hydrophobic surfaces. For hydrophilic surfaces, however, $\frac{h}{l_b/_2}$ ratio is quite low, meaning that the droplets are more spread out over the surface rather than being high in height (h). For larger droplets, the droplets spread over the surface more significantly than their heights being increased. This causes the air flow to go over the droplet more smoothly, thus, makes the normalized recirculation length -which is caused by the droplet blocking the air flow- smaller.

For PS, the ratio of the droplet being spread over the surface and increase in height falls somewhere in between the hydrophilic and hydrophobic surfaces. This obviously means that the increase in further blockage by drop height being increased is overcome by the droplet spreading over the surface with makes the air flow to smoothly go over the droplet. Then, the droplet size does not have a significant effect on the normalized recirculation size downstream the droplet.

Given the "actual" recirculation length seen for droplets with different sizes on hydrophilic and hydrophobic surfaces:

- For hydrophobic surfaces, the distance to which two sessile droplets are shed independently from each other, proportionally changes with drop height.
- For hydrophilic surfaces, the distance to which two sessile droplets are shed independently from each other, increases only slightly with drop height.

4.2.6 The effect of drop size on the flow structure (conclusion)

Given the results and analyses provided for the effect of drop size on the flow structure, to summarize, the following conclusions are made:

- The size of the droplet does not change the overall flow structure as in the (pattern of) streamlines, x-velocity and y-velocity contours.

- the differences seen for shedding of droplets in different sizes are not due to the structure of the flow.
- The velocity profiles upstream and on the droplet are identical for different drop sizes.
- provided similar Reynolds numbers, the shearing boundary layer upstream the droplet is linearly effective with the free stream velocity (U_∞), for all drop sizes (since normalized velocity profiles are similar).
- the coefficient of friction should be similar for droplets with different sizes.
- The normalized recirculation length of the air flow over a sessile droplet increases with drop size when the surface is hydrophobic.
- The normalized recirculation length of the air flow over a sessile droplet decreases with drop size when the surface is hydrophilic.
- For hydrophobic surfaces, the distance to which two sessile droplets are shed independently from each other, proportionally changes with drop height.
- For hydrophilic surfaces, the distance to which two sessile droplets are shed independently from each other, increases only slightly with drop height.

4.3 The effect of drop oscillations on the air flow structure

To understand the effect of drop oscillations on air flow characteristics, the droplet shapes (at the verge of shedding) were analyzed, their CAD models designed using Solidworks and 3D-printed. The 3D-printed droplet mockups were used to isolate the effect of drop oscillations on flow structure and turbulence statistics over a sessile droplet.

4.3.1 Structure of air flow over droplet mockups

The x-velocity contours along with streamlines for air flow over sessile droplets on "Teflon" surface and their solid mockups are provided in Figure 4-17. The results show a noticeable similarity between the air flow over sessile droplets and their mockups. Meaning that both normalized x-velocity contours and streamlines are similar for the droplets and their solid mockups.

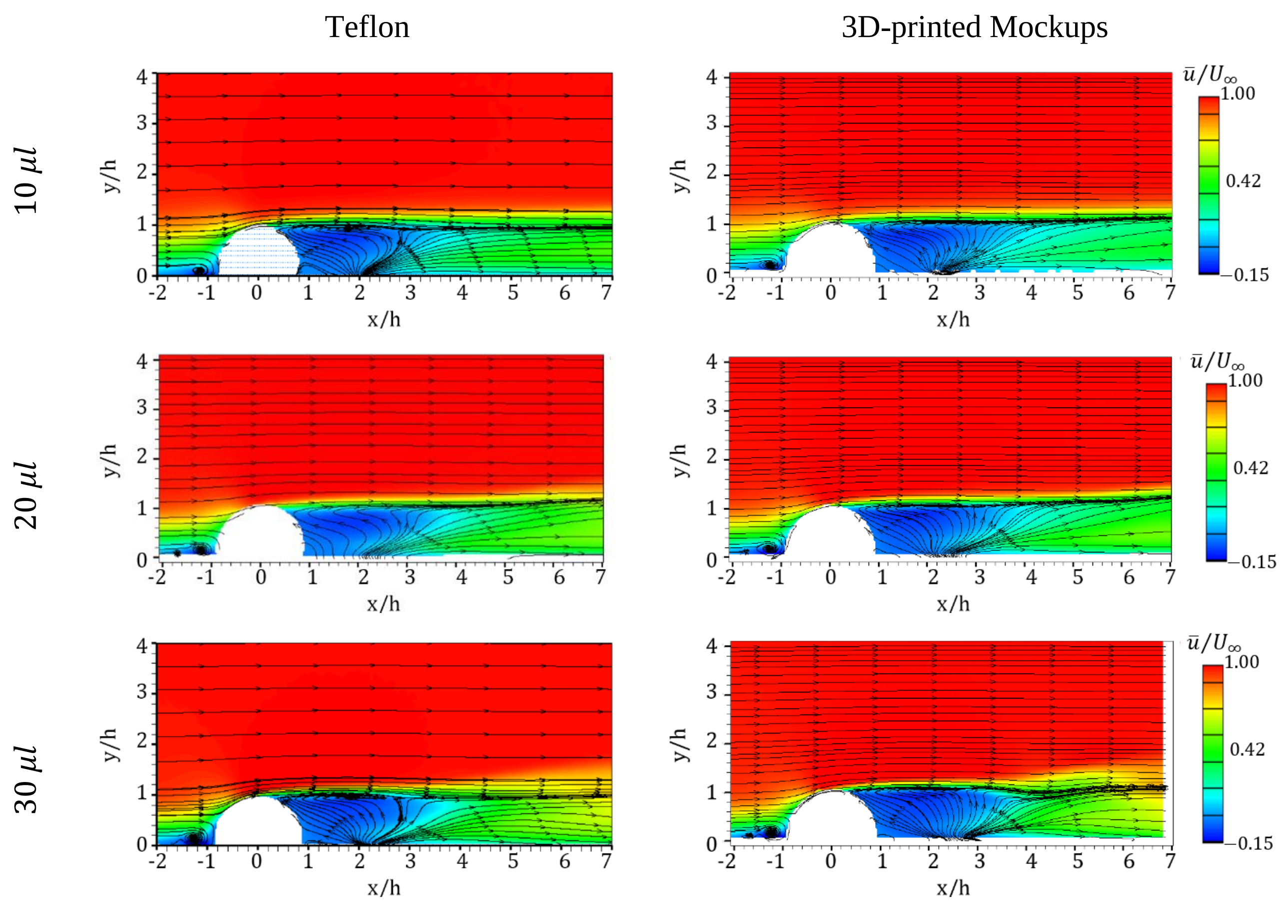

Figure 4-17. streamline patterns on x-velocity contours for droplets with different sizes on Teflon vs. their associated solid mockups. Free stream velocities for droplets on Teflon: 10 μl) 5.6 m/s, 20 μl) 4.8 m/s, 30 μl) 4.5 m/s.

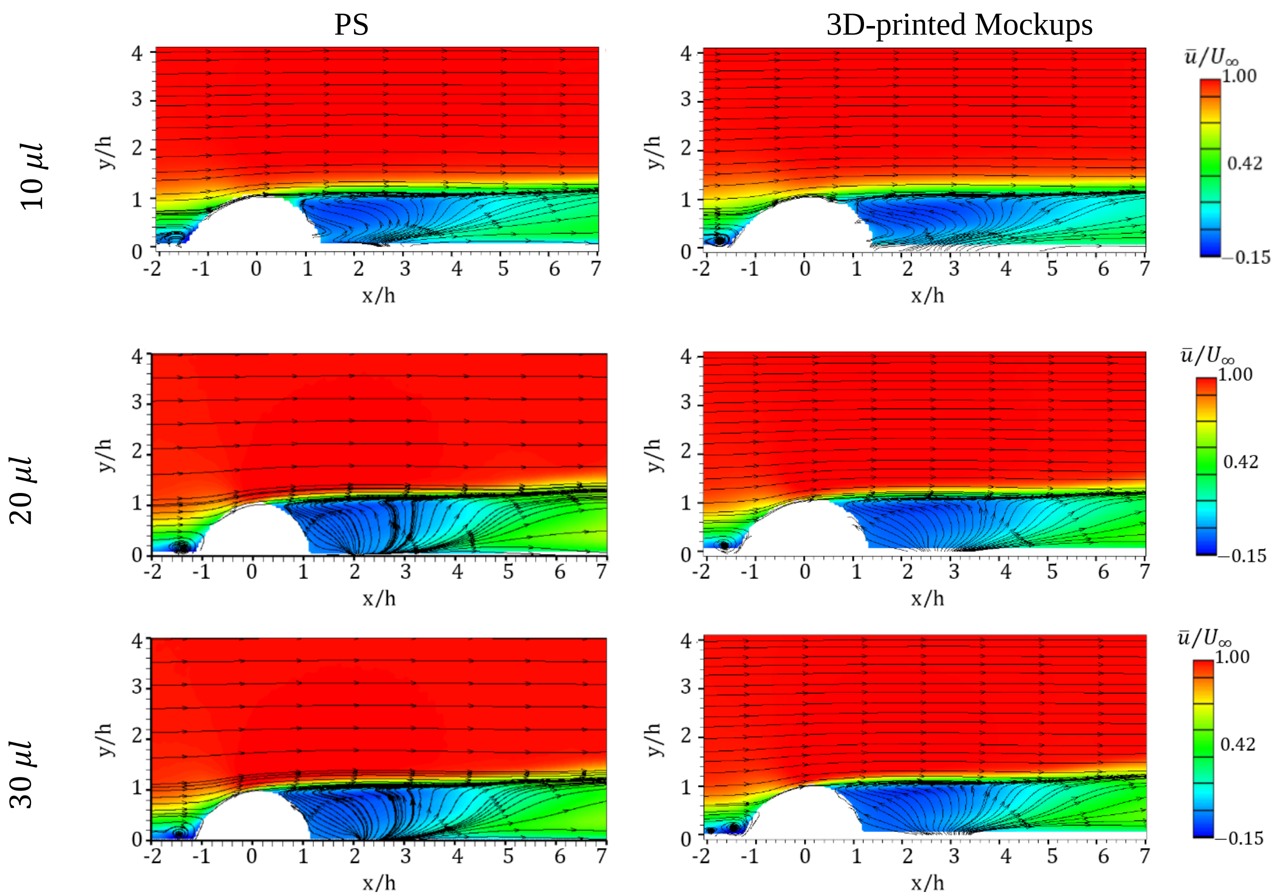

Figure 4-18. streamline patterns on x-velocity contours for droplets with different sizes on PS vs. their associated solid mockups. Free stream velocities for droplets on PS: 10 μl) 8.5 m/s, 20 μl) 8.2 m/s, 30 μl) 6.6 m/s.

The same results for droplets on PS and their solid mockups are shown in Figure 4-18. The results show again similarity in terms of streamlines and normalized x-velocity contours.

The normalized x-velocity contour for air flow over sessile droplets placed on PEMA and their solid mockups are shown in Figure 4-19. Illustrated in the figure, the streamlines and normalized x-velocity for the droplets and their mockups are similar.

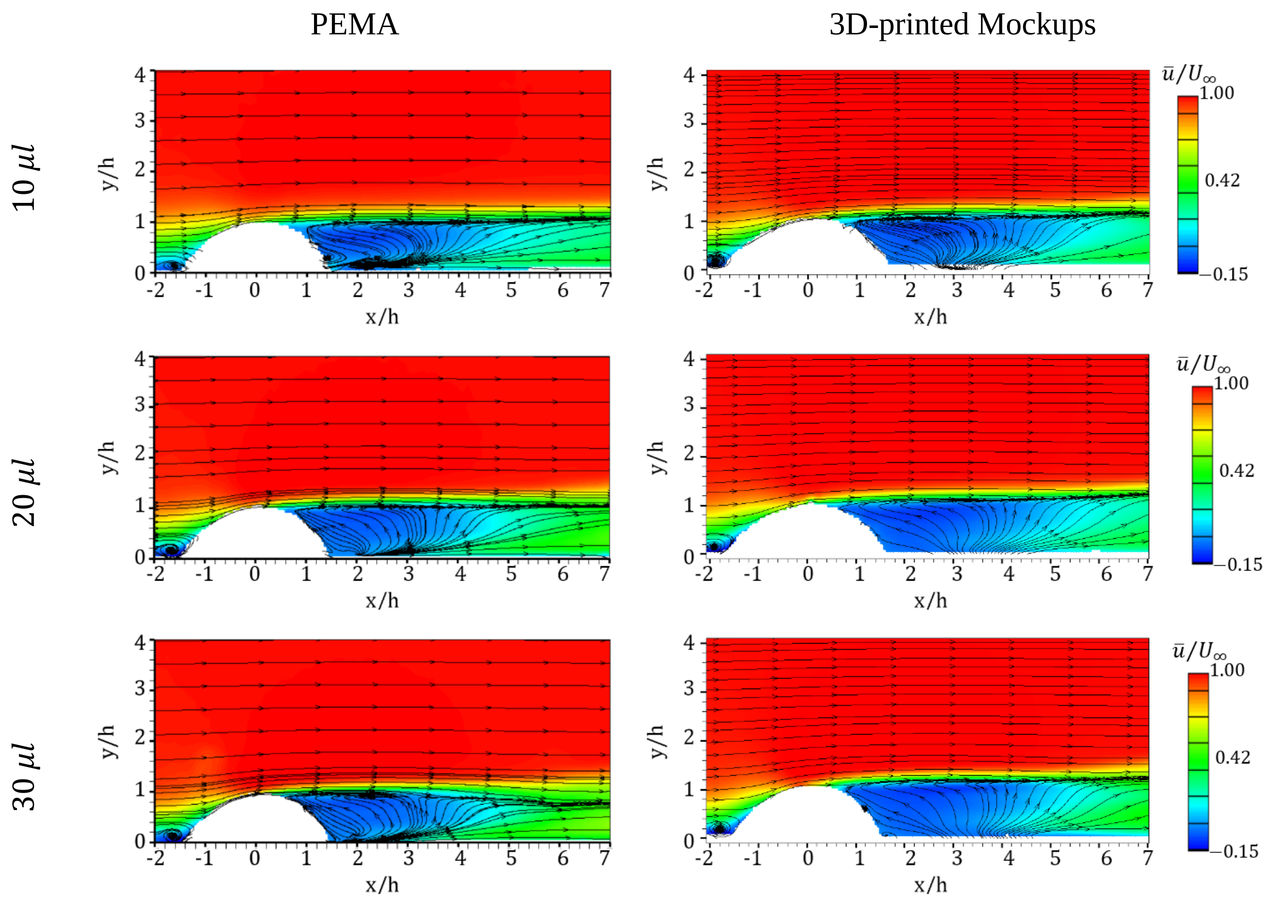

Figure 4-19. streamline patterns on x-velocity contours for droplets with different sizes on PEMA vs. their associated solid mockups. Free stream velocities for droplets on PEMA: 10 μl) 8.9 m/s, 20 μl) 8.3 m/s, 30 μl) 8.1 m/s.

The same contours for PMMA are shown in Figure 4-20. Like solid mockups for other wettabilities, the streamlines and normalized x-velocity for solid mockups of PMMA are similar to those of real droplets. Then, the oscillations of droplets do not play a role in changing the structure of air flow over sessile droplets.

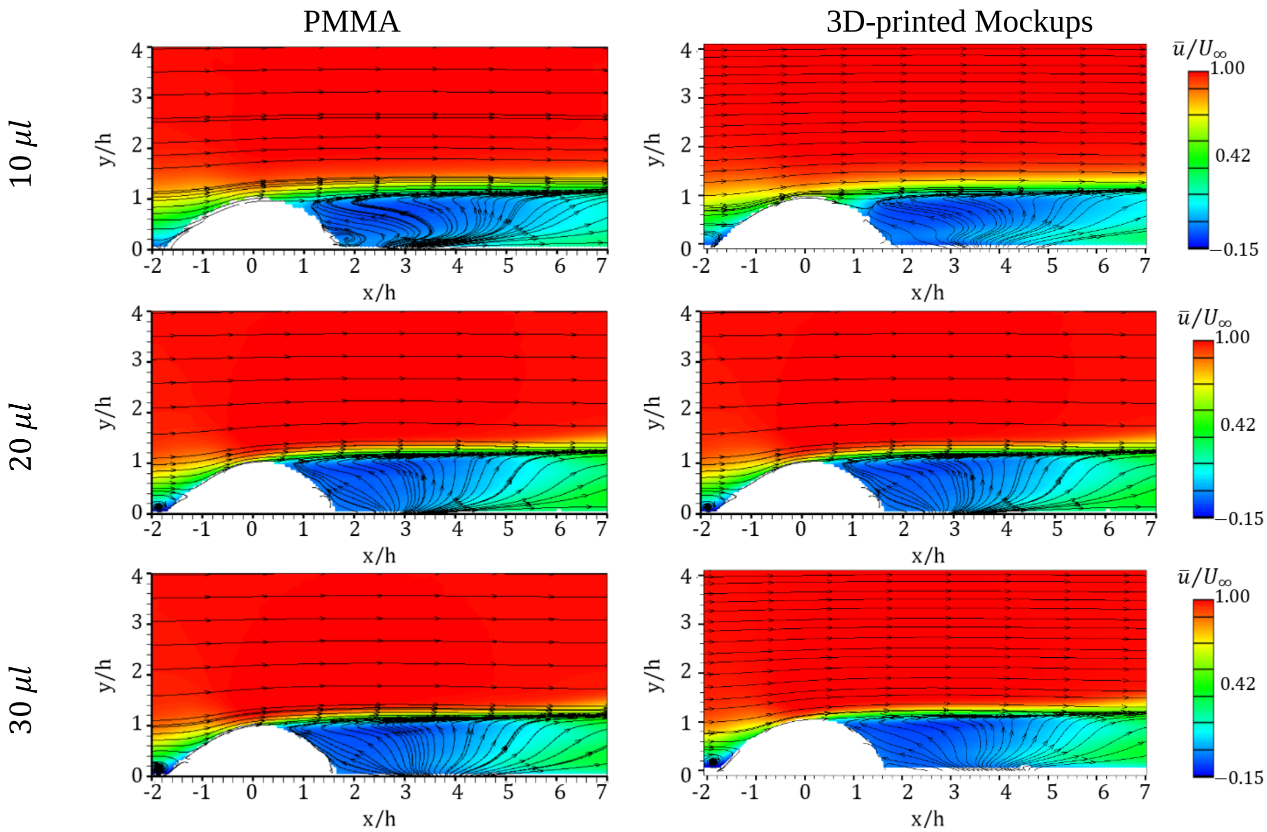

Figure 4-20. streamline patterns on x-velocity contours for droplets with different sizes on PMMA vs. their associated solid mockups. Free stream velocities for droplets on PMMA: 10 μl) 10.8 m/s, 20 μl) 9.9 m/s, 30 μl) 8.4 m/s

4.3.2 Recirculation length for air flow over solid mockups

The normalized recirculation length for air flow over sessile droplets with different sizes for surfaces of different wettability along with their solid mockups are shown in Figure 4-21-Figure 4-24. The error bars show a "± standard deviation" from the average values calculated out of three separate experiments for each case study. Looking at Figure 4-21-Figure 4-24 for droplets with different sizes on each surface wettability and their solid mockups, one sees that for all 12 cases, the normalized recirculation lengths of the solid mockups are close to the values for droplets. The droplets seem to make the recirculation length of the air flow downstream a little shorter than their solid representatives. That is due to the models' surface roughness. The solid mockups are made using a considerably precise 3D-printer, however, to make their surface as smooth as a droplet surface, is not completely possible at that scale even for a printer as precise as that. Thus, with the results of flow structure being notably similar for droplets and their mockups, one could define the effect of oscillation in flow structure the same as the effect of the roughness of the solid mockups surface in this study. In that conclusion, the surface of a droplet is considered as ideally smooth.

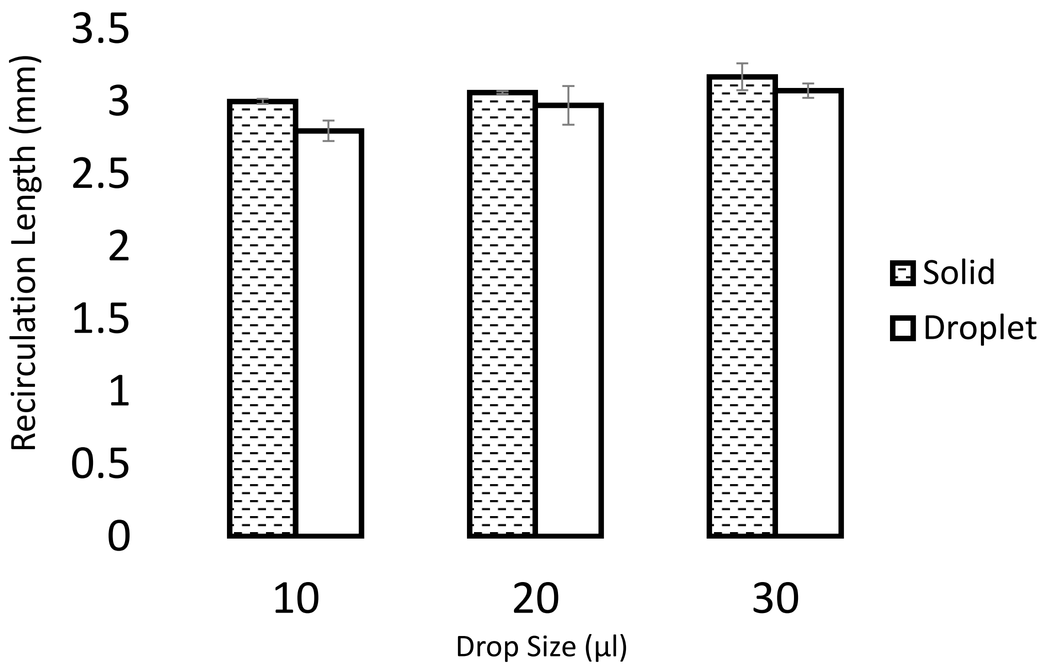

Figure 4-21. The normalized recirculation length for air airflow over sessile droplets placed on Teflon and their mockups. Free stream velocities for droplets on Teflon: 10 μl) 5.6 m/s, 20 μl) 4.8 m/s, 30 μl) 4.5 m/s.

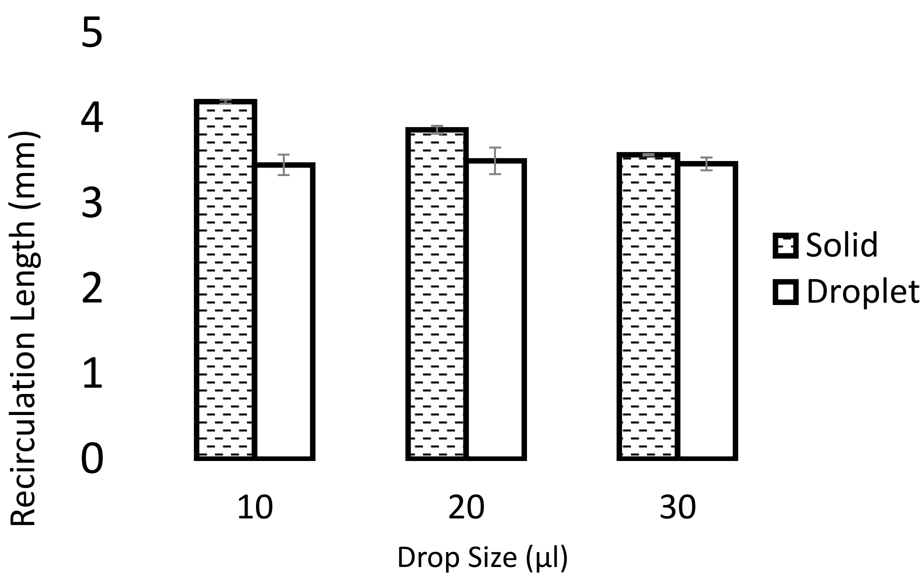

Figure 4-22. The normalized recirculation length for air airflow over sessile droplets placed on PS and their mockups. Free stream velocities for

droplets on PS: 10 μl) 8.5 m/s, 20 μl) 8.2 m/s, 30 μl) 6.6 m/s.

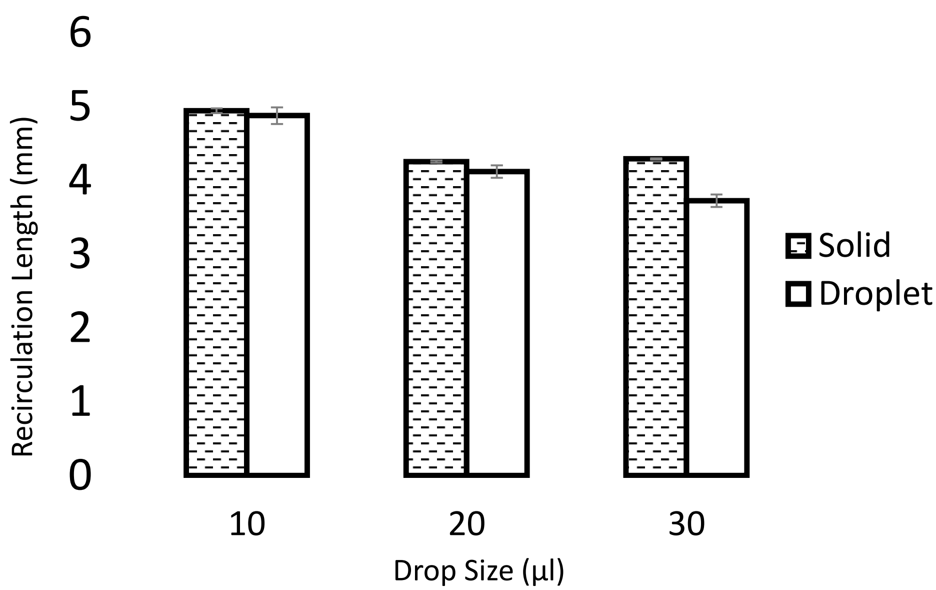

Figure 4-23. The normalized recirculation length for air airflow over sessile droplets placed on PEMA and their mockups. Free stream velocities for droplets on PEMA: 10 μl) 8.9 m/s, 20 μl) 8.3 m/s, 30 μl) 8.1 m/s

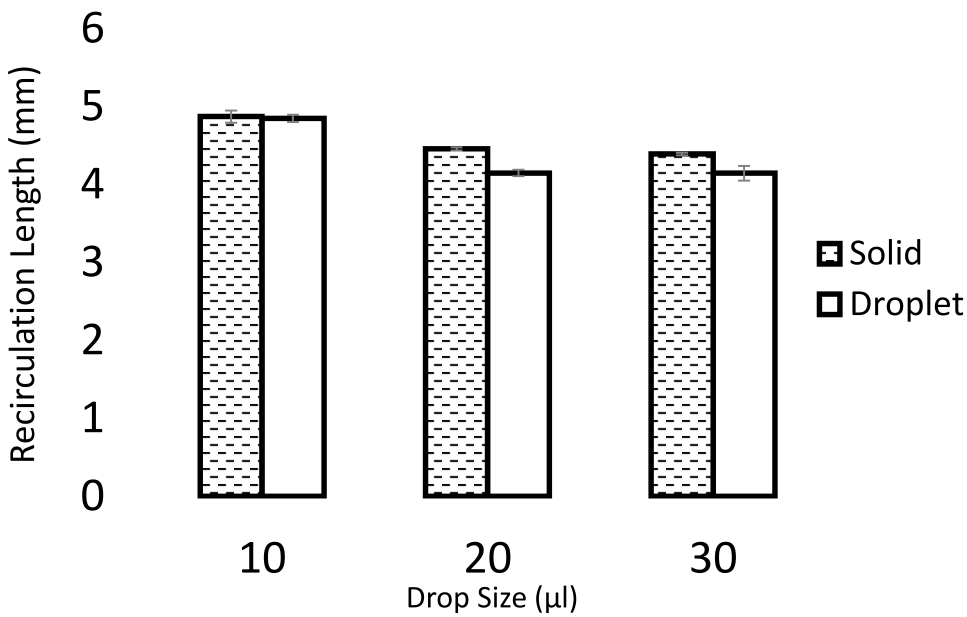

Figure 4-24. The normalized recirculation length for air airflow over sessile droplets placed on PMMA and their mockups. Free stream velocities for droplets on PMMA: 10 μl) 10.8 m/s, 20 μl) 9.9 m/s, 30 μl) 8.4 m/s

4.3.3 The effect of drop oscillations on the air flow structure

Based on the time averaged results for air flow over droplet mockups, the following conclusion could be made regarding the flow structure:

- The oscillations' effect in changing the structure of the flow is negligible.
- The effect of drop surface oscillations on defining the recirculation length is similar to the effect of solid mockups surface roughness on the flow.

4.4 The effect of wettability on pressure around a sessile droplet

4.4.1 Pressure Contour (PMMA - $30\ \mu l$)

Study of pressure field will allow one to understand the drag force hence the drive for shedding of a droplet. The drag force is caused by the pressure difference (upstream and downstream) and the skin friction drag. The skin friction drag is due to the shear stress exerted on the surface of the body (droplet). Skin drag relates to the velocity profile at the immediate vicinity of the drop surface and the fluid (air) viscosity. To analyze the form drag (the drag force caused by the pressure difference), one should obtain the pressure field out of the velocity fields given. The pressure distribution around the droplet (in the mid-plane) caused by the air flow is shown in Figure 4-25. The contour shows a high-pressure zone of about 10 Pa (gauge pressure relative to the pressure in the free stream) upstream of the droplet, and a low pressure zone (a gauge pressure of about -10 Pa) is located over the droplet. The low-pressure zone continues downstream of the droplet, but increases slightly such that a pressure of about -4 Pa is distributed on the downstream side of the droplet. This pressure difference of almost more than 14 Pa results in a drag force which is also proportional to the frontal area as well.

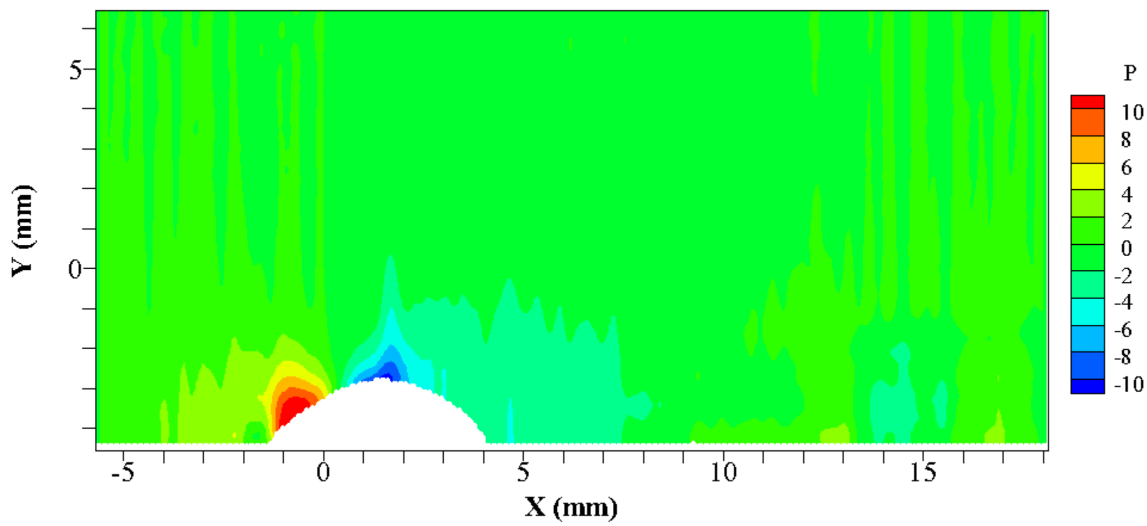

Figure 4-25. Pressure contour for flow over a sessile droplet (PMMA - 30 μl). U_∞=8.4 m/s

Pressure contours are informative in terms of pressure distribution around the droplets. However, to analyze and compare the drag force around the droplets more effectively it is yet better to analyze the drag coefficient contours for the considered study cases. The pressure coefficient contour for the air flow over a 30 μl droplet on a PMMA coated aluminum surface is shown in Figure 4-26. Figure 4-26 shows that the same distribution of the pressure is kept as Figure 4-25 but the values are normalized using the free stream velocity.

This shows the order of the pressure difference by which -while acted on the frontal area of the droplet- the droplet is deformed/depinned.

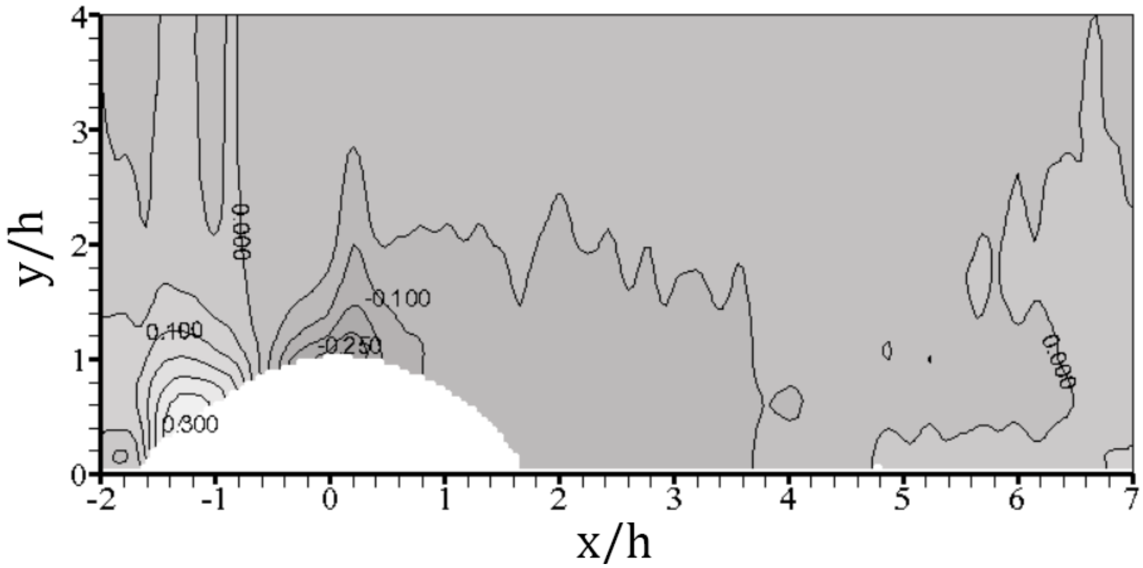

Figure 4-26. Pressure coefficient contour for flow over a sessile droplet (PMMA - 30 μl).

U_{∞}=8.4 m/s

4.4.2 Angle of Separation (PMMA - $30\ \mu l$)

Angle of separation is perhaps one of the most important characteristics of the flow over a body. This is because the angle of separation has a direct effect on the wake area and the drag force. Higher separation angles lead to less drag force and lower separation angles result in stronger drag forces. To calculate the angle of separation, one could use the fact that the separation happens when ${dp}/{dl_{surface}} > 0$. And to apply the principle in calculating the angle of separation one needs the pressure contours. The schematic of the procedure to find the angle of separation for the considered case (PMMA-30) is shown in Figure 4-27. The angle of separation for PMMA-30 is 98° in the midplane.

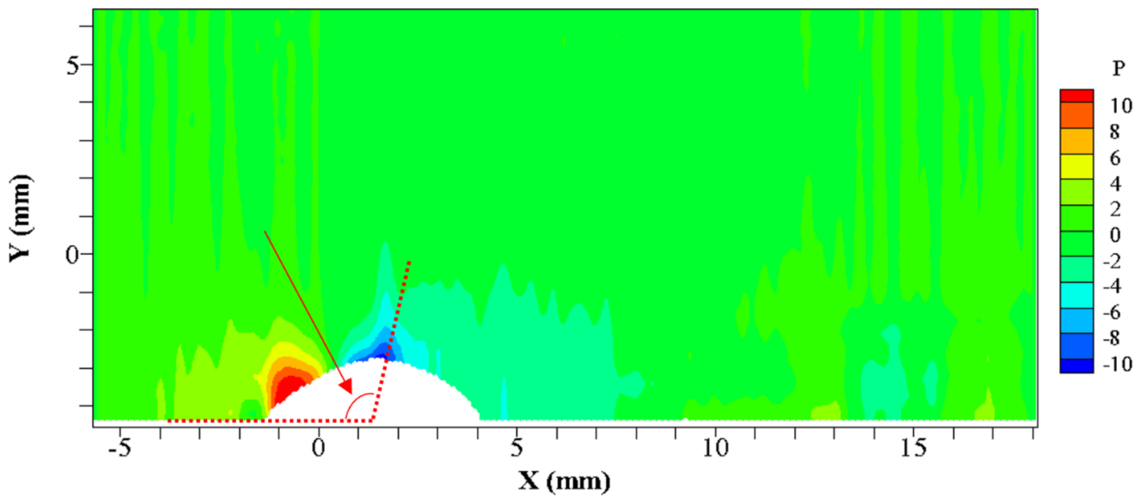

Figure 4-27. The angle of separation for the air flow over a 30 μl droplet on a PMMA coated Aluminum surface, in the midplane. U_{∞}=8.4 m/s

4.4.3 The effect of wettability on pressure

The pressure contour for air flow over a 30 μl droplet on PMMA was thoroughly explained in 4.4.1. To analyze and compare the coefficient of pressure for all the cases, their pressure coefficient contours are brought herewith in Figure 4-28.

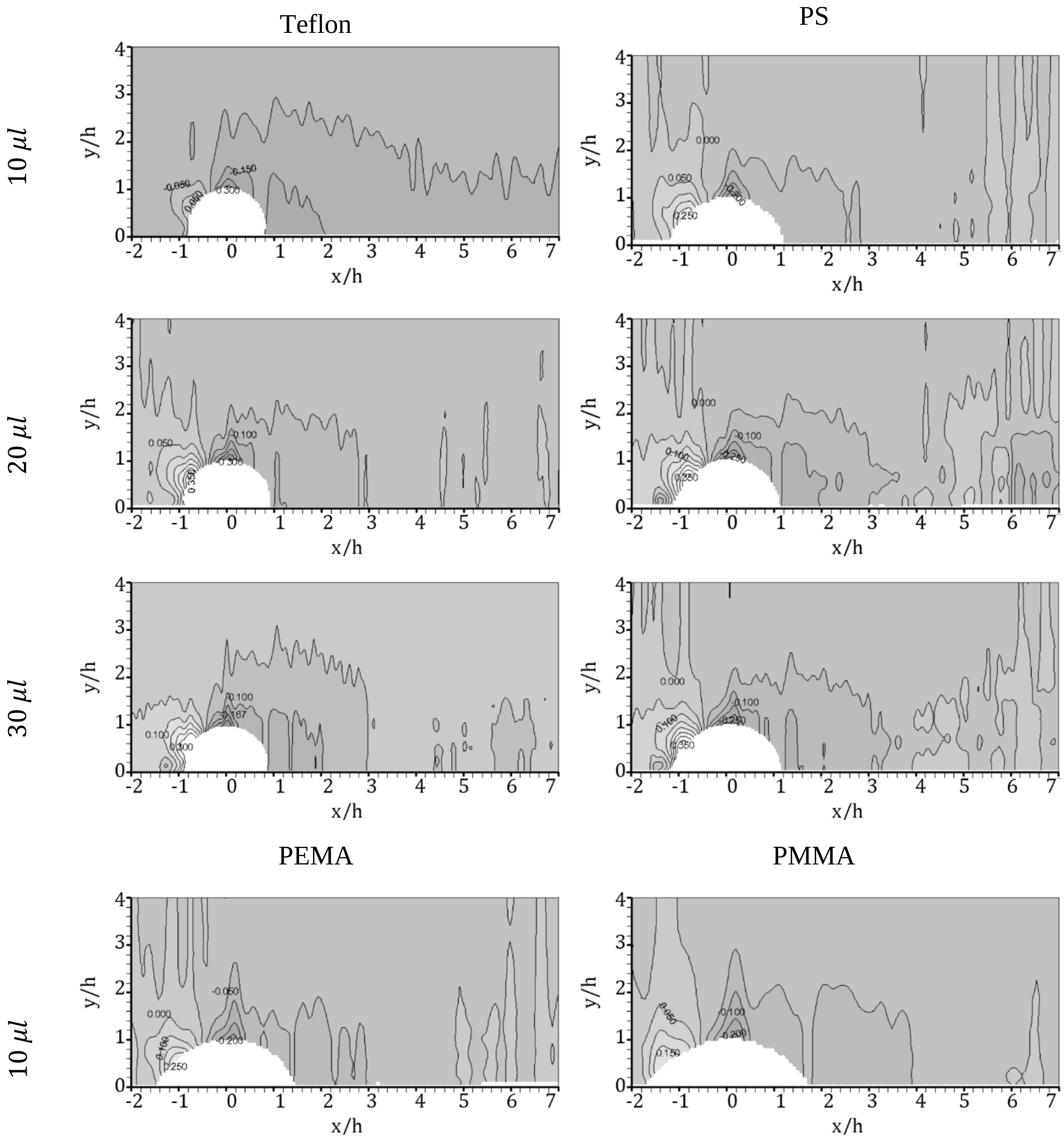

Continues next page…

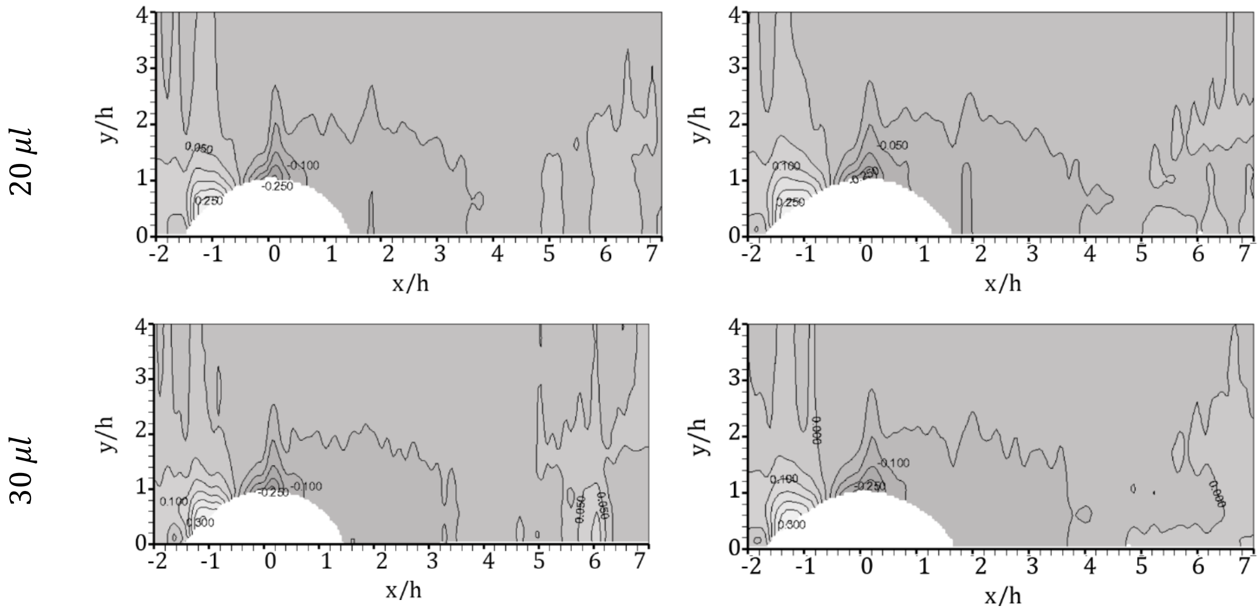

Figure 4-28. Coefficient of Pressure contours for different cases of study. Free stream velocities for droplets on Teflon: 10 µl) 5.6 m/s, 20 µl) 4.8 m/s, 30 µl) 4.5 m/s. Free stream velocities for droplets on PS: 10 µl) 8.5 m/s, 20 µl) 8.2 m/s, 30 µl) 6.6 m/s. Free stream velocities for droplets on PEMA: 10 µl) 8.9 m/s, 20 µl) 8.3 m/s, 30 µl) 8.1 m/s. Free stream velocities for droplets on PMMA: 10 µl) 10.8 m/s, 20 µl) 9.9 m/s, 30 µl) 8.4 m/s

Looking at the figures and the pressure coefficients around the droplet, it is seen that, for each droplet size, the pressure profiles and the coefficients around the droplet are quite close which would result in the drag coefficient of a droplet at these four surface wettabilities being in the same order. This also conforms to the findings of Milne's Ph.D. theis in which he reported the drag coefficients of water droplets on PMMA and Teflon to be quite close to each other using the recordings done by a floating element sensor [53]

4.4.4 The effect of wettability and drop size on angle of separation

The flow separation angles calculated using the pressure contours are shown in Table 4-1.

Table 4-1. Angle of Separation for all the cases

	$10\ \mu l$	**$20\ \mu l$**	**$30\ \mu l$**
Teflon	92°	94°	96°
PS	97°	96°	99°
PEMA	98°	97°	99°
PMMA	98°	98°	98°

Data in Table 4-1 shows very similar flow separation angle for all the cases. The values are somewhere between the values reported for spheres exposed to laminar (82°) and turbulent (120°) flow in literature. They are closer to the values reported for laminar flow (which is consistent with the Reynolds numbers in the current study) [54]. As such, the wettability and size do not have a significant effect on changing the flow separation angle at the verge of shedding.

4.4.5 The effect of wettability and drop size on pressure around a sessile droplet (conclusions)

Given the pressure contours, the velocity profiles and angle of separation around a sessile droplet, the following conclusions are made:

- Flow separation angle is similar (~97°) for droplets of different sizes on surfaces with different wettabilities.
- The order of magnitude for c_f is the same for all the cases due to velocity profile and separation angle similarity.

- The order of magnitude of c_p is the same for all drop sizes on different surface wettabilities.
- With c_p and c_f being similar for droplets at the verge of shedding (regardless of surface wettability and drop size): the drag force by which the droplets are depinned changes only with AU_∞^2 (in which A is the frontal area of the droplet and U_∞ is the free stream velocity of the air when the droplet is at the verge of shedding).

4.5 The effect of surface wettability on turbulence

To understand the status of turbulence around a sessile droplet, first the results for (PMMA - $30\ \mu l$) is shown. Then, the effect of wettability on changing the turbulence of flow around a sessile droplet is provided for all cases.

Understanding turbulence characteristics is important as, for instance, the average drag force may be below the value required to depin the droplet, but the instantaneous drag force could lead to shedding of droplet. Then, it is important to identify the level of turbulence in such studies. This way one realizes how deviated the instantaneous values could be from the time-averaged values.

4.5.1 Turbulence statistics (PMMA - $30\ \mu l$)

The following parameters are used to study the flow turbulence passing over a sessile droplet:

1) normalized u'$_{rms}$ (u'_{rms}/U_∞) contours
2) normalized u'$_{rms}$ (u'_{rms}/U_∞) profiles
3) normalized Reynolds Stress ($\overline{u'v'}/U_\infty^2$) contours

4.5.2 Normalized u'_{rms} ($^{u'_{rms}}/_{U_\infty}$) contour (PMMA - 30 μl)

The normalized u'_{rms} (=$^{u'_{rms}}/_{U_\infty}$) contour for a 30 μl droplet on PMMA is shown in Figure 4-29; the free stream shows the lowest u'_{rms}values which are close to zero. This indicates that the time-averaged x-velocity field is not much different than the instantaneous values in the main flow. The recirculation zone (which is shown in section 4.1.4), also shows quite low u'_{rms} values implying a low turbulence level. The shear layer shows a medium level of u'_{rms}. The $^{u'_{rms}}/_{U_\infty}$value in that area is almost 0.05 suggesting that the instantaneous x-velocity values could be 5% of U_∞ different than the time averaged values in the shear layer. The $^{u'_{rms}}/_{U_\infty}$values in the area that is below $^{y}/_{h} = 1$ (below the shear layer) and after the recirculation zone are also in the middle range. On top of this area, which is downstream the shear layer, the highest values for $^{u'_{rms}}/_{U_\infty}$is seen. This happens due to the vortex shedding, and higher levels of $^{u'_{rms}}/_{U_\infty}$corresponds to higher level of turbulence that is caused by the droplet. The quite low turbulence around the droplet indicates that the instantaneous values around the droplet should not be much different than their average values. High turbulence downstream of the droplet however suggests that -if other droplets are placed downstream- the droplets placed downstream would face a highly turbulent flow. This could lead to significant variations in instantaneous properties of the flow compared to averaged values for those droplets placed downstream of the first droplet.

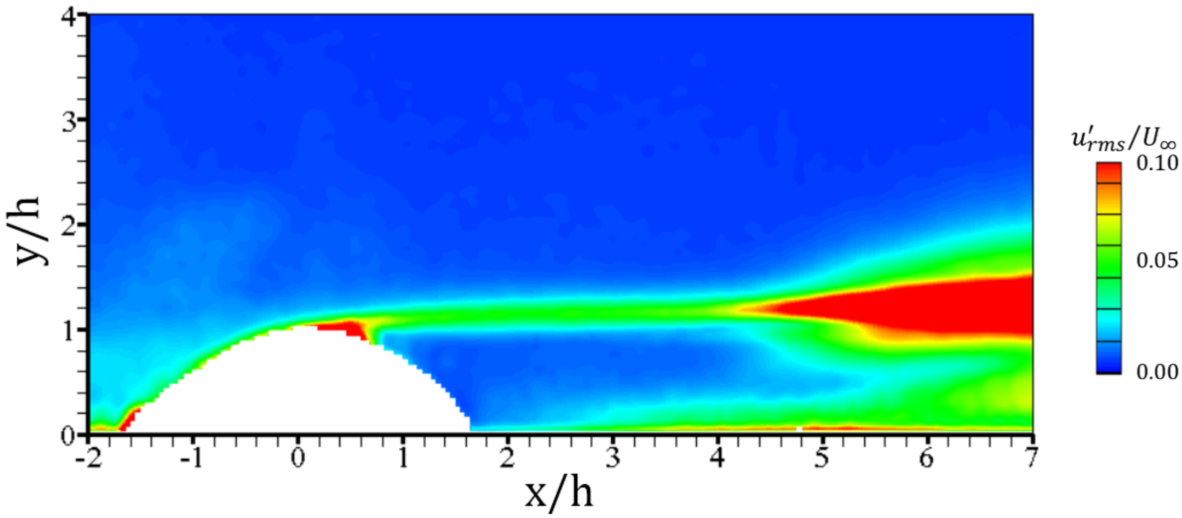

Figure 4-29. The normalized u'_{rms} (u'_{rms}/U_∞) contour for a 30 μl droplet on PMMA. U_∞=8.4 m/s

4.5.3 Normalized u'_{rms} profiles (PMMA - 30 μl)

To quantifiably analyze the differences between the u'_{rms}/U_∞ values for different cases, profiles at upstream, over and downstream of the droplet are examined. The spacing for the profiles are the same as those used in x-velocity profiles (e.g. Figure 4-3).

4.5.4 Normalized Reynolds Stress contour

In the current study, the order of y-velocity was found to be much less than the x-velocities. However, to identify the level of turbulence as accurate as possible (and the fact that the rms values for y-velocity could be as significant as the values for x-velocity), one needs to assess the Reynolds stress values to analyze the turbulence intensity. The normalized Reynolds stress ($\overline{u'v'}/U_\infty^2$) contour for a 30 μl droplet on PMMA is shown in Figure 4-30. Analogous to the u'_{rms}/U_∞, high Reynolds stress values exist where the vortices are shed (after the recirculation zone, close to

$^{y}/_{h} = 1$). This indicates that if a droplet is placed downstream of this droplet, the second droplet would be exposed to a rather turbulent flow. That would lead to significant deviations of instantaneous values from the averaged values for the second droplet. The other areas show normalized Reynolds stress values close to zero. As the normalized Reynolds stress around the droplet is insignificant, the instantaneous drag coefficient for droplet does not differ from the averaged value considerably.

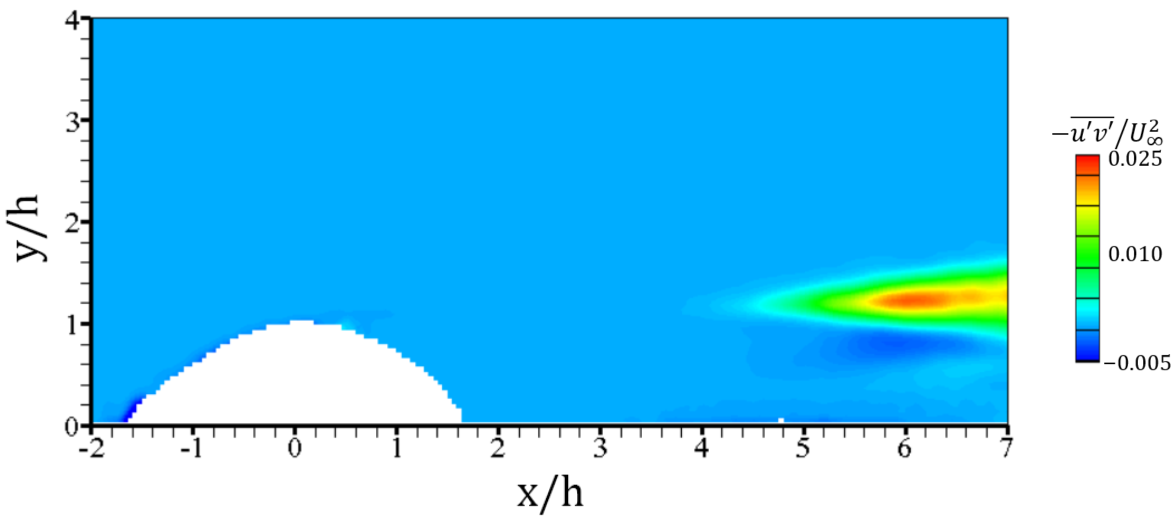

Figure 4-30. The normalized Reynolds Stress ($^{\overline{u'v'}}/_{U_\infty^2}$) contour for a 30 μl droplet on PMMA. U_∞=8.4 m/s

4.5.5 Turbulence statistics (all the cases)

The results here are presented in the same order as those in section 4.5.1, i.e., the effect of wettability is analyzed first using the $^{u'_{rms}}/_{U_\infty}$ contours. Then, the $^{u'_{rms}}/_{U_\infty}$ profiles are used to make a more detailed and precise comparisons to realize the effect of wettability on $^{u'_{rms}}/_{U_\infty}$ (as a measure of turbulence). The normalized Reynolds stress contours are also provided to reinforce the conclusions made through ${u'_{rms}}/{U_\infty}$ values. Finally, the maximum ${u'_{rms}}/{U_\infty}$ values for each case are provided to justify and strengthen the conclusions made through ${u'_{rms}}/{U_\infty}$ contours, and profiles and Reynolds stress contours. Plus, to showcase the effect of surface wettability concisely.

4.5.6 The effect of wettability on normalized u'_{rms} contours

The normalized u'_{rms} (${u'_{rms}}/{U_\infty}$) contours are provided herewith to comprehend the effect of wettability on turbulence intensity (normalized u'_{rms} in this case). The ${u'_{rms}}/{U_\infty}$ contours for droplets of different sizes on different wettabilities are illustrated in Figure 4-31. The figure suggests that for 10 µl the induced turbulence intensity is the greatest when the surface is coated with PS and PMMA and the lowest when the substrates are coated with Teflon and PEMA. This means that small droplets sitting on PMMA and PS would induce high turbulence to the flow. In case of a tandem arrangement for a system of droplets, those droplets placed downstream would be exposed to a rather turbulent flow. That could lead to instantaneous drag coefficient of those droplets to deviate significantly from the average drag coefficient (which should be systematically studied for a system of droplets).

As suggested by the contours, the turbulence level of the air flow over larger droplets (20 µl and 30 µl) are similar to each other. For subtle differences, however, shall be done using the profiles, etc., but, as far as the contours indicate, the normalized u'_{rms} levels are not different in a way that is noticeable.

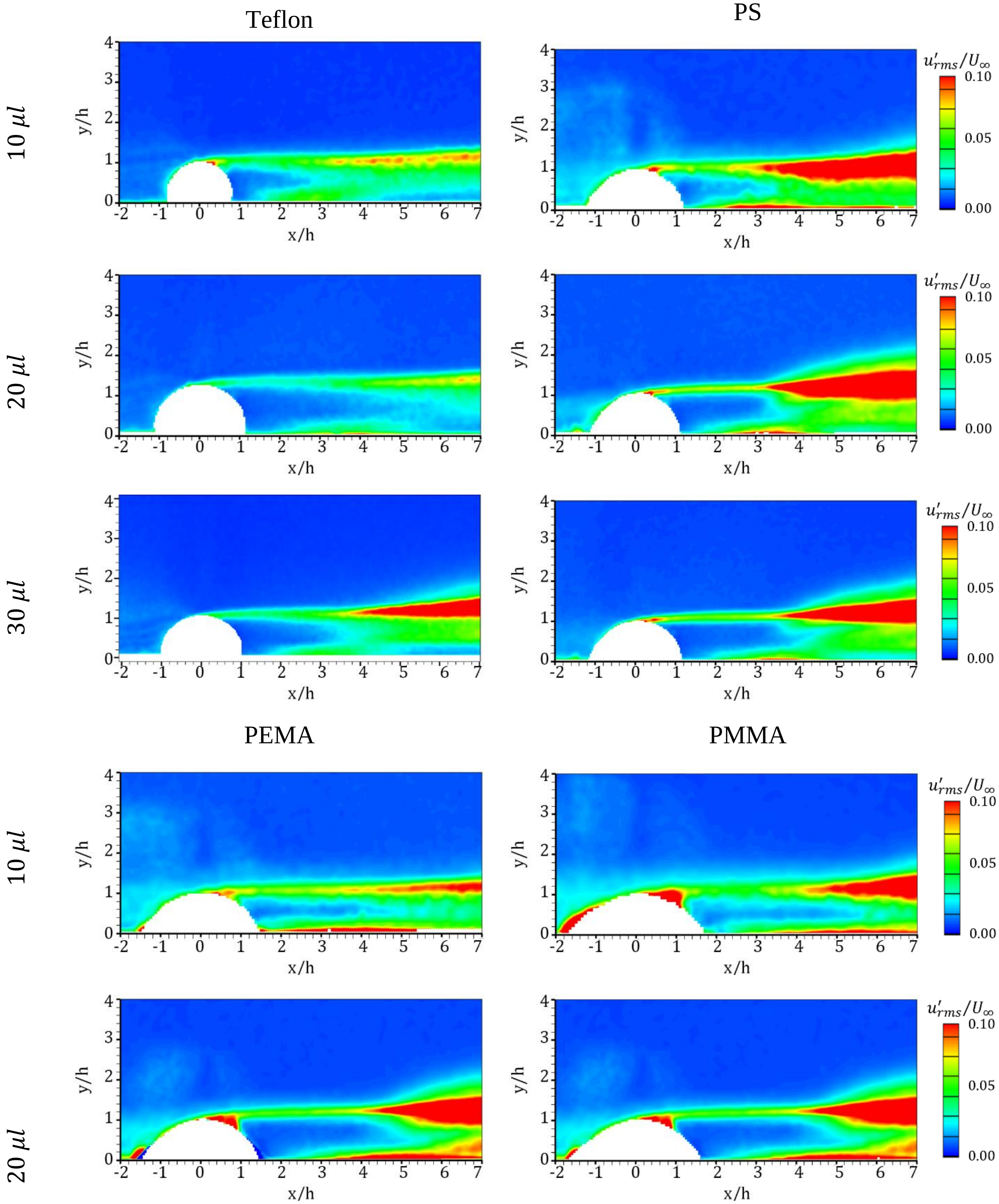

Continues next page…

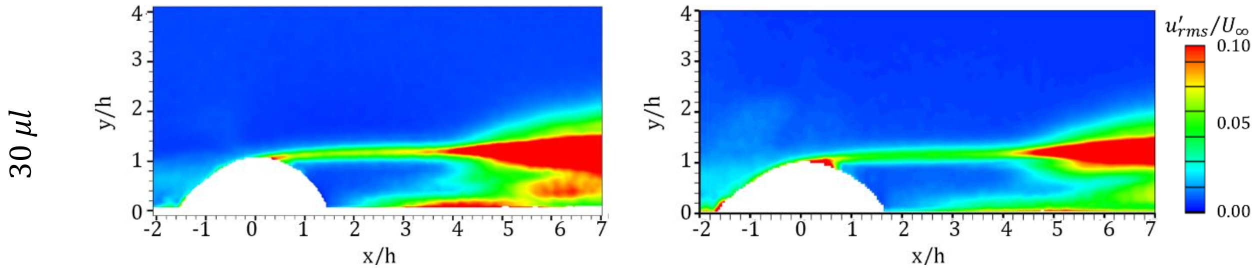

Figure 4-31. normalized u'_{rms} (u'_{rms}/U_∞) contours for air flow over sessile droplets. Free stream velocities for droplets on Teflon: 10 μl) 5.6 m/s, 20 μl) 4.8 m/s, 30 μl) 4.5 m/s. Free stream velocities for droplets on PS: 10 μl) 8.5 m/s, 20 μl) 8.2 m/s, 30 μl) 6.6 m/s. Free stream velocities for droplets on PEMA: 10 μl) 8.9 m/s, 20 μl) 8.3 m/s, 30 μl) 8.1 m/s. Free stream velocities for droplets on PMMA: 10 μl) 10.8 m/s, 20 μl) 9.9 m/s, 30 μl) 8.4 m/s

This is an indication that for larger droplets (20 μl and 30 μl) the turbulence does not change with the surface wettability. It is concluded then, that for large droplets, normalized turbulence (u'_{rms}) is similar. Then for a system of droplets with tandem arrangement, the effect of surface wettability in inducing turbulence to the flow for droplets sitting downstream the same. Thus, the deviation of instantaneous values (e.g., drag coefficient) from average values (for droplets sitting downstream in a tandem arrangement) should be similar for large droplets regardless of the surface wettability.

Figure 4-31 shows that the u'_{rms}/U_∞ around droplet profiles are insignificant. This means that instantaneous drag coefficient for all droplet sizes are similar to average drag coefficients regardless of drop size and surface wettability.

4.5.7 The effect of wettability on normalized u'_{rms} upstream and on the droplet (profiles)

To further confirm the earlier observations, the normalized u'$_{rms}$ profiles are provided hereby in Figure 4-32 and Figure 4-33. Figure 4-32 shows normalized u'$_{rms}$ (= u'_{rms}/U_{∞}) profiles upstream of a droplet -with different sizes of 10-30 μl- on surfaces with different wettabilities. The turbulence levels are insignificant for all the cases and similar.

a)

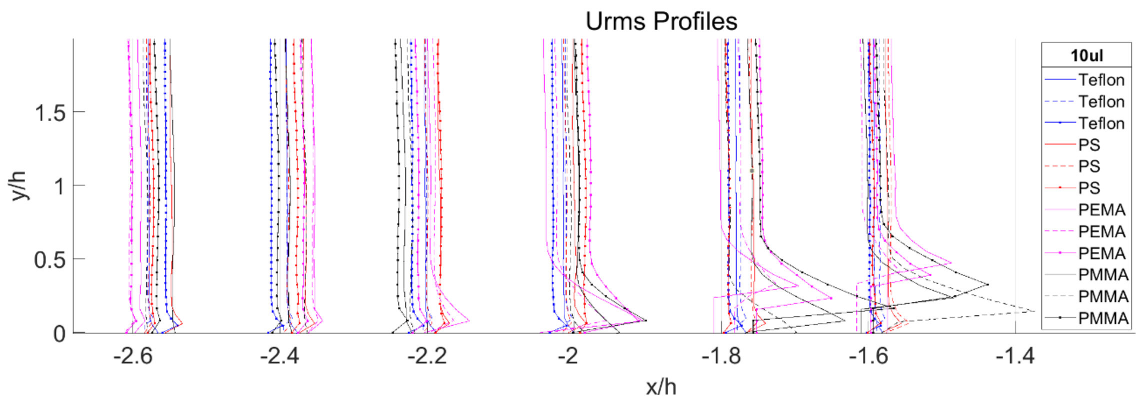

b)

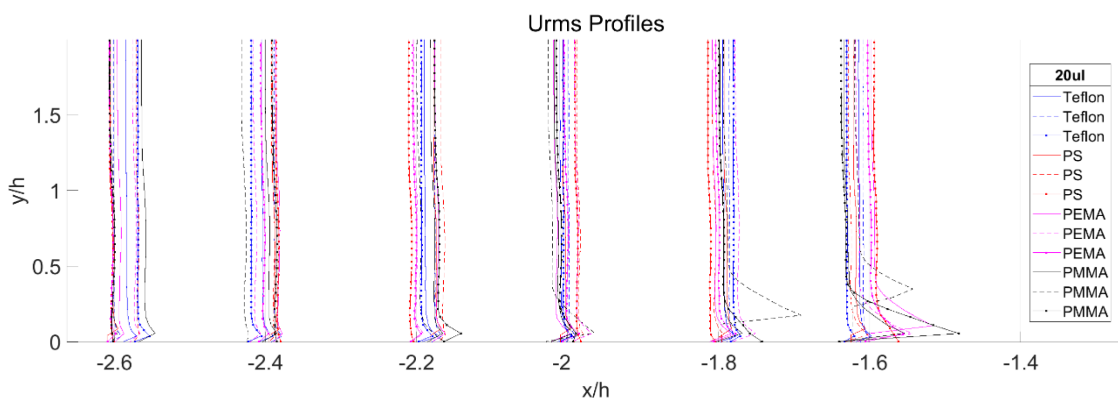

Continues next page…

c)

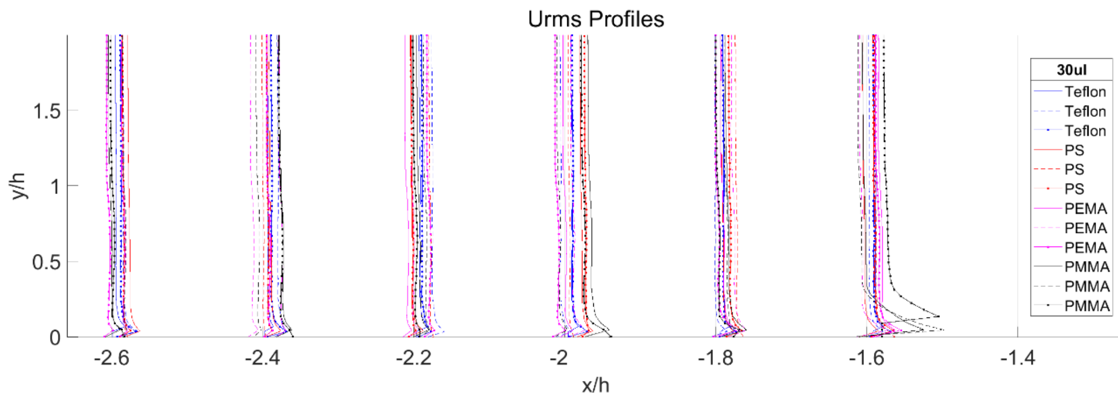

Figure 4-32. normalized u'$_{rms}$ ($^{u'_{rms}}/_{U_\infty}$) profiles upstream the droplet a) for 10 μl droplets b) for 20 μl droplets. c) for 30 μl droplets. Free stream velocities for droplets on Teflon: 10 μl) 5.6 m/s, 20 μl) 4.8 m/s, 30 μl) 4.5 m/s. Free stream velocities for droplets on PS: 10 μl) 8.5 m/s, 20 μl) 8.2 m/s, 30 μl) 6.6 m/s. Free stream velocities for droplets on PEMA: 10 μl) 8.9 m/s, 20 μl) 8.3 m/s, 30 μl) 8.1 m/s. Free stream velocities for droplets on PMMA: 10 μl) 10.8 m/s, 20 μl) 9.9 m/s, 30 μl) 8.4 m/s

A few bumps seen in Figure 4-32 at $^x/_h = -1.8$ and $^x/_h = -1.6$, are due to the small vortex created behind the droplet. Figure 4-32 also indicates that even those bumps corresponding to the small vortex behind the droplet, do not differ significantly for surfaces with different wettabilities.

a)

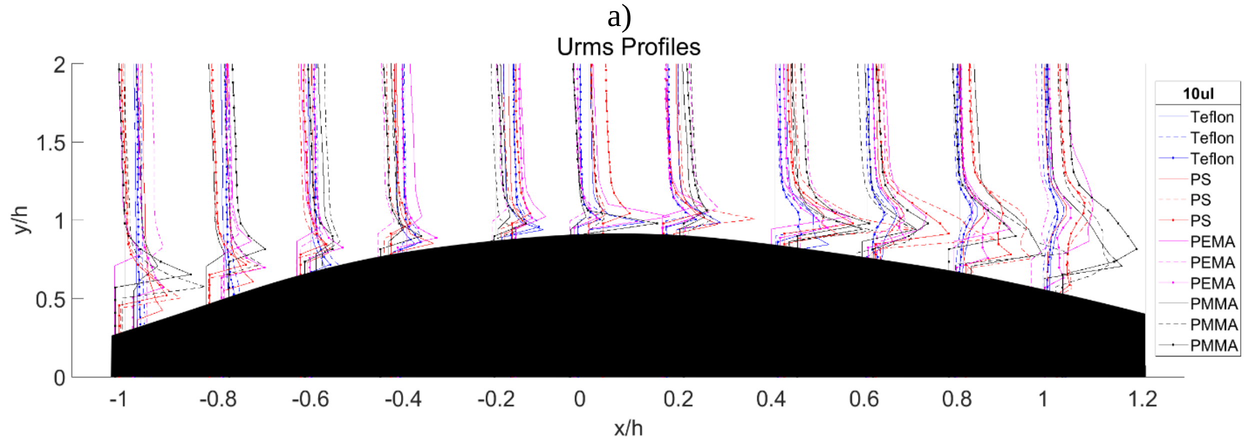

Continues next page…

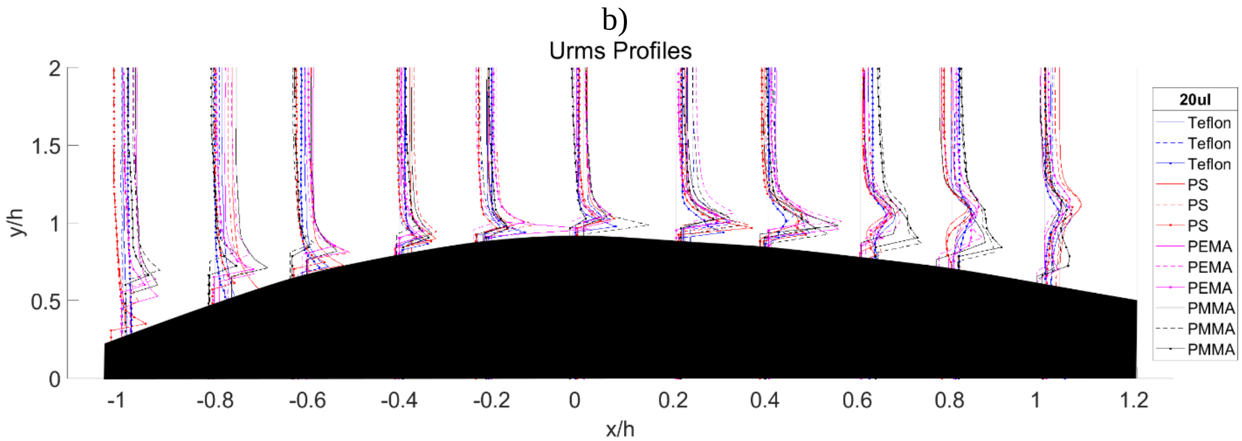

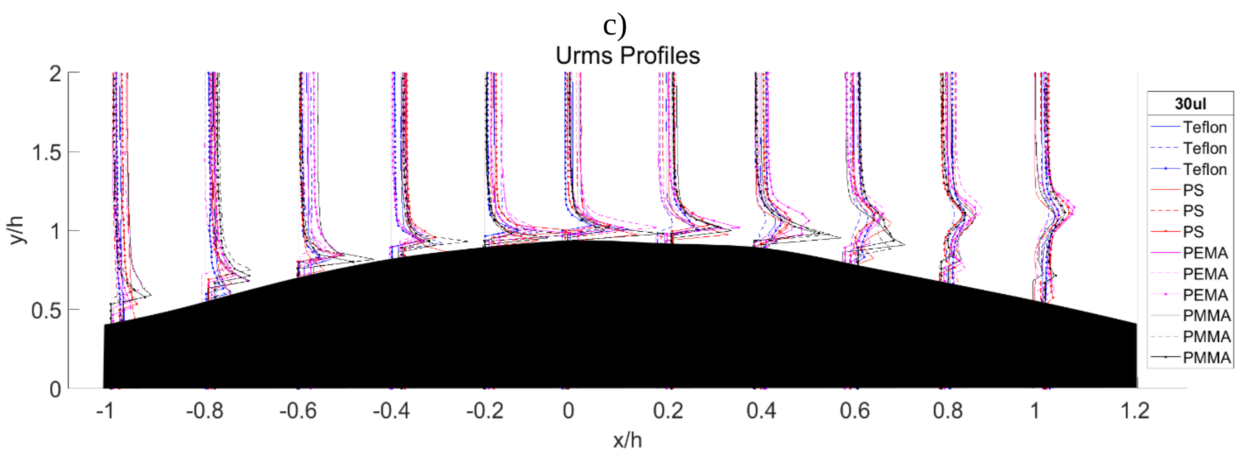

Figure 4-33. normalized u'$_{rms}$ (u'_{rms}/U_∞) profiles on the droplet a) for 10 μl droplets b) for 20 μl droplets. c) for 30 μl droplets. Free stream velocities for droplets on Teflon: 10 μl) 5.6 m/s, 20 μl) 4.8 m/s, 30 μl) 4.5 m/s. Free stream velocities for droplets on PS: 10 μl) 8.5 m/s, 20 μl) 8.2 m/s, 30 μl) 6.6 m/s. Free stream velocities for droplets on PEMA: 10 μl) 8.9 m/s, 20 μl) 8.3 m/s, 30 μl) 8.1 m/s. Free stream velocities for droplets on PMMA: 10 μl) 10.8 m/s, 20 μl) 9.9 m/s, 30 μl) 8.4 m/s

Figure 4-33 shows normalized u'$_{rms}$ ($= \mathrm{u'_{rms}}/\mathrm{U_\infty}$) profiles on a droplet -with different size of 10-30 μl- on surfaces with different wettabilities. The profiles in Figure 4-33 indicate that the turbulence level on the surface of the droplet has some bumps; in the free stream flow (e.g., $y/h \geq 1.1$ for $x/h = 0$) , the turbulence level drops down to ~0. The peaks seen over the surface of the droplets, seem not to be changing with the surface wettability irrespective of the drop size. It is strongly concluded then, that the turbulence level (normalized u'_{rms}) upstream and on the droplet do not change with surface wettability. The insignificant turbulence on the droplet indicates that instantaneous coefficient of friction should be similar to average coefficient of friction for all drop sizes and surface wettabilities.

4.5.8 The effect of wettability on normalized u'_{rms} downstream the droplet (profiles)

Having analyzed the effect of surface wettability on the normalized u'_{rms} upstream and on the droplet, the effect is also to be assessed for downstream the droplet. Figure 4-34 illustrates the normalized u'_{rms} profiles- for all drop sizes- on surfaces with different wettabilities. Concluded earlier, for smaller droplets ($10\,\mu l$) those droplets on PS and PMMA lead to higher levels of u'_{rms}/U_∞ downstream of the droplet (see section 4.5.6). The larger droplets induced the same level of normalized u'_{rms} downstream of the droplet regardless of the surface wettability.

Figure 4-34a further highlights the conclusion made for normalized turbulence levels for small droplets. The profiles in Figure 4-34a clearly indicate that the turbulence level of airflow downstream of the droplets on PS and PMMA are more than the other wettabilities. This reinforces the conclusion that for two small tandem droplets, the second droplet on PS and PMMA are exposed to a more turbulent flow. That could lead to higher instantaneous drag coefficients (compared to their average values) for small droplets placed downstream of a droplet on PS and PMMA.

Figure 4-34b and Figure 4-34c also, support the idea that as the droplets get larger ($20\,\mu l$ and $30\,\mu l$) the wettability of the surface do not change the normalized u'_{rms} values for the airflow downstream of a droplet. This reinforces the conclusion that for two large tandem droplets, the droplet that is placed downstream, experiences the same level of turbulence regardless of the surface wettability.

a)

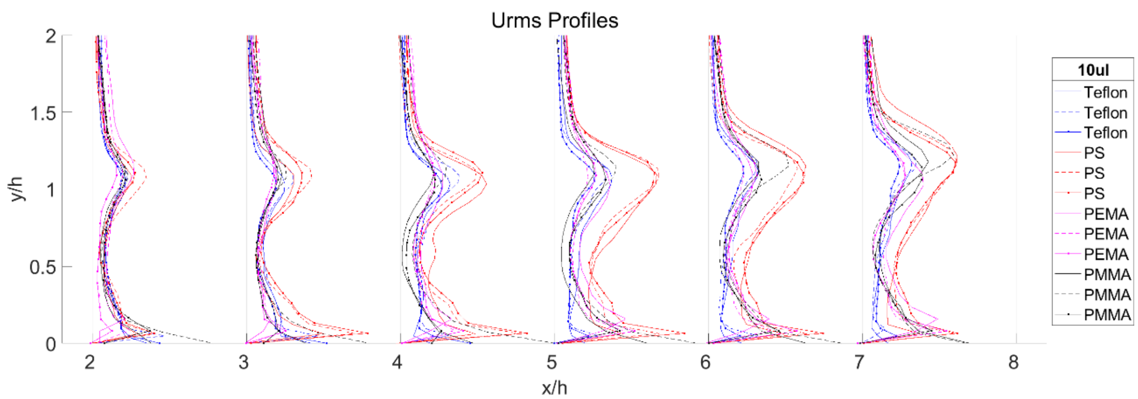

b)

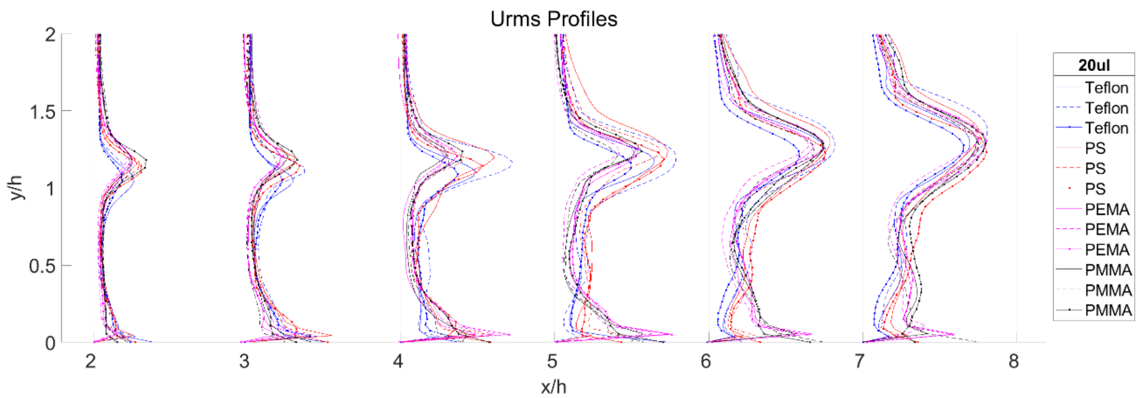

Continues next page…

c)

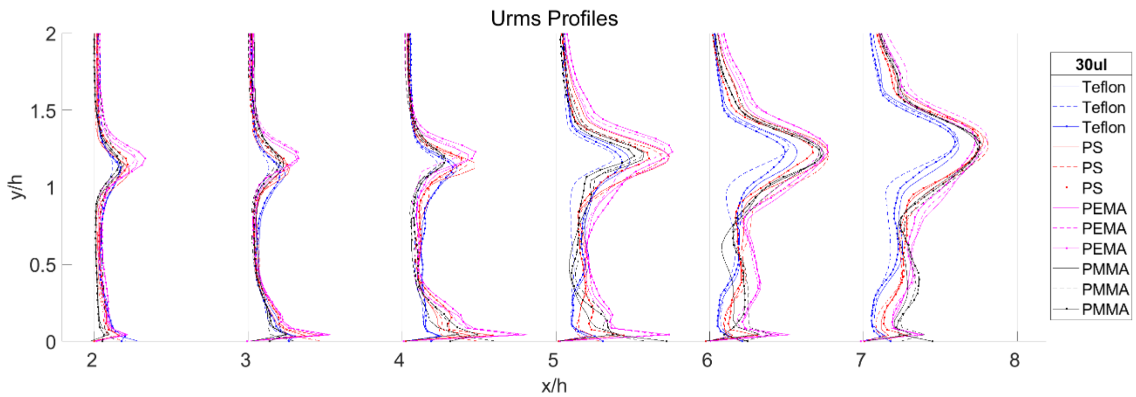

Figure 4-34. normalized u'$_{rms}$ ($^{u'_{rms}}/_{U_\infty}$) profiles downstream the droplet a) for 10 μl droplets b) for 20 μl droplets. c) for 30 μl droplets. Free stream velocities for droplets on Teflon: 10 μl) 5.6 m/s, 20 μl) 4.8 m/s, 30 μl) 4.5 m/s. Free stream velocities for droplets on PS: 10 μl) 8.5 m/s, 20 μl) 8.2 m/s, 30 μl) 6.6 m/s. Free stream velocities for droplets on PEMA: 10 μl) 8.9 m/s, 20 μl) 8.3 m/s, 30 μl) 8.1 m/s. Free stream velocities for droplets on PMMA: 10 μl) 10.8 m/s, 20 μl) 9.9 m/s, 30 μl) 8.4 m/s

4.5.9 The effect of wettability on normalized u'_{rms} (using maximum normalized u'_{rms} values)

Figure 4-35 shows the maximum normalized u'$_{rms}$ values for air flow over sessile droplets. The error bars show a "± standard deviation" from the average values calculated out of three separate experiments for each case study. For 10 μl droplets, it is seen that the maximum u'$_{rms}$ values - which happens in the shear layer and after the recirculation zone- for PS and PMMA are almost twice in the field (compared to Teflon and PEMA).

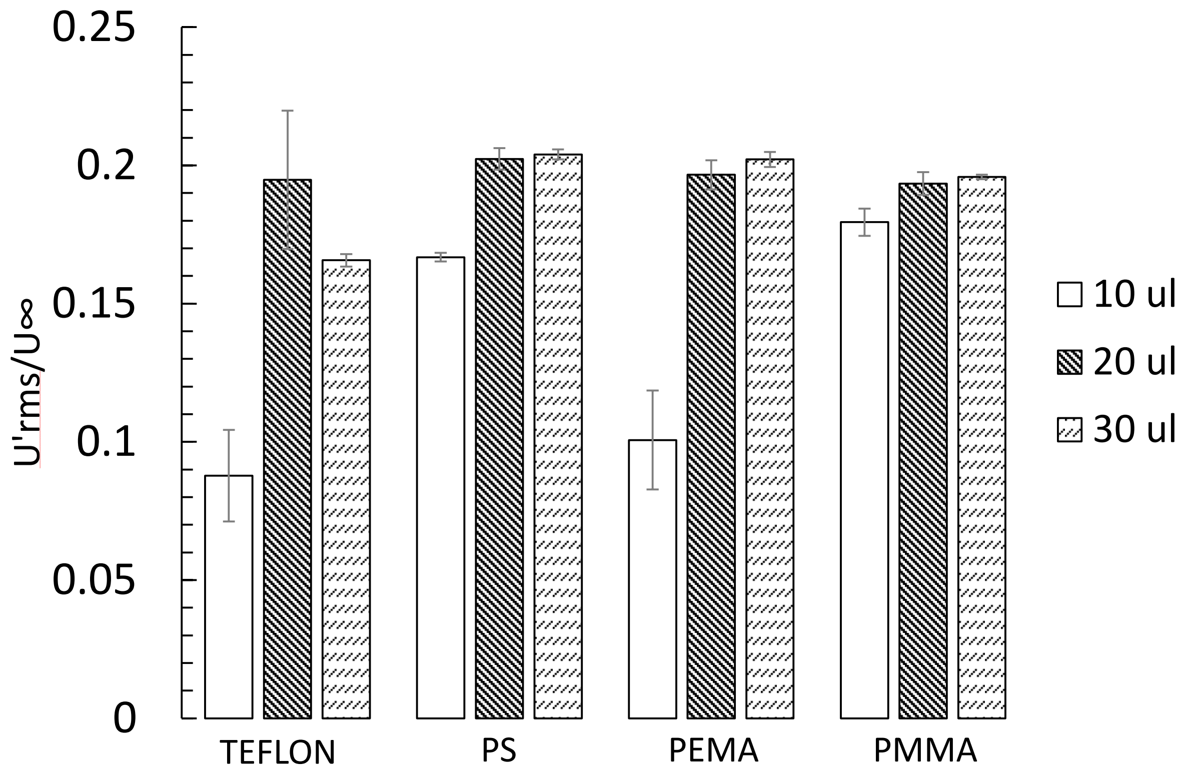

Figure 4-35. Maximum normalized u'_{rms} $\left({u'_{rms}}/{U_\infty}\right)$ values for air flow over 10 μl dorplets. Free stream velocities for droplets on Teflon: 10 μl) 5.6 m/s, 20 μl) 4.8 m/s, 30 μl) 4.5 m/s. Free stream velocities for droplets on PS: 10 μl) 8.5 m/s, 20 μl) 8.2 m/s, 30 μl) 6.6 m/s. Free stream velocities for droplets on PEMA: 10 μl) 8.9 m/s, 20 μl) 8.3 m/s, 30 μl) 8.1 m/s. Free stream velocities for droplets on PMMA: 10 μl) 10.8 m/s, 20 μl) 9.9 m/s, 30 μl) 8.4 m/s

For 20 μl and 30 μl droplets, the earlier conclusion is further reinforced that the normalized u'_{rms} values for larger droplets, do not change with the wettability of the surface.

Given the above results one can state that:

- For small droplets the wettability of the surface can make a noticeable difference in the turbulence of the air flow downstream of a droplet. Small droplets (10 μl) sitting on PS and PMMA, lead to maximum normalized u'_{rms} values that are twice those for that of PEMA and Teflon.

- For two small tandem droplets, those droplets sitting downstream of a droplet on PS and PMMA, experience higher turbulence compared to those on Teflon and PEMA.
- For larger droplets ($20\,\mu l$ and $30\,\mu l$), the wettability of the surface does not make significant differences in the normalized u'_{rms} values in the air flow field.
- For two large tandem droplets, the droplets that are sitting downstream of a droplet experience similar turbulence in the shearing flow, regardless of the surface wettability.

4.5.10 The effect of wettability on turbulence statistics (conclusions)

Given the data provided on the effect of wettability on turbulence intensity, the following conclusions are made:

- For the air flow over small sessile droplets, turbulence is the highest when the surface is coated with PMMA and PS.
- For the air flow over large sessile droplets, turbulence intensity does not change considerably with surface wettability.
- For all droplets the instantaneous drag coefficients are similar to their average values as the turbulence around the droplet profile is insignificant.

4.6 The effect of drop size on turbulence

4.6.1 The effect of drop size on normalized u'_{rms} upstream and on the droplet (profiles)

Figure 4-36 shows the normalized u'$_{rms}$ profiles for air flow upstream the droplets for different droplet sizes on each surface wettability. Just as seen earlier for the effect of wettability on normalized u'$_{rms}$ for air flow upstream the droplets, the droplet size does not change the normalized u'$_{rms}$ levels upstream the droplet.

a)

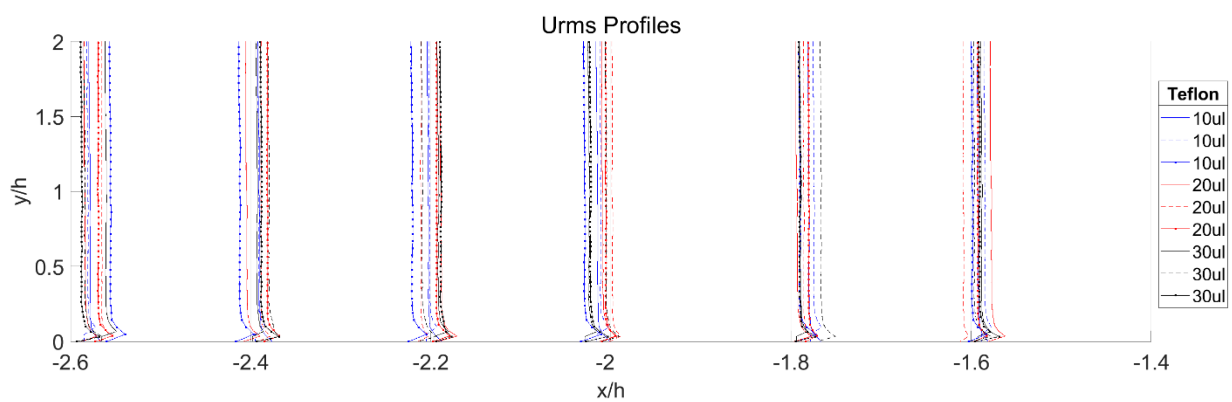

b)

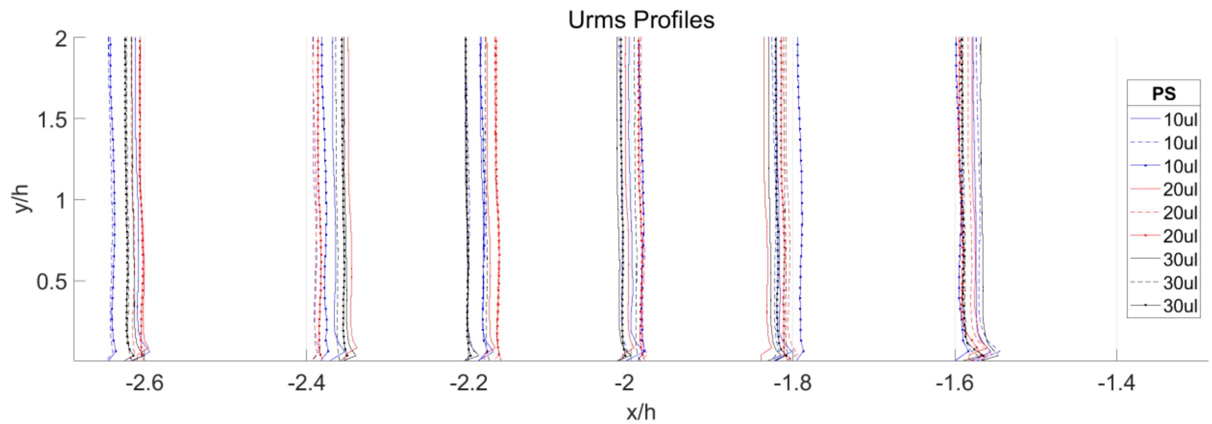

Continues next page…

c)

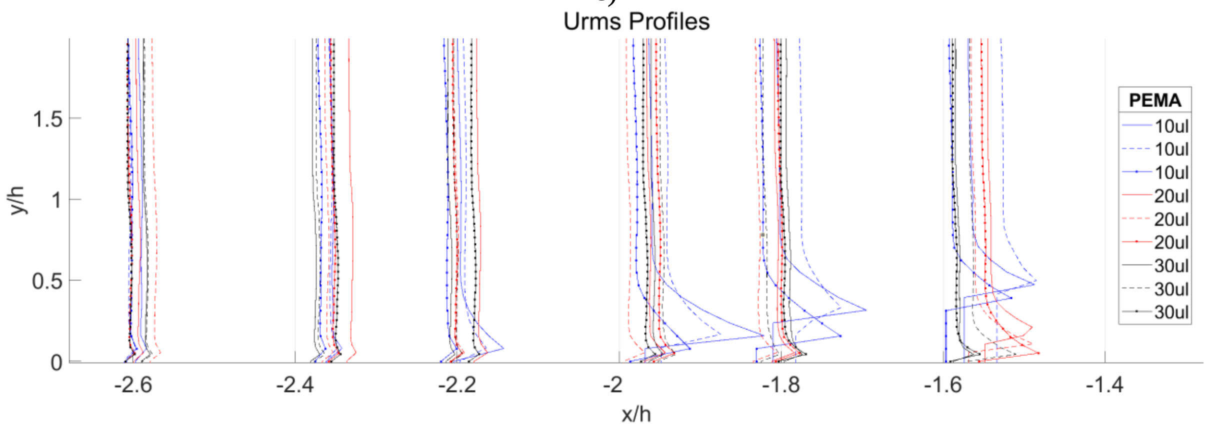

d)

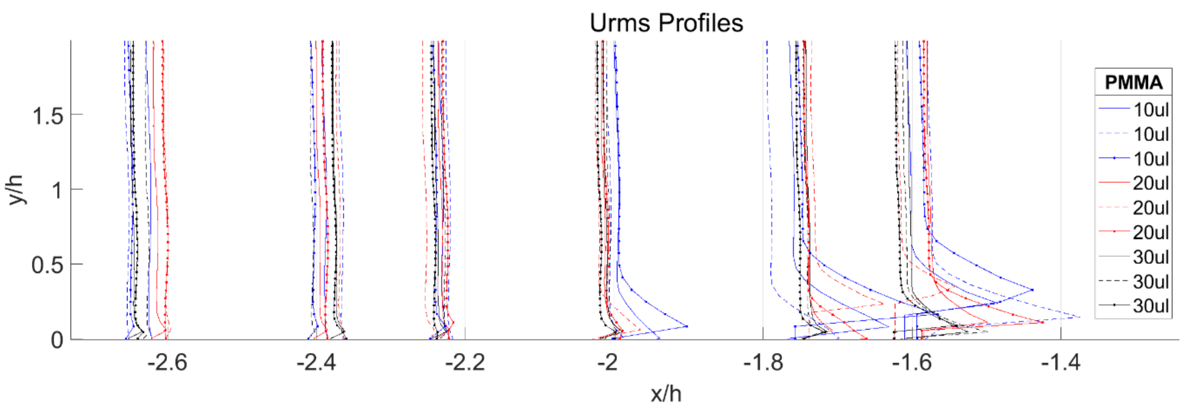

Figure 4-36. normalized u'$_{\text{rms}}$ ($^{u'_{rms}}/_{U_\infty}$) profiles upstream a droplet placed on a) Teflon. b) PS. c) PEMA. d) PMMA. Free stream velocities for droplets on Teflon: 10 μl) 5.6 m/s, 20 μl) 4.8 m/s, 30 μl) 4.5 m/s. Free stream velocities for droplets on PS: 10 μl) 8.5 m/s, 20 μl) 8.2 m/s, 30 μl) 6.6 m/s. Free stream velocities for droplets on PEMA: 10 μl) 8.9 m/s, 20 μl) 8.3 m/s, 30 μl) 8.1 m/s. Free stream velocities for droplets on PMMA: 10 μl) 10.8 m/s, 20 μl) 9.9 m/s, 30 μl) 8.4 m/s

a)

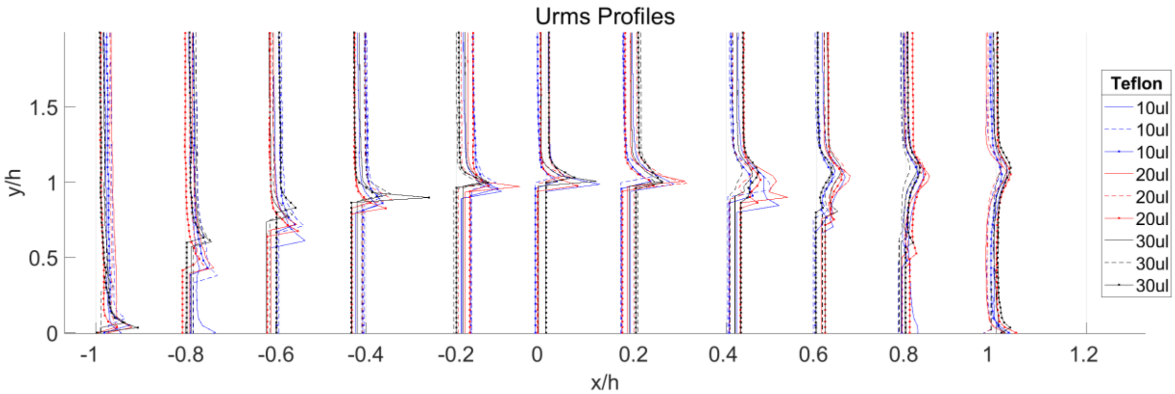

b)

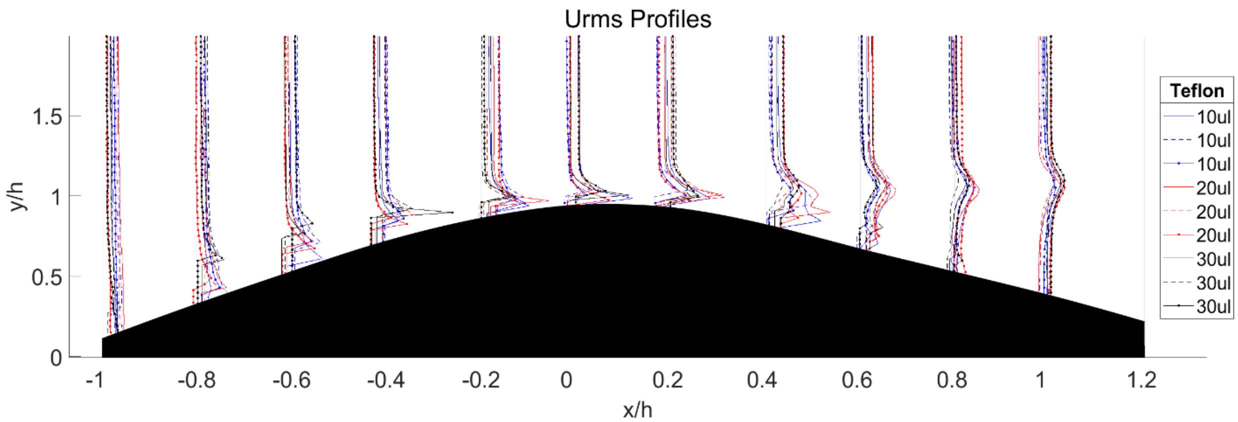

c)

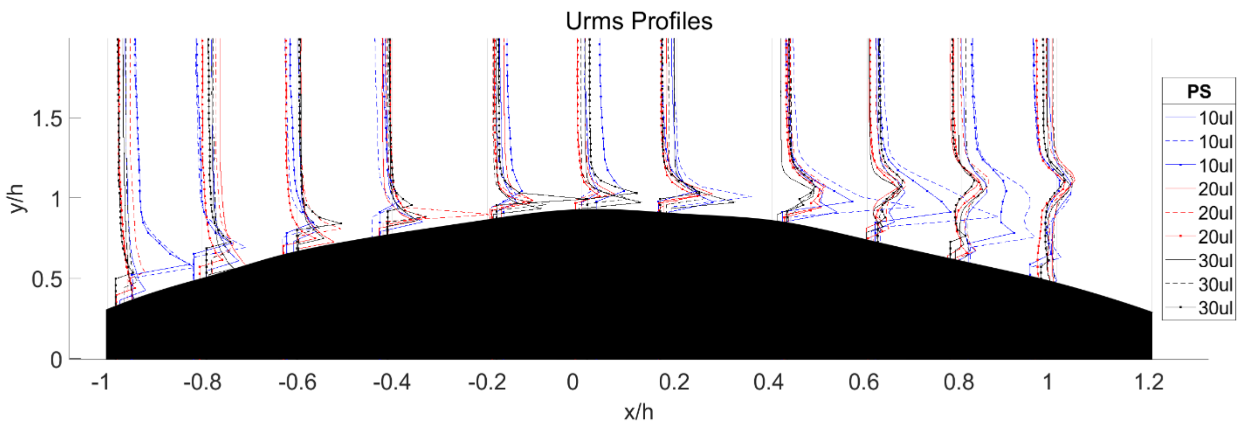

Continues the next page…

d)

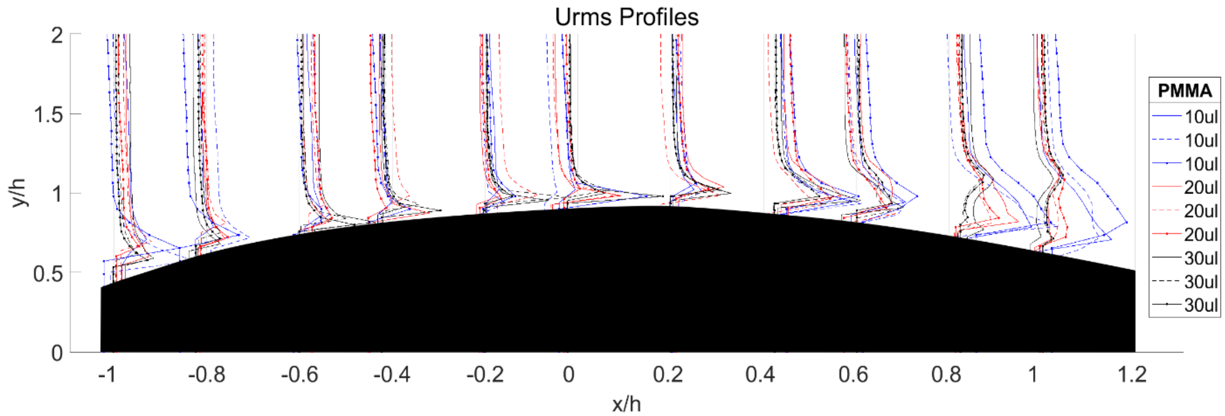

Figure 4-37. normalized u'$_{rms}$ ($^{u'_{rms}}/_{U_\infty}$) profiles on a droplet placed on a) Teflon. b) PS. c) PEMA. d) PMMA. Free stream velocities for droplets on Teflon: 10 μl) 5.6 m/s, 20 μl) 4.8 m/s, 30 μl) 4.5 m/s. Free stream velocities for droplets on PS: 10 μl) 8.5 m/s, 20 μl) 8.2 m/s, 30 μl) 6.6 m/s. Free stream velocities for droplets on PEMA: 10 μl) 8.9 m/s, 20 μl) 8.3 m/s, 30 μl) 8.1 m/s. Free stream velocities for droplets on PMMA: 10 μl) 10.8 m/s, 20 μl) 9.9 m/s, 30 μl) 8.4 m/s

Figure 4-37 illustrates the normalized u'$_{rms}$ profiles on the droplets with different sizes for each surface wettability. Assessing most of the locations, the profiles indicate that the droplet size does not change the normalized u'$_{rms}$ values near the drop surface. This means that instantaneous coefficient of friction is similar to their average values regardless of the drop size.

4.6.2 The effect of drop size on normalized u'_{rms} downstream the droplet (profiles)

The normalized u'$_{rms}$ profiles for air flow downstream of a sessile droplet with different sizes are shown in Figure 4-38 for each surface wettability. Figure 4-38 indicates that for all wettabilities, the larger droplets (20 μl and 30 μl) induce higher levels of turbulence (normalized u'$_{rms}$) downstream the flow.

This means that for a tandem arrangement of droplets, if droplets are larger, those droplets placed downstream are exposed to a more turbulent flow.

a)

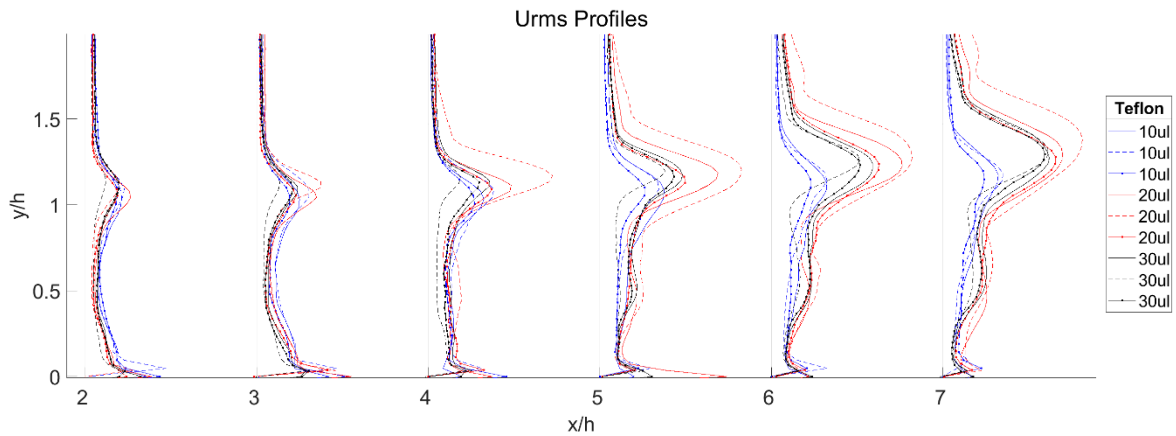

b)

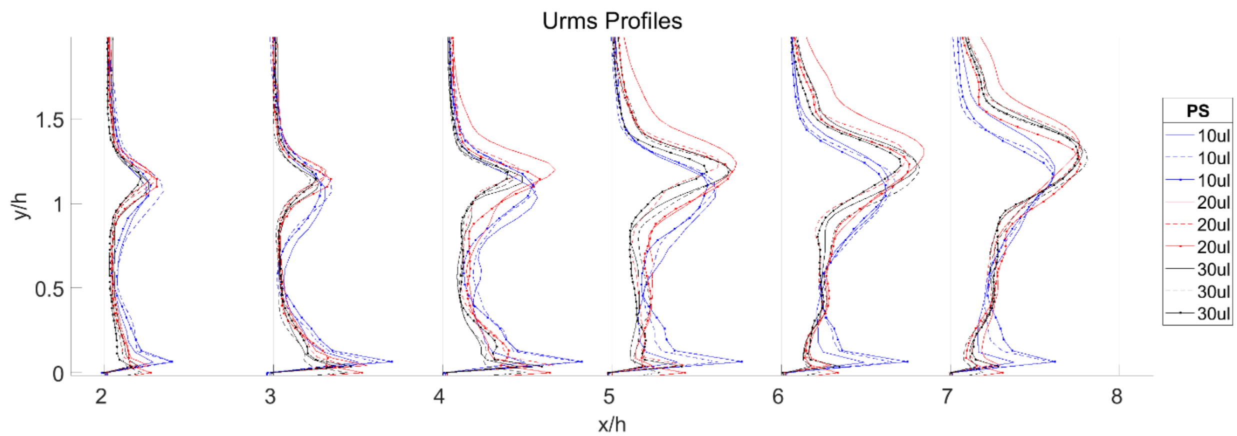

c)

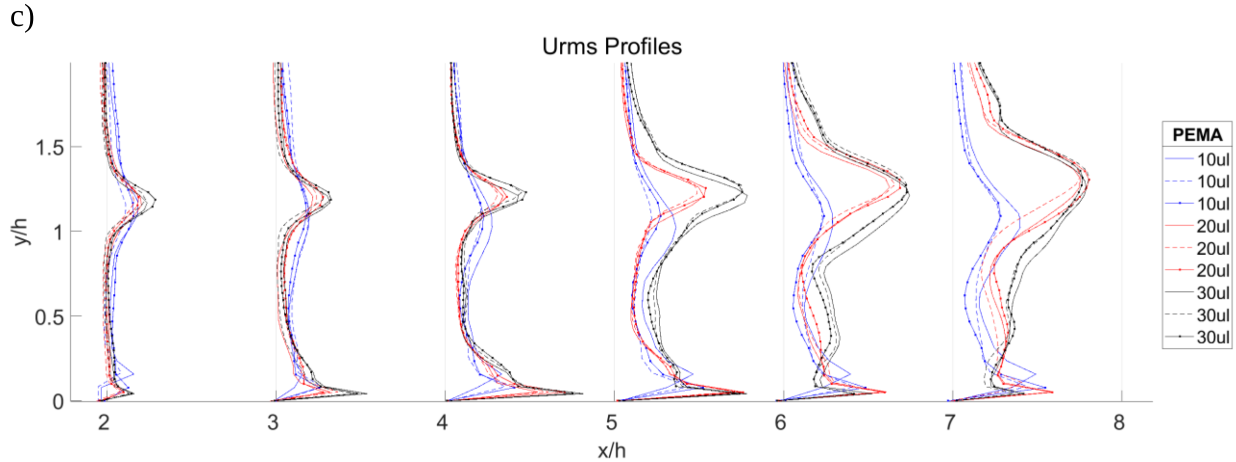

Continues the next page…

d)

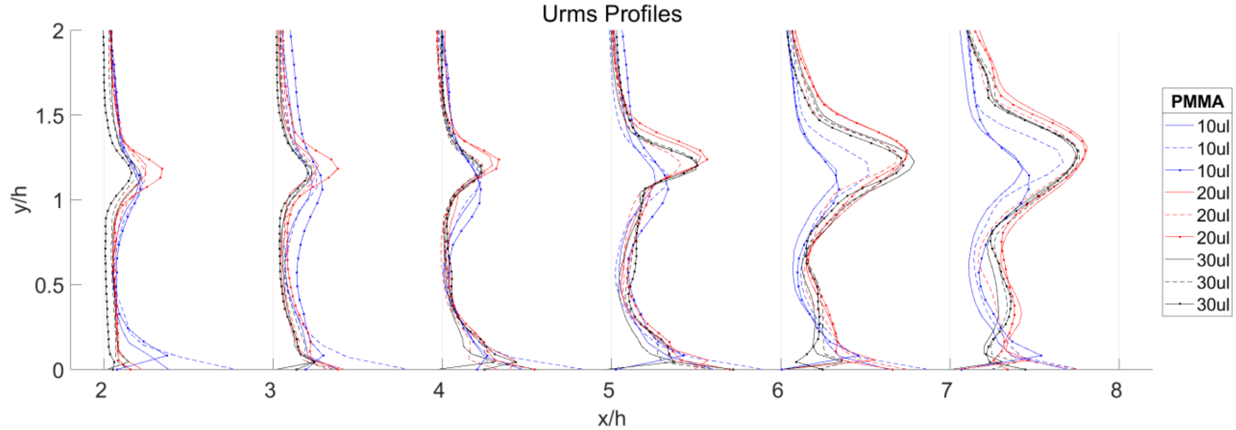

Figure 4-38. normalized u'$_{rms}$ (u'_{rms}/U_∞) profiles downstream a droplet placed on a) Teflon. b) PS. c) PEMA. d) PMMA. Free stream velocities for droplets on Teflon: 10 μl) 5.6 m/s, 20 μl) 4.8 m/s, 30 μl) 4.5 m/s. Free stream velocities for droplets on PS: 10 μl) 8.5 m/s, 20 μl) 8.2 m/s, 30 μl) 6.6 m/s. Free stream velocities for droplets on PEMA: 10 μl) 8.9 m/s, 20 μl) 8.3 m/s, 30 μl) 8.1 m/s. Free stream velocities for droplets on PMMA: 10 μl) 10.8 m/s, 20 μl) 9.9 m/s, 30 μl) 8.4 m/s

The difference between the normalized u'$_{rms}$ of air flow downstream the small and large droplets on PS and PMMA however, is less that of Teflon and PEMA. Higher level of turbulence downstream of the large droplets is due to the large droplets blocking the free stream flow and not only the boundary layer flow.

More importantly, as the turbulence level close to droplet profile is insignificant, the following conclusion is yet more reinforced:

- For all droplet sizes and surface wettabilities, the instantaneous drag coefficient is similar to their average value.

4.6.3 The effect of drop size on normalized u'_{rms} (using maximum normalzied u'_{rms}values)

Figure 4-39 shows the maximum normalized u'_{rms} values for air flow over sessile droplets for all the cases together. Figure 4-39 clearly indicates that for all surface wettabilities, the larger the droplet, the higher the turbulence level (normalized u'_{rms}). As explained earlier, the reason lies in the state of droplet height vs. boundary layer height. The larger the droplet gets; more blockage is seen by the free stream flow. To block such high velocity flow at once, high levels of turbulence is to be expected downstream the flow. The considerable difference between normalized u'_{rms} values for $10\ \mu l$ and $20\ \mu l$ droplets can be explained with the status of the droplets and the boundary layer (that for $10\ \mu l$ droplets the droplet is exposed only to boundary layer flow while larger droplets block the free stream flow as well). Then the conclusions made earlier is yet reinforced that:

- for a tandem arrangement of droplets, if droplets are larger, those droplets placed downstream are exposed to a more turbulent flow.

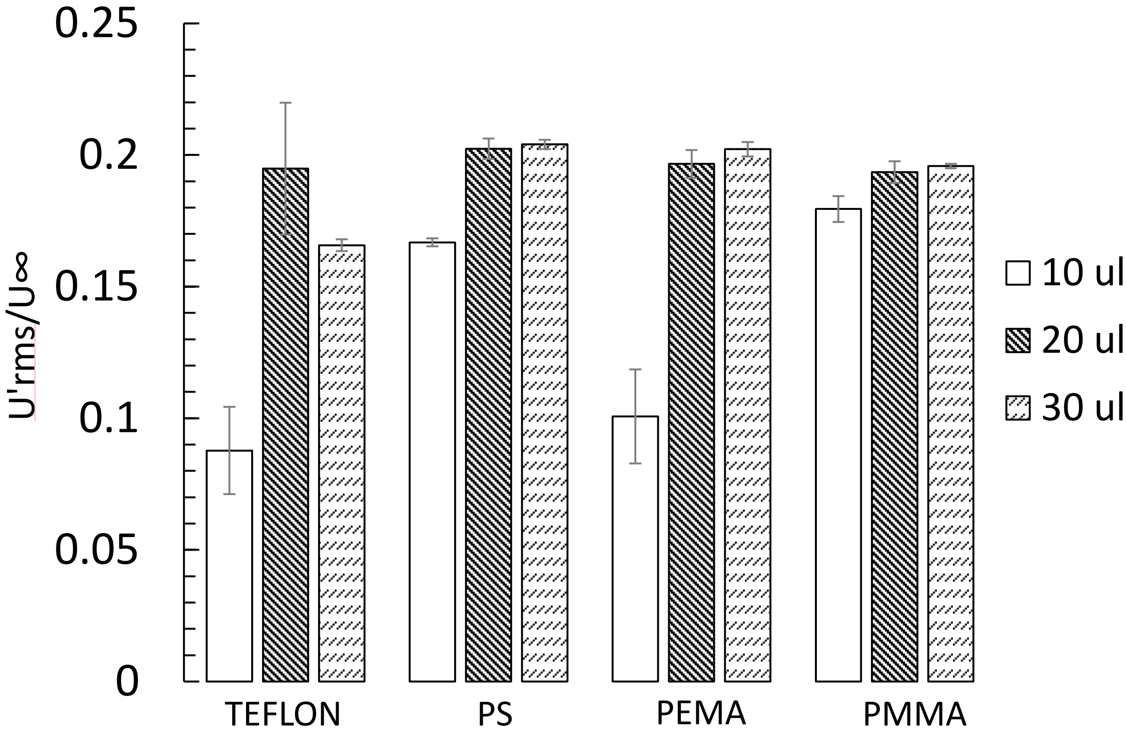

Figure 4-39. Maximum normalized u'_{rms} $\left({u'_{rms}}/{U_\infty}\right)$ values for air flow over sessile dorplets.

Free stream velocities for droplets on Teflon: 10 µl) 5.6 m/s, 20 µl) 4.8 m/s, 30 µl) 4.5 m/s.

Free stream velocities for droplets on PS: 10 µl) 8.5 m/s, 20 µl) 8.2 m/s, 30 µl) 6.6 m/s.

Free stream velocities for droplets on PEMA: 10 µl) 8.9 m/s, 20 µl) 8.3 m/s, 30 µl) 8.1 m/s.

Free stream velocities for droplets on PMMA: 10 µl) 10.8 m/s, 20 µl) 9.9 m/s, 30 µl) 8.4 m/s

4.6.4 The effect of drop size on turbulence intensity (conclusions)

Through the results provided on ${u'_{rms}}/{U_\infty}$ in the flow field, the following conclusions are made:

- Larger droplets induce higher levels of turbulence intensity in the field.
- For a tandem arrangement of droplets, if droplets are larger, those droplets placed downstream are exposed to a more turbulent flow.
- For all droplet sizes and surface wettabilities, the instantaneous drag coefficient is similar to their average value.

4.6.5 effects of wettability and drop size on normalized Reynolds stress

The contours in Figure 4-40 suggest that as droplets get larger, the turbulence intensity increases (higher Reynolds stress values are seen in the flow field).

The contours also indicate that for small droplets, those placed on PS and PMMA, show higher Reynolds Stress in the field. Larger droplets show almost similar contours (with PS, PEMA and PMMA showing a bit higher values than Teflon (about 10%) which was also seen for normalized u'rms data) suggesting that for larger droplets, the wettability does not change the turbulence level (considering the normalized data) significantly. Thus, all conclusions made using ${u'_{rms}}/{U_\infty}$ values hold true using Reynolds Stress. The conclusions are:

- For all droplets (regardless of surface wettability and drop size) the instantaneous drag coefficients are similar to their average values as the turbulence around the droplet profile is insignificant.

- For the air flow over small sessile droplets, turbulence is the highest when the surface is coated with PMMA and PS.

- For the air flow over large sessile droplets, turbulence intensity does not change considerably with surface wettability.

- For all droplets the instantaneous drag coefficients are similar to their average values as the turbulence around the droplet profile is insignificant.

- Larger droplets induce higher levels of turbulence intensity in the field
- For a tandem arrangement of droplets, if droplets are larger, those droplets placed downstream are exposed to a more turbulent flow.

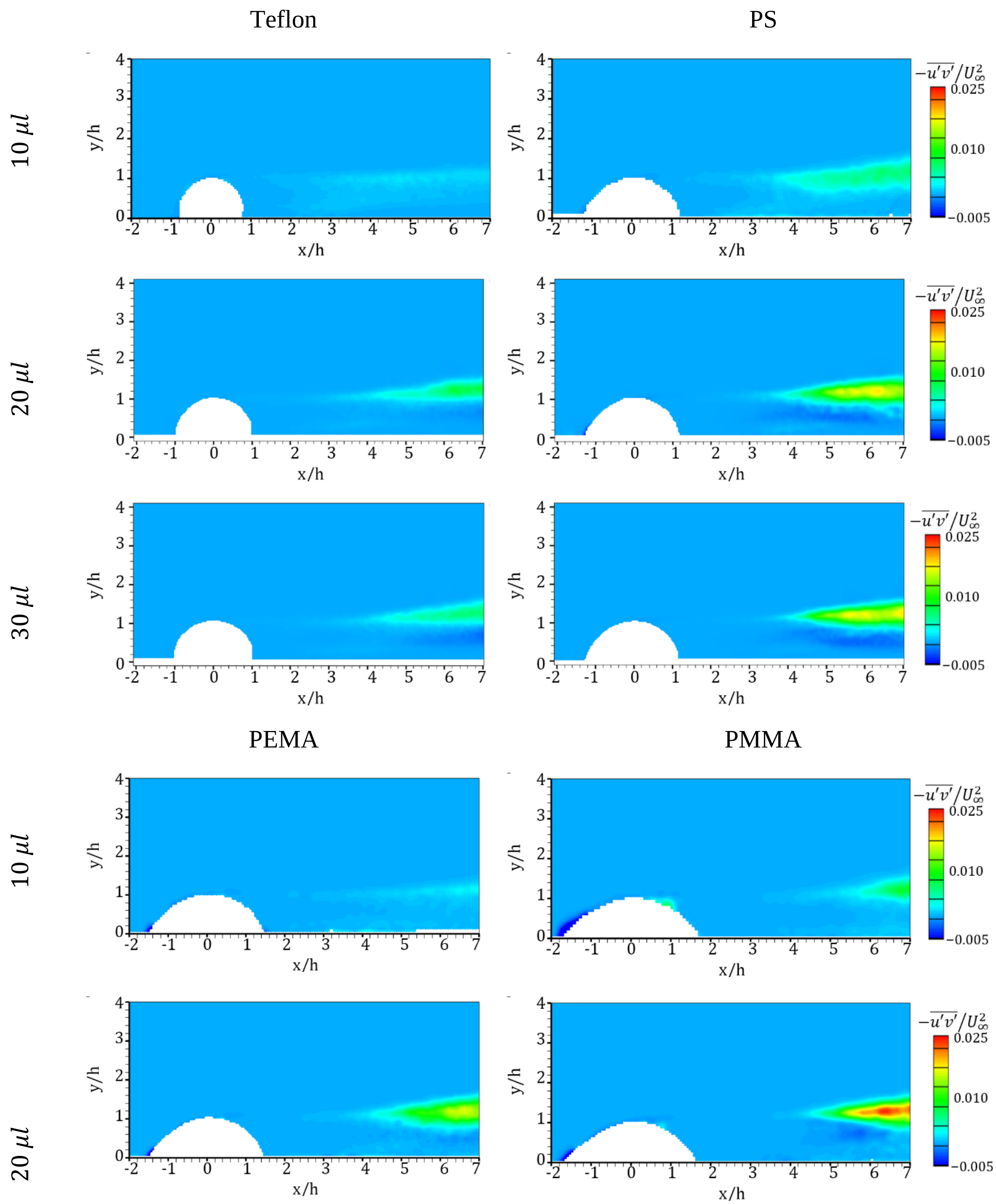

Continues next page…

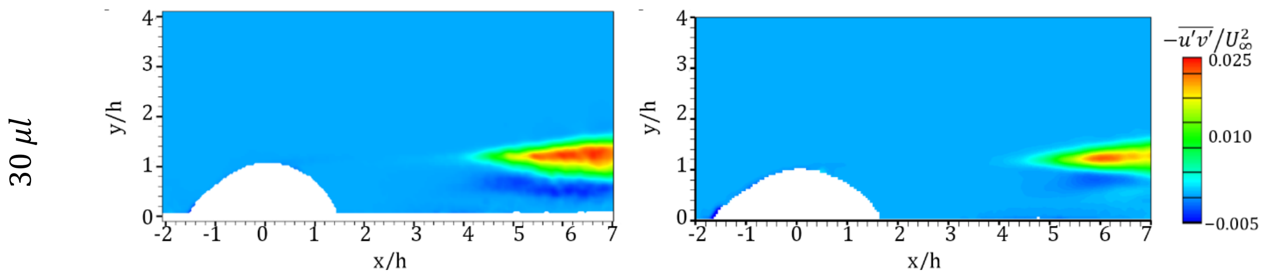

Figure 4-40. Normalized Reynolds stress ($\overline{u'v'}/U_\infty^2$) contours. Free stream velocities for droplets on Teflon: 10 µl) 5.6 m/s, 20 µl) 4.8 m/s, 30 µl) 4.5 m/s. Free stream velocities for droplets on PS: 10 µl) 8.5 m/s, 20 µl) 8.2 m/s, 30 µl) 6.6 m/s. Free stream velocities for droplets on PEMA: 10 µl) 8.9 m/s, 20 µl) 8.3 m/s, 30 µl) 8.1 m/s. Free stream velocities for droplets on PMMA: 10 µl) 10.8 m/s, 20 µl) 9.9 m/s, 30 µl) 8.4 m/s

4.7 The effect of drop oscillations on turbulence intensity

4.7.1 Maximum normalized u'_{rms} for airflow over solid mockups

The maximum normalized u'_{rms} (= u'_{rms}/U_∞) values for air flow over sessile droplets and their solid mockups are presented in Figure 4-41 - Figure *4-44*. The error bars show a "± standard deviation" from the average values calculated out of three separate experiments for each case study. For all surface wettabilities, the maximum u'_{rms} values for airflow over sessile droplets fairly match those of their solid mockups. The similarity is the highest for PS, PEMA and PMMA surfaces such that the values are remarkably close to each other. For Teflon also, the values are close to each other and the trend is held with the solid mockups.

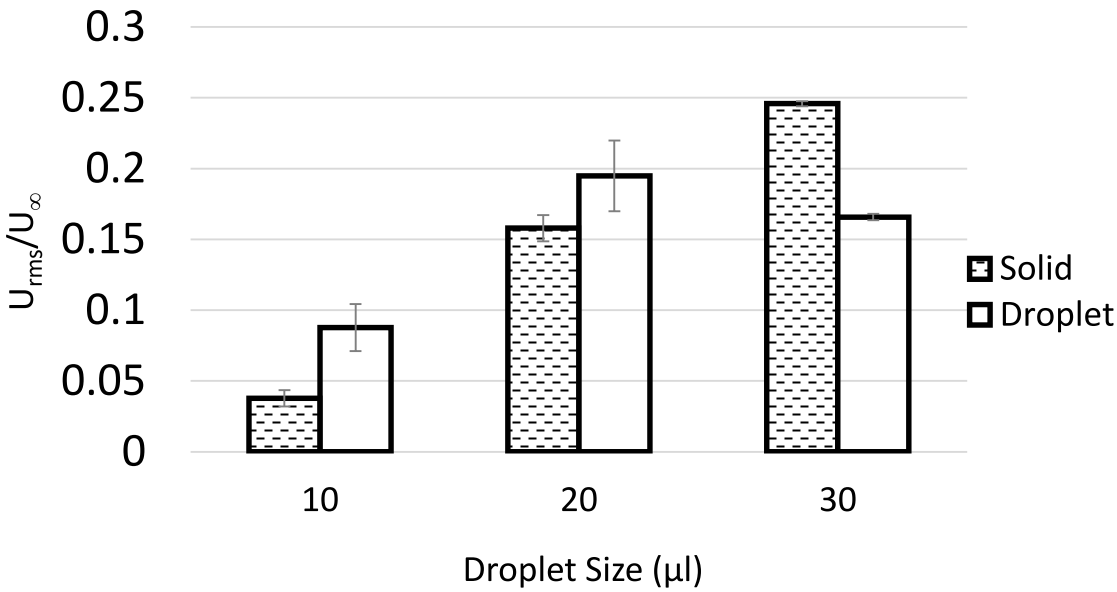

Figure 4-41. The normalized u'_{rms} (u'_{rms}/U_{∞}) values for air airflow over sessile droplets placed on Teflon and their mockups. Free stream velocities for droplets on Teflon: $10\ \mu l)$ $5.6\ m/s$, $20\ \mu l)$ $4.8\ m/s$, $30\ \mu l)$ $4.5\ m/s$

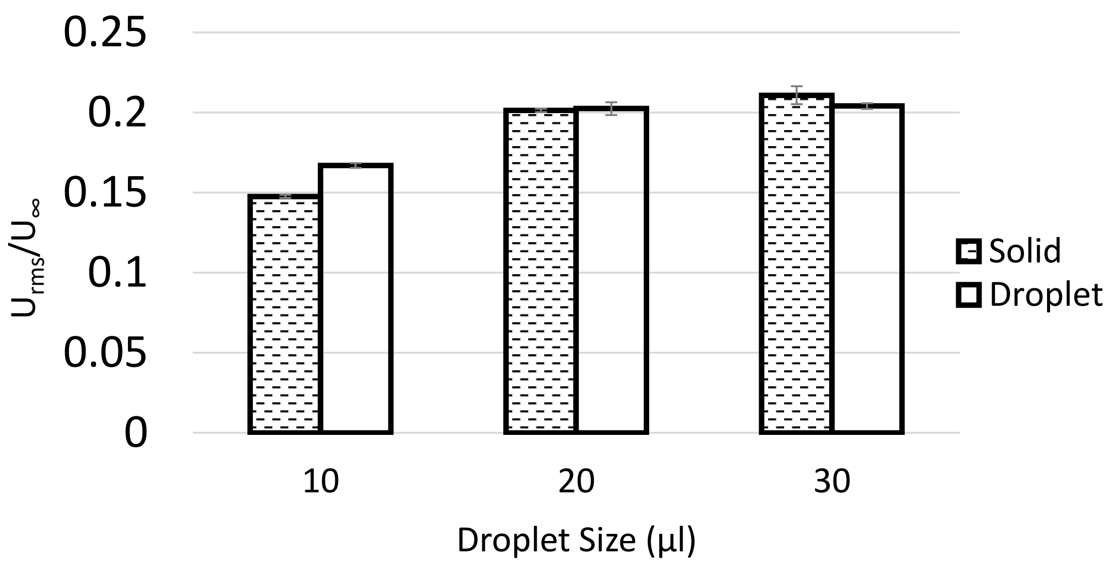

Figure 4-42. The normalized $\mathrm{u}'_{\mathrm{rms}}$ ($\mathrm{u}'_{\mathrm{rms}}/\mathrm{U}_{\infty}$) values for air airflow over sessile droplets placed on PS and their mockups. Free stream velocities for droplets on PS: 10 µl) 8.5 m/s, 20 µl) 8.2 m/s, 30 µl) 6.6 m/s.

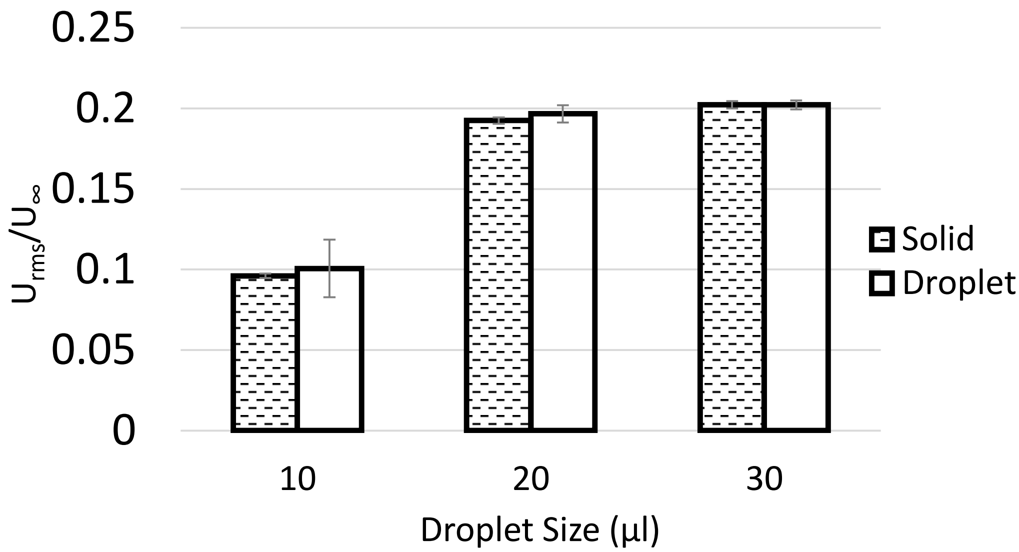

Figure 4-43. The normalized u'_{rms} ($^{u'_{rms}}/_{U_\infty}$) values for air airflow over sessile droplets placed on PEMA and their mockups. Free stream velocities for droplets on PEMA: 10 µl) 8.9 m/s, 20 µl) 8.3 m/s, 30 µl) 8.1 m/s

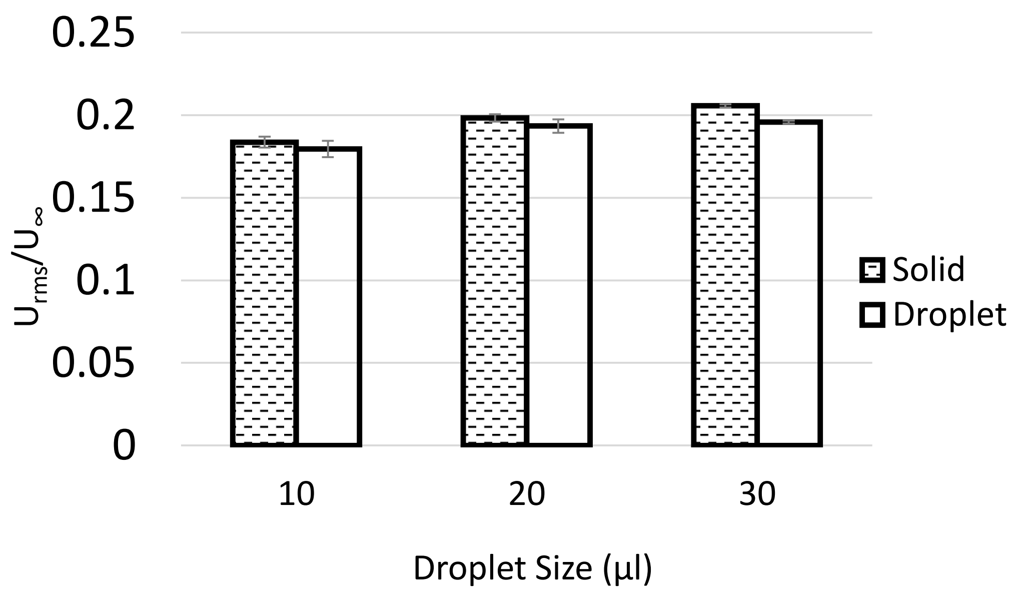

Figure 4-44. The normalized u'_{rms} ($^{u'_{rms}}/_{U_\infty}$) values for air airflow over sessile droplets placed on Teflon and their mockups. Free stream velocities for droplets on PMMA: 10 μl) 10.8 m/s, 20 μl) 9.9 m/s, 30 μl) 8.4 m/s

Noticeable similarity for maximum u'_{rms} values and flow structure for air flow over sessile droplets and their solid mockups is seen. Then, only considering the midplane data, it could be concluded that:

- The turbulence induced downstream of solid mockups of droplets is similar to the turbulence downstream of the droplets themselves. (if the ramp-up is as slow as $\sim 2.8\,\frac{m/s}{min}$).
- The effect of oscillation in flow structure and turbulence statistics is equivalent to the effect of surface roughness for the 3D-printed solid mockups. (if the ramp-up is as slow as $\sim 2.8\,\frac{m/s}{min}$).
- For a slow ramp-up of $\sim 2.8\,\frac{m/s}{min}$, the effect of oscillations in droplets in inducing turbulence in the flow field is as significant as the effect of surface roughness for a not ideally smooth (life the surface of a droplet) body.

5 Conclusions

Having gone through all the data regarding the characteristics of air flow over sessile droplets with different sizes and placed on different surface wettabilities plus their solid mockups, the following conclusions are made (note that all the conclusions are made for the midplane of the droplet):

- Flow Structure (Patten) in mid-plane is similar for air flow over droplets regardless of wettability and size.
- The more hydrophilic the surface, the longer the normalized recirculation length.
- The "actual" recirculation length for sessile droplets on hydrophobic surfaces, are longer than those on hydrophilic surfaces. Meaning that, droplets on hydrophobic surfaces should keep longer distances from each other to be shed independently (to depin at a critical velocity for a single droplet with the same conditions (wettability/size)).
- For hydrophilic surfaces, the normalized recirculation length decreases with size.
- For hydrophobic surfaces, the normalized recirculation length increases with size.
- For hydrophilic surfaces, the distance to which two sessile droplets are shed independently from each other, increases only slightly with drop height.
- For hydrophobic surfaces, the distance to which two sessile droplets are shed independently from each other, proportionally changes with drop height.
- The normalized velocity profiles upstream and on the droplet are identical for different drop sizes.
- Flow separation angle is similar (~97°) for droplets of different sizes on surfaces with different wettabilities.

- The order of c_f is the same for all the cases due to velocity profile and separation angle similarity.
- The order of magnitude of c_p is the same for all drop sizes on different surface wettabilities.
- With c_p and c_f being similar for droplets at the verge of shedding (regardless of surface wettability and drop size): the drag force by which the droplets are depinned changes only with AU_∞^2 (in which A is the frontal area of the droplet and U_∞ is the free stream velocity of the air when the droplet is at the verge of shedding).
- The effect of drop surface oscillations on changing the flow structure is insignificant.
- The effect of drop surface oscillations on defining the recirculation length is as significant as the effect of solid mockups surface roughness on the recirculation length.
- For all droplet sizes and surface wettabilities, the turbulence around the droplet profile is insignificant.
- For all droplet sizes and surface wettabilities, the instantaneous drag coefficient is similar to their average value.
- For all drop sizes and surface wettabilities, the highest turbulence is found further downstream of the droplet (after the recirculation zone).
- For the air flow over small sessile droplets, turbulence downstream of the droplet is the highest when the surface is coated with PMMA and PS.
- For a tandem arrangement of small droplets, those droplets sitting downstream of a droplet on PS and PMMA, experience higher turbulence compared to those on Teflon and PEMA.

- For the air flow over large sessile droplets (20 μl and 30 μl), turbulence downstream of the droplet does not change with surface wettability.
- For a tandem arrangement of large droplets (20 μl and 30 μl), the droplets that are sitting downstream of a droplet experience similar turbulence in the shearing flow, regardless of the surface wettability.
- Larger droplets induce higher levels of turbulence intensity in the field.
- For a tandem arrangement of droplets, if droplets are larger, those droplets placed downstream are exposed to a more turbulent flow.
- The turbulence induced downstream of solid mockups of droplets is similar to the turbulence downstream of the droplets themselves. (if the ramp-up is as slow as $\sim 2.8\,\frac{m/_s}{min}$).
- The effect of oscillation in flow structure and turbulence statistics is equivalent to the effect of surface roughness for the 3D-printed solid mockups. (if the ramp-up is as slow as $\sim 2.8\,\frac{m/_s}{min}$).
- For a slow ramp-up of $\sim 2.8\,\frac{m/_s}{min}$, the effect of oscillations in droplets in inducing turbulence in the flow field is as significant as the effect of surface roughness for a not ideally smooth (life the surface of a droplet) body.

6 Future Work

A lot remains to be done given the findings of this thesis and the studies in literature. A few important studies that are required to be done using PIV measurements are listed below:

- Investigating the characteristics of air flow over a sessile droplet from top view (with the light sheet crossing the droplet horizontal to the substrate at different elevations).
- Obtaining the 3D flow field for air flow over a sessile droplet using plenoptic cameras or several cameras (a 3D Particle Image Velocity measurement setup).
- Studying the effect of droplet spacing in changing the flow structure and pressure around the droplets for a system of sessile droplets.
- Studying the air flow characteristics (streamlines, x-velocity, y-velocity, vorticity, pressure, angle of flow separation, etc.) around sessile droplets in real conditions (or droplets sitting on wind turbine/airfoil profiles).
- Studying the air flow characteristics around sessile droplets behind a frozen droplet, or collated and frozen droplets.
- Studying the dynamics and characteristics of airflow over sessile droplets from the point of flow exposure to runback, using higher accelerations.

These are only a few studies that such a state-of-the-art experimental setup/measurement technique makes possible. Several other studies could be done using this technique to shed light on the physics of sessile droplet shedding which would enable the related applications and industries to make use of detailed results and understanding in the process.

References

1) Dalili, N., Edrisy, A., & Carriveau, R. (2009). A review of surface engineering issues critical to wind turbine performance. Renewable and Sustainable Energy Reviews, 13(2), 428-438.
2) Politovich, M. K. (1989). Aircraft icing caused by large supercooled droplets. Journal of Applied Meteorology, 28(9), 856-868.
3) Tüber, K., Pócza, D., & Hebling, C. (2003). Visualization of water buildup in the cathode of a transparent PEM fuel cell. Journal of Power Sources, 124(2), 403-414.
4) Dietz, C., Rykaczewski, K., Fedorov, A. G., & Joshi, Y. (2010). Visualization of droplet departure on a superhydrophobic surface and implications to heat transfer enhancement during dropwise condensation. Applied Physics Letters, 97(3), 033104
5) Thoreau, V., Malki, B., Berthome, G., Boulange-Petermann, L., & Joud, J. C. (2006). Physico-chemical and dynamic study of oil-drop removal from bare and coated stainless-steel surfaces. Journal of Adhesion Science and Technology, 20(16), 1819-1831.
6) Cebeci, T., & Kafyeke, F. (2003). Aircraft icing. Annual Review of Fluid Mechanics, 35(1), 11-21.
7) Zhang, F. Y., Yang, X. G., & Wang, C. Y. (2006). Liquid water removal from a polymer electrolyte fuel cell. Journal of the Electrochemical Society, 153(2), A225-A232.
8) Madani, S., & Amirfazli, A. (2014). Oil drop shedding from solid substrates by a shearing liquid. Colloids and Surfaces A: Physicochemical and Engineering Aspects, 441, 796-806.
9) Deepu, P., Basu, S., & Kumar, R. (2014). Multimodal shape oscillations of droplets excited by an air stream. Chemical Engineering Science, 114, 85-93.
10) Milne, A. J. B., & Amirfazli, A. (2009). Drop shedding by shear flow for hydrophilic to superhydrophobic surfaces. Langmuir, 25(24), 14155-14164.
11) Antonini, C., Carmona, F. J., Pierce, E., Marengo, M., & Amirfazli, A. (2009). General methodology for evaluating the adhesion force of drops and bubbles on solid surfaces. Langmuir, 25(11), 6143-6154.
12) Brown, R. A., Orr Jr, F. M., & Scriven, L. E. (1980). Static drop on an inclined plate: analysis by the finite element method. Journal of Colloid and Interface Science, 73(1), 76-87.

13) Quéré, D., Azzopardi, M. J., & Delattre, L. (1998). Drops at rest on a tilted plane. Langmuir, 14(8), 2213-2216.
14) Extrand, C. W., & Kumagai, Y. (1995). Liquid drops on an inclined plane: the relation between contact angles, drop shape, and retentive force. Journal of Colloid and Interface Science, 170(2), 515-521.
15) Chow, R. T. P. (1983). On the ability of drops or bubbles to stick to non-horizontal surfaces of solids. Journal of Fluid Mechanics, 137, 1-29.
16) ElSherbini, A. I., & Jacobi, A. M. (2004). Liquid drops on vertical and inclined surfaces: I. An experimental study of drop geometry. Journal of Colloid and Interface Science, 273(2), 556-565.
17) Milne, A. J. B., Defez, B., Cabrerizo-Vílchez, M., & Amirfazli, A. (2014). Understanding (sessile/constrained) bubble and drop oscillations. Advances in Colloid and Interface Science, 203, 22-36.
18) Jang, Y. I., & Lee, S. J. (2008). PIV analysis of near-wake behind a sphere at a subcritical Reynolds number. Experiments in Fluids, 44(6), 905-914.
19) Ozgoren, M., Okbaz, A., Dogan, S., Sahin, B., & Akilli, H. (2013). Investigation of flow characteristics around a sphere placed in a boundary layer over a flat plate. Experimental Thermal and Fluid Science, 44, 62-74.
20) Ozgoren, M., Pinar, E., Sahin, B., & Akilli, H. (2011). Comparison of flow structures in the downstream region of a cylinder and sphere. International Journal of Heat and Fluid Flow, 32(6), 1138-1146.
21) Jung, S., Mareck, K., Shelley, M., & Zhang, J. (2006). Dynamics of a deformable body in a fast flowing soap film. Physical Review Letters, 97(13), 134502.
22) Fujiwara, A., Danmoto, Y., Hishida, K., & Maeda, M. (2004). Bubble deformation and flow structure measured by double shadow images and PIV/LIF. Experiments in Fluids, 36(1), 157-165.
23) Ysasi, A., Kanso, E., & Newton, P. K. (2011). Wake structure of a deformable Joukowski airfoil. Physica D: Nonlinear Phenomena, 240(20), 1574-1582.
24) Michelin, S., Smith, S. G. L., & Glover, B. J. (2008). Vortex shedding model of a flapping flag. Journal of Fluid Mechanics, 617, 1-10.
25) White, F. M. (1999). Fluid mechanics.

26) Seiler, P. M., Gloerfeld, M., Roisman, I. V., & Tropea, C. (2019). Aerodynamically driven motion of a wall-bounded drop on a smooth solid substrate. Physical Review Fluids, 4(2), 024001.
27) Fan, J., Wilson, M. C. T., & Kapur, N. (2011). Displacement of liquid droplets on a surface by a shearing air flow. Journal of Colloid and Interface Science, 356(1), 286-292.
28) O'neill, M. E. (1968). A sphere in contact with a plane wall in a slow linear shear flow. Chemical Engineering Science, 23(11), 1293-1298.
29) Razzaghi, A., & Amirfazli, A. (2019). Shedding of a pair of sessile droplets. International Journal of Multiphase Flow, 110, 59-68.
30) Dimitrakopoulos, P., & Higdon, J. J. L. (1997). Displacement of fluid droplets from solid surfaces in low-Reynolds-number shear flows. Journal of Fluid Mechanics, 336, 351-378.
31) Zhu, X., Sui, P. C., & Djilali, N. (2008). Numerical simulation of emergence of a water droplet from a pore into a microchannel gas stream. Microfluidics and Nanofluidics, 4(6), 543-555.
32) Jarauta, A., Ryzhakov, P., Secanell, M., Waghmare, P. R., & Pons-Prats, J. (2016). Numerical study of droplet dynamics in a polymer electrolyte fuel cell gas channel using an embedded Eulerian-Lagrangian approach. Journal of Power Sources, 323, 201-212.
33) Jarauta, A., Secanell, M., Pons-Prats, J., Ryzhakov, P., Idelsohn, S. R., & Oñate, E. (2015). A semi-analytical model for droplet dynamics on the GDL surface of a PEFC electrode. International Journal of Hydrogen Energy, 40(15), 5375-5383.
34) Jarauta, A., & Ryzhakov, P. (2018). Challenges in Computational Modeling of Two-Phase Transport in Polymer Electrolyte Fuel Cells Flow Channels: A Review. Archives of Computational Methods in Engineering, 25(4), 1027-1057.
35) Mandal, D. K., Criscione, A., Tropea, C., & Amirfazli, A. (2015). Shedding of water drops from a surface under icing conditions. Langmuir, 31(34), 9340-9347.
36) Razzaghi, A., Banitabaei, S. A., & Amirfazli, A. (2018). Shedding of multiple sessile droplets by an airflow. Physics of Fluids, 30(8), 087104.
37) Kim, D., & Choi, H. (2003). Laminar flow past a hemisphere. Physics of Fluids, 15(8), 2457-2460.

38) Johnson, K. C., Thurow, B. S., Kim, T., Blois, G., & Christensen, K. T. (2017). Volumetric velocity measurements in the wake of a hemispherical roughness element. AIAA Journal, 2158-2173.

39) Panigrahi, P. K., Schroeder, A., & Kompenhans, J. (2006). PIV investigation of flow behind surface mounted permeable ribs. Experiments in Fluids, 40(2), 277-300.

40) Wang, L., Hejcik, J., & Sunden, B. (2007). PIV measurement of separated flow in a square channel with streamwise periodic ribs on one wall. Journal of Fluids Engineering, 129(7), 834-841.

41) Panigrahi, P. K. (2009). PIV investigation of flow behind surface mounted detached square cylinder. Journal of Fluids Engineering, 131(1), 011202.

42) Pinar, E., Sahin, B., Ozgoren, M., & Akilli, H. (2013). Experimental study of flow structures around side-by-side spheres. Industrial & Engineering Chemistry Research, 52(40), 14492-14503.

43) Ozgoren, M. (2013). Flow structures around an equilateral triangle arrangement of three spheres. International Journal of Multiphase Flow, 53, 54-64.

44) Mehta, R. D., & Bradshaw, P. (1979). Design rules for small low speed wind tunnels. The Aeronautical Journal, 83(827), 443-453.

45) Batchelor, G. K. (1953). The Theory of Homogeneous Turbulence. Cambridge University press, United Kingdom.

46) Cattafesta, L., Bahr, C., & Mathew, J. (2010). Fundamentals of wind-tunnel design. Encyclopedia of Aerospace Engineering.

47) Bell, J. H., & Mehta, R. D. (1988). Contraction design for small low-speed wind tunnels. NASA Technical Reports Server.

48) Brassard, D., & Ferchichi, M. (2005). Transformation of a polynomial for a contraction wall profile. J. Fluids Eng., 127(1), 183-185.

49) Hanson, R. E., Buckley, H. P., & Lavoie, P. (2012). Aerodynamic optimization of the flat-plate leading edge for experimental studies of laminar and transitional boundary layers. Experiments in Fluids, *53*(4), 863-871.

50) Raffel, M., Willert, C. E., Scarano, F., Kähler, C. J., Wereley, S. T., & Kompenhans, J. (2018). Particle image velocimetry: a practical guide. Springer.

51) Cao, X., Liu, J., Jiang, N., & Chen, Q. (2014). Particle image velocimetry measurement of indoor airflow field: A review of the technologies and applications. Energy and Buildings, 69, 367-380.

52) www.litronlasers.com/. Accessed online on January 2020.

53) Zhang, C., Vasilevskis, S., & Kozlowski, B. (2018). Particle Image Velocimetry: User Guide.

54) https://www.lavision.de/. Accessed online on January 2020.

55) Milne, A. J. (2013). Blown Away: The Shedding and Oscillation of Sessile Drops by Cross Flowing Air. University of Alberta, Canada.

56) Choi, D., & Park, H. (2018). Flow around in-line sphere array at moderate Reynolds number. Physics of Fluids, 30(9), 097104.)

Appendices

A. Calculations

A.1 Test Section calculations

First off, one should know how the boundary layer growth is inside the channel to find out the thickness of the free stream flow at each location. The free stream core is simply the core of the channel in which the boundary layer hasn't reached yet. In order to do so, Reynolds number should be calculated firstly as the boundary layer thickness completely relies on Reynolds number (no matter what type of the flow e.g., External vs. Internal or Laminar vs. Turbulent, is being considered). As the flow passes the "Flow Conditioning and Settling Chamber" a fresh uniform flow is started with very small turbulence intensity which could be ignored. Thus, the first assumption being made here is that the boundary layer starts as the air enters the contraction chamber. Secondly, to derive the boundary layer thickness at each local point, the boundary layer development to the point of internal fully developed flow, has been simplified to be linear. Thirdly, as the contraction chamber profile is complicated, the exact development of the flow inside, would be significantly complicated to calculate analytically. Thus, the average hydraulic diameter of the chamber has been calculated using the dimensions of the entrance and the exit. Then, the calculations would be as follows:

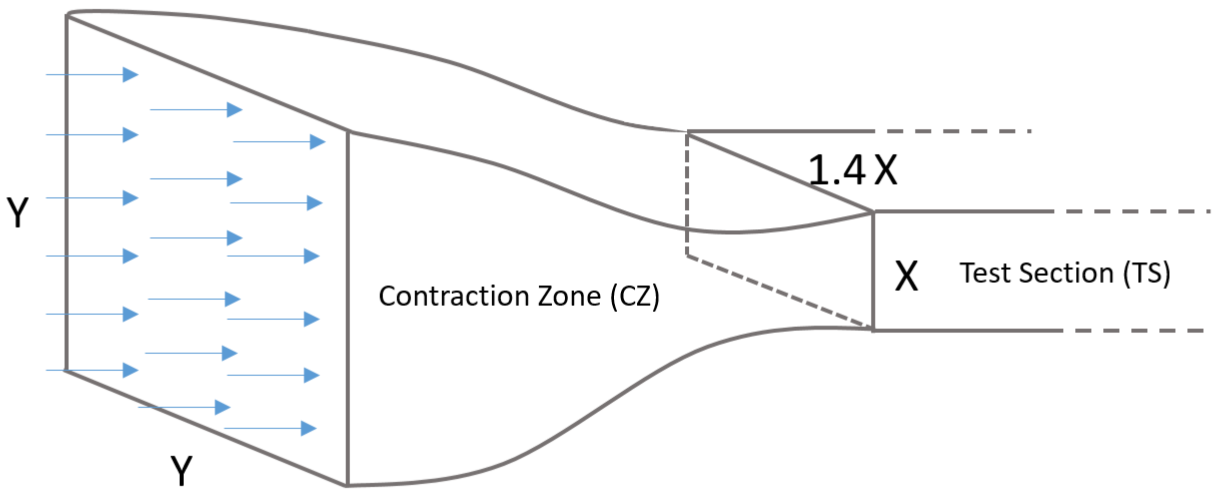

Figure A-1. The schematic of contraction zone and the test section before defining the dimensions.

Regarding the literature, the contraction ratio is one of the most important parameters which has a direct effect on the flow quality, and it is that the larger the contraction ratio, the more uniform the air flow inside the test section would get. Nevertheless, as the contraction ratio becomes larger, the other elements of the wind tunnel get larger as well, thus, leading to more space consumption and higher costs. However, again, relying on various studies, it could be said that the contraction ratio of 10 would give a flow of considerably high quality of the flow (uniform air flow with the least possible turbulence) for most of the applications [24-26]. Then:

$$N = \frac{Y^2}{1.4X^2} = 10 \tag{A-1}$$

Calculating the hydraulic diameter for the entrances of the Contraction Zone and the Test Section, we would have:

$$D_{H_{CZ}} = \frac{2ab}{a+b} = \frac{2*(3.75X)^2}{7.5X} = 3.75X \tag{A-2}$$

$$D_{H_{TS}} = \frac{2ab}{a+b} = \frac{2*1.4X*X}{2.4X} = 1.17X \tag{A-3}$$

Then by calculating the average of the hydraulic diameter for the entrance and the exit of the contraction zone, $D_{H_{a_{CZ}}}$ would be:

$$D_{H_{a_{CZ}}} = \frac{3.75X + 1.17X}{2} = 2.46X \quad \text{(A-4)}$$

Then, considering the literature on the critical air velocity, taking the velocity of 2 $^{m}/_{s}$ as the lowest possible velocity at the worst case, it needs to be identified whether the flow falls under the laminar regime or if it is turbulent. Considering the velocity inside the test section as 2 $^{m}/_{s}$, the volumetric flow which would be constant for this incompressible air flow is:

$$Q = 2\ ^{m}/_{s} * 1.4X^2 m^2 = 2.8X^2\ ^{m^3}/_{s} \quad \text{(A-5)}$$

Then the velocity inside the contraction zone with an averaged diameter would be calculated as:

$$V_{a_{CZ}} = \frac{2.8X^2}{\pi^{(2.46X)^2}/_{4}} = 0.589\ ^{m}/_{s} \quad \text{(A-6)}$$

Thus, the Re for these two ducts would be:

$$Re_{TS} = \frac{1.225 * 2 * 1.17X}{1.81 * 10^{-5}} = 158370X \quad \text{(A-7)}$$

$$Re_{CZ} = \frac{1.225 * 0.589 * 2.46X}{1.81 * 10^{-5}} = 98063X \quad \text{(A-8)}$$

As the Reynolds number for the Contraction Zone is smaller than that of the Test Section it would be reasonable to identify whether the flow inside the contraction zone is turbulent or laminar. If it is turbulent then indeed a turbulent flow is present inside the test section as well as its Reynolds number is larger than that of the contraction zone. In order to calculate the transition between laminar and turbulent flow Re_{CZ} is put equal to 2300 which gives an X of 2.3 cm. It is of no doubt that the channel height is larger than 2.3 cm, then, it is obvious that the whole analysis is done for a turbulent flow inside both of the ducts. Then as Re_{TS} and Re_{CZ} are both less than $10^7$when the velocity is 2 $^m/_s$ for this case of study, the entrance length for both the contraction zone and the test section would follow the formulation for turbulent flows of $Re < 10^7$:

$$L_{e_{CZ}} = (1.6)(Re_d)^{0.25} * d \approx (1.6)(98063X)^{0.25} * 2.46X \approx 68.65X^{5/4} \quad \text{(A-9)}$$

$$L_{e_{TS}} = (1.6)(Re_d)^{0.25} * d = (1.6)(158370X)^{0.25} * 1.17X = 37.344X^{5/4} \quad \text{(A-10)}$$

To get a rough estimation on how much the length of the contraction would be, we rely on literature in which a transition with an angle around 12° is recommended. Then:

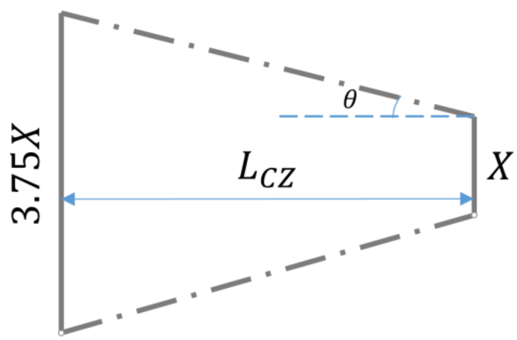

$$\frac{\frac{3.75X}{2}-\frac{X}{2}}{L_{CZ}} = tan(12°) \rightarrow L_{CZ} = 6.47X \quad \text{(A-11)}$$

Then considering the –imaginary (because it exceeds the actual length of the chamber)- entrance length of the contraction zone and its average hydraulic diameter, assuming that the boundary layer grows linearly, the angle for the boundary layer development is achieved:

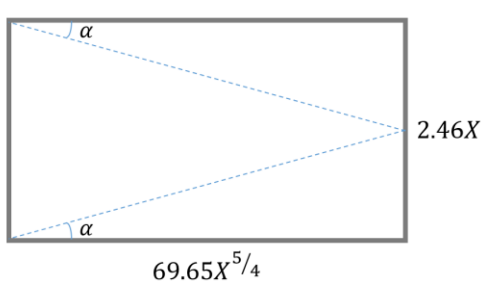

$$tan\alpha = \frac{2.46X/_2}{69.65X^{5/4}} = \frac{2.46}{139.3X^{0.25}} \quad \text{(A-12)}$$

Given the contraction chamber length and the –simplified- angle for boundary layer development, the boundary layer thickness at the end of the chamber (δ_{CZ}) is calculated which will enter the test section:

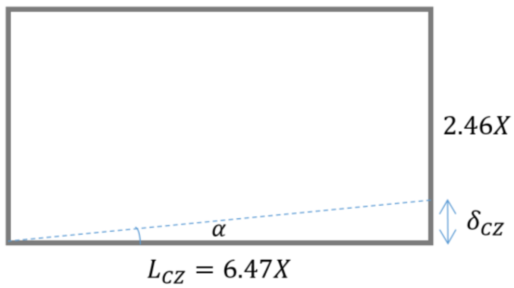

$$\frac{\delta_{CZ}}{6.47X} = tan\alpha = \frac{2.46}{139.3X^{0.25}} \rightarrow \delta_{CZ} = \frac{15.92}{139.3}X^{0.75} \quad \text{(A-13)}$$

Then the same process for the section needs to be done as to realize how fast the boundary layer insider the test section is developed:

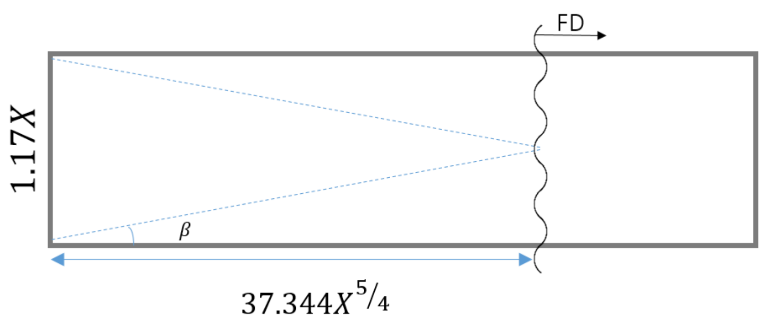

$$tan\beta = \frac{1.17X/_{2}}{37.344X^{5/4}} = \frac{1.17}{74.688X^{0.25}} \quad \text{(A-14)}$$

Then with the Boundary Layer Development rate given inside the test section and the present boundary layer thickness at the entrance, due to the presence of contraction chamber, the total one-sided thickness of the boundary layer at length l past the test section is given by:

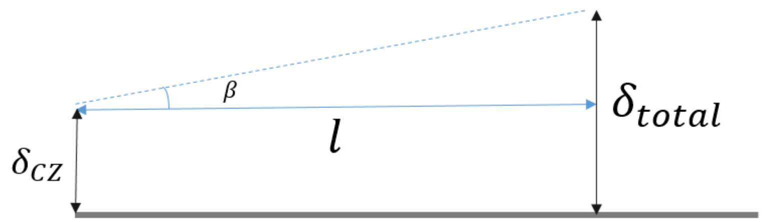

$$\delta_{total} = \frac{1.17L}{74.688X^{0.25}} + \frac{15.92}{139.3}X^{0.75} \tag{A-15}$$

$$Core\ Uniform\ flow\ Diameter: X - 2\delta_{total} \tag{A-16}$$

Which leads to A-16 giving the free stream length in the test section core at the end of the area of interest for the specified study at worst possible case scenario. Considering the Field of View for this study which is 21.09 mm in height and a safety factor of ~ 1.5 for the simplifications and assumptions made in the analysis, a test section with the dimensions of $8 * 11\ cm^2$ sounds as a quite reasonable choice as it would provide uniform flow in the area of interest even for the worst imaginary case for the study at hand, and is not considerably large as to require an unreasonable driving system for the maximum desired velocity ($20\ {}^{m}/_{s}$) to be reached. As for the length of the test section, it is to be considered that while it is desired to be long enough for the study to be done appropriately, it shouldn't be quite large as it would lead to thick boundary layer increasing the possibility of flow separation downstream. As a general rule derived by empirical results it has been recommended for the length of the test section not to be much larger than $3 * hydraulic\ diameter\ of\ the\ cross\ section$. It has been chosen for the test section of this study to be 30 cm long so that the designed deck which is 20 cm long to be put in the middle and for the flow to stabilize after entering the test section.

Table A-1. The free stream length in the test section core

$X\ [cm]$	Boundary layer height at $l = 25\ [cm]$	Free stream length in the middle $[cm]$
5	2.036619	0.926762
6	2.176789	1.646422
7	2.316683	2.366634
8	2.455514	3.088972
9	2.59292	3.814161
10	2.728745	4.542509
11	2.862941	5.274117
12	2.995513	6.008974
13	3.126496	6.747008
14	3.255941	7.488119
15	3.383904	8.232193
16	3.510445	8.979109
17	3.635625	9.72875
18	3.759501	10.481
19	3.882129	11.23574
20	4.003562	11.99288

A.2 Light Sheet Calculations

Given that there are two available cylindrical lenses with $f = -20\ mm$ and $f = -10\ mm$, the aperture angle (APANGLE)and the distance for which the exit of the divergence lens and the plate should be kept on (D), is calculated:

$f := 10\ \mathrm{mm}$ $\qquad\qquad$ $d := 3\ \mathrm{mm}$

APANGLE is the aperture angle when using the divergence lens with specified focal length and the laser beam for which the diameter is 3 mm.

$$APANGLE := 180 \cdot 2 \cdot \frac{\mathrm{atan}\left(\frac{d}{2 \cdot f}\right)}{\pi} = 17.0615$$

D is the distance between the divergence lens and the plate on which the droplet is sitting and it is calculated using basic geometrical conditions.

$FOV := 25\ \mathrm{mm}$

$$D := 2 \cdot \frac{(FOV - d)}{2} \cdot \frac{f}{d} = 0.0733\ \mathrm{m}$$

$f := 20\ \mathrm{mm}$ $\qquad\qquad$ $d := 3\ \mathrm{mm}$

APANGLE is the aperture angle when using the divergence lens with specified focal length and the laser beam for which the diameter is 3 mm.

$$APANGLE := 180 \cdot 2 \cdot \frac{\mathrm{atan}\left(\frac{d}{2 \cdot f}\right)}{\pi} = 8.5783$$

D is the distance between the divergence lens and the plate on which the droplet is sitting and it is calculated using basic geometrical conditions.

$FOV := 25\ \mathrm{mm}$

$$D := 2 \cdot \frac{(FOV - d)}{2} \cdot \frac{f}{d} = 0.1467\ \mathrm{m}$$

A.3 Camera Lens Calculations

The relevant calculations regarding selectoin of a lens for the experiment is given below:

CCDSIZE is the width of the camera's sensor

ODISTANCE is the distance between the Laser light sheet shed in the test section and the front side of the lens

$CCDSIZE := 16.6\ \mathrm{mm}$ $\qquad$ $ODISTANCE := 470\ \mathrm{mm}$

FOVSIZE is the width of the Field of View.

IMAGEHEIGHT is the same as the height in FOV.

$FOVSIZE := 25\ \mathrm{mm}$ $\qquad$ $IMAGEHEIGHT := 21.09\ \mathrm{mm}$

MAG calculates the magnification required to take the proper picture.

$$MAG := \frac{CCDSIZE}{FOVSIZE} = 0.664$$

FOCALLENGTH gives the focal length of the lens required in meters.

$$FOCALLENGTH := \frac{ODISTANCE}{1 + \frac{1}{MAG}} = 0.1875\ \mathrm{m}$$

The ANGULARFOV parameter gives the angular FOV in degrees:

$$ANGULARFOV := 2 \cdot \mathrm{atan}\left(\frac{0.5 \cdot IMAGEHEIGHT}{FOCALLENGTH}\right) \cdot \frac{180}{\pi} = 6.4362$$

B. Datasheet

B.1 Axial Fan

The specifications of the 2214 F/2 TDHH0 axial fan from Ebmpapst used in the wind tunnel is given in Figure B-1.

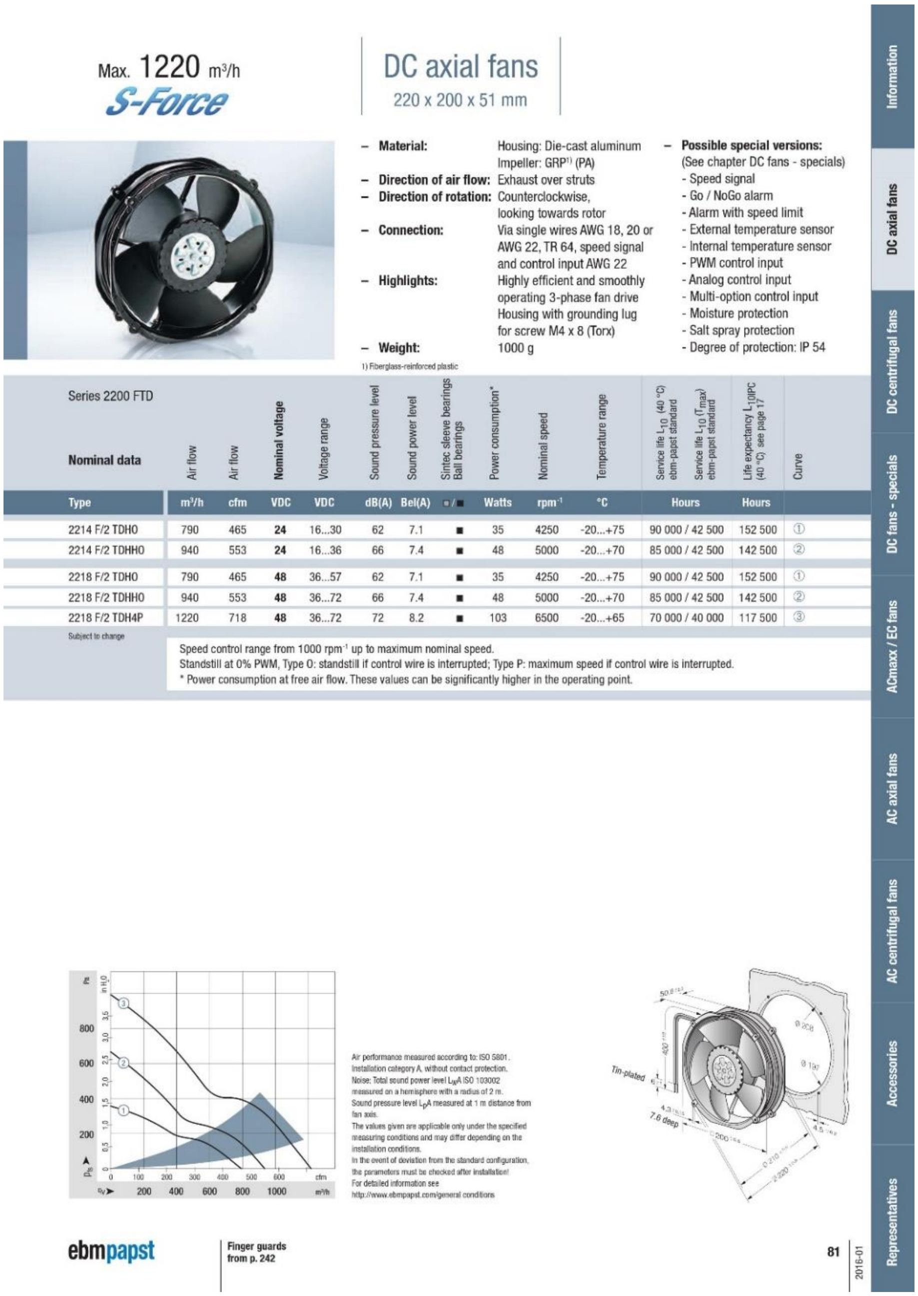

Max. 1220 m³/h
S-Force

DC axial fans
220 x 200 x 51 mm

- **Material:** Housing: Die-cast aluminum; Impeller: GRP[1)] (PA)
- **Direction of air flow:** Exhaust over struts
- **Direction of rotation:** Counterclockwise, looking towards rotor
- **Connection:** Via single wires AWG 18, 20 or AWG 22, TR 64, speed signal and control input AWG 22
- **Highlights:** Highly efficient and smoothly operating 3-phase fan drive; Housing with grounding lug for screw M4 x 8 (Torx)
- **Weight:** 1000 g

1) Fiberglass-reinforced plastic

- **Possible special versions:**
  (See chapter DC fans - specials)
  - Speed signal
  - Go / NoGo alarm
  - Alarm with speed limit
  - External temperature sensor
  - Internal temperature sensor
  - PWM control input
  - Analog control input
  - Multi-option control input
  - Moisture protection
  - Salt spray protection
  - Degree of protection: IP 54

Series 2200 FTD

Nominal data	Air flow	Air flow	Nominal voltage	Voltage range	Sound pressure level	Sound power level	Sintec sleeve bearings / Ball bearings	Power consumption*	Nominal speed	Temperature range	Service life L_{10} (40 °C) / Service life L_{10} (T_{max}) ebm-papst standard	Life expectancy L_{10IPC} (40 °C) see page 17	Curve
Type	m³/h	cfm	VDC	VDC	dB(A)	Bel(A)	□/■	Watts	rpm⁻¹	°C	Hours	Hours	
2214 F/2 TDH0	790	465	**24**	16...30	62	7.1	■	35	4250	-20...+75	90 000 / 42 500	152 500	①
2214 F/2 TDHH0	940	553	**24**	16...36	66	7.4	■	48	5000	-20...+70	85 000 / 42 500	142 500	②
2218 F/2 TDH0	790	465	**48**	36...57	62	7.1	■	35	4250	-20...+75	90 000 / 42 500	152 500	①
2218 F/2 TDHH0	940	553	**48**	36...72	66	7.4	■	48	5000	-20...+70	85 000 / 42 500	142 500	②
2218 F/2 TDH4P	1220	718	**48**	36...72	72	8.2	■	103	6500	-20...+65	70 000 / 40 000	117 500	③

Subject to change

Speed control range from 1000 rpm⁻¹ up to maximum nominal speed.
Standstill at 0% PWM, Type 0: standstill if control wire is interrupted; Type P: maximum speed if control wire is interrupted.
* Power consumption at free air flow. These values can be significantly higher in the operating point.

Air performance measured according to: ISO 5801.
Installation category A, without contact protection.
Noise: Total sound power level $L_{W}A$ ISO 103002 measured on a hemisphere with a radius of 2 m.
Sound pressure level $L_{p}A$ measured at 1 m distance from fan axis.
The values given are applicable only under the specified measuring conditions and may differ depending on the installation conditions.
In the event of deviation from the standard configuration, the parameters must be checked after installation!
For detailed information see
http://www.ebmpapst.com/general conditions

ebmpapst

Finger guards from p. 242

81

2016-01

Figure B-1. The specifications of the axial fan used in the wind tunnel (2214 F/2 TDHH0)

B.2 Stratasys CONNEX3 OBJET260 3D printer

stratasys

Objet260 Connex3

Multi-color, multi-material or versatility? Choose all three for your office.

Unleash your creativity with the most advanced office 3D printer: The Objet260 Connex3™. The Connex3 empowers you to 3D print brilliantly colored prototypes to fit your application needs. The Objet260 Connex3 boasts the widest range of material properties for its class, from rigid to flexible, transparent to opaque, neutral to vibrant, standard to biocompatible and durable to high temperature. With Connex3, incorporate dozens of colors into one prototype, from vivid opaque to stained glass-like translucent, with hundreds of blended hues in between. GrabCAD Print™ software makes it simple to build high-quality, accurate 3D models.

3D Printer Specifications	
Model Materials	Rigid Opaque: VeroPureWhite™, VeroWhitePlus™, VeroBlackPlus™, VeroGray™, VeroBlue™, VeroCyan™, VeroMagenta™, VeroYellow™, VeroMagentaV™, VeroYellowV™
	Rubber-like: Agilus30™, TangoPlus™, TangoBlackPlus™, TangoBlack™, TangoGray™
	Transparent: VeroClear™ and RGD720
	Simulated Polypropylene: Rigur™ and Durus™
	High Temperature
	Bio-compatible
Digital Materials	Vibrant blended colors in Rigid Opaque
	Translucent colored tints
	Rubber-like materials in a variety of Shore A values
	Digital ABS Plus™ for durability, including blends with rubber
	Simulated polypropylene materials with improved heat resistance
Material Options	Over 1,000
Maximum Materials per Part	82
Support Material	SUP705 (WaterJet removable), SUP706 (soluble)
Maximum Build Size (XYZ)	255 x 252 x 200 mm (10.0 x 9.9 x 7.9 in.)
System Size	87 x 120 x 73.5 cm (34.2 x 47.2 x 29 in.)
	Material Cabinet: 33 x 117 x 64 cm (13 x 46.1 x 25.2 in.)
System Weight	264 kg (581 lbs.)
	Material Cabinet: 76 kg (168 lbs.)
Resolution	**X-axis:** 600 dpi; **Y-axis:** 600 dpi; **Z-axis:** 1600 dpi
Accuracy[1]	Typical deviation from STL dimensions, for models printed with rigid materials, based on size: under 100 mm – ±100μ; above100 mm – ±200μ.
Minimum Layer Thickness	Horizontal build layers as fine as 16 microns (.0006 in.)
Build Modes	**Digital Material:** 30-micron (.001 in.) resolution
	High Quality: 16-micron (.0006 in.) resolution
	High Speed: 30-micron (.001 in.) resolution

[1] These results are valid for about 95% of printed models, measured when ambient temperature is 23 °C and relative humidity is 50%.

Spec Sheet

Figure B-2. The specifications of “Stratasys CONNEX3 OBJET260” 3D printer

B.3 MakerBot Z18 3D printer

Print Technology:

Fused Deposition Modeling

Build Volume:

30.0 L x 30.5 W x 45.7 H CM

[11.8 L x 12.0 W x 18.0 H IN]

2,549 cubic inches

Layer Resolution:

100 microns

Material Diameter:

1.75 mm [0.069 IN]

Material Compatibility:

MakerBot PLA Material - Large Spool

MakerBot Tough Material - Large Spool

Additional materials such as bronzefill, copperfill, and woodfill

Extruder Compatibility:

Smart Extruder+

Tough Smart Extruder+

Experimental Extruder

Nozzle Diameter:

0.4 MM [0.015 IN]

B.4 Camera

The specifications of the imager sCMOS is given in Table B-1.

Table B-1. The specifications of the imager sCMOS

General System Specifications	**Value**
Double shutter	two images with 120 ns interframing time
Exposure time	15 µs - 100 ms
Digital output	16 bit
Lens mount	F-mount (optional C-mount)
Number of pixels	2560 x 2160 pixels
Pixel size	6.5 µm x 6.5 µm
Interface	PCI-ExpressCard (4 x slot)
Active area	16.6 mm x 14.0 mm
Frame rate	50 fps

B.5 Lens

The specifications for 180mm F/3.5 Di SP MACRO 1:1 Lens from TAMRON is given in Table B-2.

Table B-2. The specifications of 180mm F/3.5 Di SP MACRO 1:1

Model	*B01*
Lens Construction (Groups/Elements)	11/14
Angle of View	14°
Diaphragm Blade Number	7
Minimum Focus Distance	0.47m (18.5″)
Macro Magnification Ratio	1:1
Filter Diameter	ø72
Weight	920g (32.5oz.)
Diameter x Length	ø84.8mmx165.7mm (3.3in x 6.5in)
Mount	Canon, Nikon, Sony A mount